

**Master's Thesis**

**Untersuchung von Eigenschaften des Top-Quarks  
unter Benutzung eines Profile-Likelihood-Fits bei  
ATLAS**

**Studies of Top Quark Properties Using a Profile  
Likelihood Fit at ATLAS**

prepared by

**Philipp Stolte**

from Göttingen

at the II. Institute of Physics

**Thesis number:** II.Physik-UniGö-MSc-2012/06  
**Thesis period:** March 30, 2012 until September 27, 2012  
**Supervisors:** Dr. Kevin Kröniger  
Dipl. Phys. Andrea Knue  
**First Referee:** Prof. Dr. Arnulf Quadt  
**Second Referee:** Prof. Dr. Ariane Frey



## Abstract

Top quarks play an essential role in the field of elementary particle physics - especially due to their remarkable properties comprising a large mass, which is approximately comparable to the mass of a tungsten atom, and an extremely short lifetime: Examining this quark in more detail and measuring its properties serves, for instance, to test the established Standard Model of particle physics and the results may also hint at unknown physics beyond this model.

Profile likelihood fits constitute a comparatively new fitting technique applied to determine such top quark properties. These fits are based on the idea of constraining the most relevant systematic uncertainties, which considerably affect the underlying measurement, via additional fit parameters to significantly reduce the total systematic uncertainty of the measured quantities. Each of these fit parameters, commonly denoted as nuisance parameters, accounts for exactly one certain systematic effect. In this master's thesis, two different measurements using profile likelihood fits are presented in detail. The first part of the thesis is concerned with determining the  $Wt$  production cross-section of single top quarks whereas the second analysis constitutes a measurement of the  $W$  boson polarisation in top quark pair decays. Both analyses are based on the muon+jets decay channel. Emphasis is placed on investigating the general performance and possible strengths of profile likelihood fits by testing various setups, implementations and fitting algorithms but also, primarily in the context of the second measurement, on validating the stability and the modelling of the fit in very much detail.

In order to perform all the different fits, a programme was designed in the framework of this thesis. The developed flexible tool can be adapted to other promising profile likelihood analyses in the near future.

## Zusammenfassung

Top-Quarks spielen eine wichtige Rolle in der Elementarteilchenphysik - insbesondere aufgrund ihrer bemerkenswerten Eigenschaften, die eine sehr große Masse, die ungefähr mit derjenigen eines Wolframatoms vergleichbar ist, oder eine extrem kurze Lebensdauer umfassen: Genauere Untersuchungen dieses Quarks sowie Messungen seiner Eigenschaften ermöglichen zum Beispiel, das wohlbekanntes Standardmodell der Teilchenphysik zu testen, und können außerdem Hinweise auf unbekanntes Physik jenseits dieses Modells liefern.

Profile-Likelihood-Fits stellen eine vergleichsweise neue Fitmethode dar, die bei der Bestimmung von Top-Quark-Eigenschaften sehr dienlich sein kann. Solche Fits basieren auf der Idee, die wichtigsten systematischen Unsicherheiten, die eine zugrundeliegende Messung nennenswert beeinflussen können, mittels weiterer, zusätzlicher Fitparameter einzuschränken, sodass die gesamte systematische Unsicherheit auf die gemessenen Größen signifikant reduziert werden kann. Jeder dieser Fitparameter, üblicherweise als Störparameter bezeichnet, dient dabei der Beschreibung genau einer bestimmten systematischen Unsicherheit.

In dieser Masterarbeit werden zwei verschiedene Messungen im Detail vorgestellt, die beide Profile-Likelihood-Fits verwenden. Der erste Teil der Arbeit setzt sich mit

der Bestimmung des Wirkungsquerschnitts der  $Wt$ -Produktion von einzelnen Top-Quarks, sogenannten Single-Top-Quarks, auseinander, während die zweite Analyse eine Messung der Polarisation von  $W$ -Bosonen in Top-Quark-Paarzerfällen darstellt. Beide Analysen basieren auf dem  $Myon+Jets$ -Zerfallskanal. Besonderer Wert wird dabei auf die Untersuchung der Leistungsfähigkeit und möglicher Stärken von Profile-Likelihood-Fits, in dem verschiedene Einstellungen und Implementierungen des Fits nebst einiger Fitalgorithmen getestet werden, sowie auf eine sehr umfassende Validierung der Stabilität und der Modellbildung des Fits gelegt, Letzteres insbesondere in Zusammenhang mit der zweiten Analyse.

Im Rahmen der Masterarbeit wurde ein Programm entwickelt, um alle erforderlichen besagten Fits durchführen zu können. Das entstandene, flexible Programmwerkzeug kann direkt für andere vielversprechende Analysen, welche auf der Benutzung von Profile-Likelihood-Fits basieren, angepasst werden und in naher Zukunft entsprechend Verwendung finden.

# Contents

<b>1</b>	<b>Introduction</b>	<b>1</b>
<b>2</b>	<b>The Standard Model and the Role of the Top Quark Therein</b>	<b>5</b>
2.1	The Standard Model of Particle Physics . . . . .	5
2.1.1	Quarks, Leptons and Mediators . . . . .	6
2.1.2	Interactions and the Higgs Mechanism . . . . .	8
2.2	The Top Quark . . . . .	12
2.2.1	Top Quark Production . . . . .	12
2.2.2	Top Quark Decays . . . . .	18
2.2.3	Top Quark Properties . . . . .	21
2.2.4	W Boson Polarisation . . . . .	22
<b>3</b>	<b>The ATLAS Experiment</b>	<b>25</b>
3.1	The Large Hadron Collider . . . . .	25
3.2	Detector Observables and Coordinates . . . . .	27
3.3	The ATLAS Detector . . . . .	28
3.3.1	Inner Detector . . . . .	29
3.3.2	Calorimeter System . . . . .	30
3.3.3	Muon System . . . . .	32
3.3.4	Magnet System . . . . .	33
3.3.5	Trigger System . . . . .	34
<b>4</b>	<b>Profile Likelihood Analysis</b>	<b>35</b>
4.1	Why Profile Likelihood Fits? . . . . .	35
4.2	Mathematical Aspects of a Profile Likelihood Fit . . . . .	36
4.3	Profile Likelihood Analyses with Template Fits . . . . .	37
4.4	Interpolation Methods . . . . .	39
4.5	The Likelihood Function . . . . .	41
4.6	Remarks Concerning the Implementation of the Fit . . . . .	42
4.7	Examples of Profile Likelihood Analyses . . . . .	42
<b>5</b>	<b>Measurement of the <math>W_t</math> Production in the Muon+Jets Channel</b>	<b>43</b>
5.1	$W_t$ Production: Fundamentals of the Measurement . . . . .	43
5.1.1	Simulated Event Samples and Data Samples . . . . .	43
5.1.2	Definition of Physics Objects . . . . .	44
5.1.3	Event Selection . . . . .	46
5.1.4	Systematic Uncertainties . . . . .	46
5.1.5	Background Estimation . . . . .	48
5.1.6	Event Analysis and Likelihood Discriminant . . . . .	50
5.2	Profile Likelihood Fits to Measure the $W_t$ Production Cross-Section	52
5.2.1	Technical Aspects . . . . .	52
5.2.2	Nuisance Parameters and Other Fit Parameters . . . . .	53

5.2.3	Discriminant Distributions Used for the Fit . . . . .	54
5.2.4	Cross-Section Measurements with Profile Likelihood Fits . . .	54
5.3	Wt Production Cross-Section: Results . . . . .	55
5.3.1	Profile Likelihood Fits Using Background Parameters as Nuisance Parameters . . . . .	55
5.3.2	Scan of the Signal Parameter . . . . .	59
5.3.3	Scan of Nuisance Parameters . . . . .	60
5.3.4	Profile Likelihood Fits with Fewer Nuisance Parameters . . .	62
5.3.5	Additional Studies . . . . .	63
5.3.6	Pseudo-Experiments . . . . .	65
<b>6</b>	<b>Measurement of the W Boson Polarisation in the Muon+Jets Channel</b>	<b>67</b>
6.1	W Boson Polarisation: Fundamentals of the Measurement . . . . .	67
6.1.1	Simulated Event Samples . . . . .	67
6.1.2	Definition of Physics Objects . . . . .	68
6.1.3	W+jets Normalisation . . . . .	71
6.1.4	Fake Lepton Estimates . . . . .	71
6.1.5	Event Selection . . . . .	72
6.1.6	Event Reconstruction . . . . .	73
6.1.7	Systematic Uncertainties . . . . .	76
6.2	Profile Likelihood Fits to Measure the W Boson Polarisation . . . .	78
6.2.1	Technical Aspects . . . . .	78
6.2.2	Evaluating the Available Interpolation Methods . . . . .	80
6.2.3	Nuisance Parameters and Other Fit Parameters . . . . .	82
6.3	W Boson Polarisation: Results . . . . .	83
6.3.1	Evaluation of the Helicity Fractions and Their Uncertainties .	83
6.3.2	Overview of Profiled Systematic Uncertainties . . . . .	84
6.3.3	Pseudo-Experiments . . . . .	90
6.3.3.1	How to Perform Pseudo-Experiments . . . . .	90
6.3.3.2	Results of Pseudo-Experiments . . . . .	92
6.3.4	Fit Results . . . . .	102
6.3.5	Considering Additional Systematic Uncertainties . . . . .	108
6.3.6	Measurement of the Top Quark Pair Cross-Section . . . . .	113
<b>7</b>	<b>Summary and Conclusion</b>	<b>115</b>
<b>A</b>	<b>Additional Plots</b>	<b>119</b>
<b>B</b>	<b>Additional Studies Concerning the Measurement of the Wt Production Cross-Section</b>	<b>127</b>
<b>C</b>	<b>Additional Studies Concerning the Measurement of the W Boson Polarisation</b>	<b>129</b>
	<b>Nomenclature</b>	<b>133</b>
	<b>List of Figures</b>	<b>137</b>
	<b>List of Tables</b>	<b>139</b>
	<b>Bibliography</b>	<b>141</b>

# 1 Introduction

The question about the elementary constituents of matter, addressed at the most fundamental level, which is equivalent to the smallest possible scale of size, has bothered physicists for generations. The aim of this field of physics, called elementary particle physics, is thus the hunt for those fundamental constituents and all their possible interactions, which gathered pace especially over the last decades. This is mainly due to technological improvements which enable a direct search for these constituents, the elementary particles. Today's experiments in the field of particle physics, more than 100 years after the discovery of the electron, which might be said to constitute the beginning of elementary particle physics, are based on collisions of particles getting their high energy from accelerators.

Hence, the expression *High Energy Physics* is commonly used to describe such experiments with particle accelerators. The detection of the decay products coming from the collisions of heavily accelerated particles is necessary to draw inferences about the underlying processes and the involved particles, which includes, for example, a measurement of their properties.

With a decreasing scale of the observed processes, higher and higher energies and, as a result, larger and larger colliders are requested to accelerate particles before colliding. Nowadays, the *Large Hadron Collider* (LHC) at CERN is the world's most powerful particle accelerator designed to reach beam energies of up to 7 TeV. Those high energies allow to test the Standard Model of Elementary Particle Physics (SM) in more detail or to successfully search for the Higgs particle. Very recent studies verified the observation of a new particle at the LHC which is possibly the Higgs - approximately two years after detecting first collisions at a beam energy of 3.5 TeV [1, 2]. Additionally, the further exploration of this high energy region may unveil something completely unexpected, ordinarily specified as physics beyond the Standard Model (BSM).

At the LHC, among many other particles, large amounts of top quarks are produced. This quark plays a special role due to its rather short lifetime of about  $10^{-25}$  s and its comparatively large mass which is roughly of the order of the tungsten atom mass. Such properties were and are of strong interest since, for instance, measurements of the top quark mass served to limit the prediction of the Higgs boson mass or, furthermore, because the investigation of this quark as the heaviest one may result in indications of new and today unknown physics.

The intention of this master's thesis is to present two important measurements of top quark properties. They have been performed by using profile likelihood fits to extract, e.g., a certain signal out of a given data set. Such fits are usually based on the minimisation of a negative logarithmic likelihood function.

## 1 Introduction

Those measurements of top quark properties are usually challenging as different systematic uncertainties have to be considered. With increasing frequency, profile likelihood fits are used to ease the effort of such a demanding measurement. The most conspicuous characteristic of a profile likelihood fit, as employed in the analyses discussed in this thesis, is that a number of systematic variations are added to the minimisation process of the likelihood. For each single systematic uncertainty which enters the fit, an additional fit parameter, usually referred to as nuisance parameter, is applied. These nuisance parameters adjust the size of the underlying systematic effects allowing to constrain all these uncertainties with the help of the fit.

The studies on profile likelihood fits presented here are based on data which was recorded with the ATLAS detector at a centre-of-mass energy of  $\sqrt{s} = 7$  at the LHC in 2011. In the first part of this thesis, a measurement of the production rate of single top quarks in the so-called  $Wt$  production channel is shown. The focus is laid on the lepton+jets decay channel with a muon in the final state. In general, the production of single top quarks is interesting to analyse because it allows for a direct determination of  $|V_{tb}|$ , with  $V_{tb}$  as the corresponding CKM matrix element. The crucial aim of this part is to exemplify how to set up a profile likelihood analysis and to delineate its possible strengths so that it is especially concentrated on aspects like the description of the planning and the implementation of this measurement.

The second part is concerned with a measurement of the  $W$  boson polarisation in top quark pair decays using again the muon+jets channel. This measurement is a particular test of the  $Wtb$ -vertex Lorentz structure and associated couplings. The vertex is related to the predominant decay channel of top quarks to a high degree, which underlines its relevance. In order to measure the corresponding fractions of longitudinal, left-handed and right-handed polarisation, profile likelihood fits can be used as well. This second measurement covers many detailed and complex aspects of a very profound analysis in which the deeper understanding of the fitting method and the validation of the fit is in the centre of attention, in addition to fundamental information concerning profile likelihood fits.

In the next chapter, an introduction into fundamental aspects of the Standard Model of Particle Physics is given, followed by the presentation of some detailed information about top quarks and their properties. In the subsequent Chapter 3, the ATLAS detector and its different subsystems are briefly depicted whereas the profile likelihood analysis including its most significant features is introduced in Chapter 4.

Chapter 5 serves to present the measurement of the  $Wt$  production in the muon+jets channel. Some information about the fundamentals of the  $Wt$  production cross-section measurement - concerning, for instance, event selection and reconstruction, systematic uncertainties or the used likelihood discriminant - is given at the beginning of this chapter, followed by a more detailed description concerning profile likelihood fits in the context of the presented cross-section measurement and, subsequently, by a discussion of the performed studies and the obtained results. Chapter 6 is concerned with the measurement of the  $W$  boson polarisation in the muon+jets channel. The structure of this chapter can be compared to the precedent one. After the description of most important fundamentals including the object definition, the

event selection and reconstruction, a more detailed section about the profile likelihood analysis in the context of a measurement of the  $W$  boson polarisation follows. The obtained results and performed studies are presented afterwards; special emphasis is put on the validation and testing of the different fitting methods. Eventually, a summary of all performed analyses is delineated in Chapter 7 comprising a brief outlook.

Several additional studies concerning both measurements which allow for a cross-check of the obtained results are covered in App. B and App. C.

According to  $\hbar = c = 1$  in natural units, with  $\hbar$  as the reduced Planck constant and  $c$  as the speed of light, masses, energies and momenta are usually given in the unit of electronvolt, eV, in the upcoming chapters.

## *1 Introduction*

## 2 The Standard Model and the Role of the Top Quark Therein

Since this master's thesis serves to present several studies of top quark properties as they are predicted by the Standard Model of Particle Physics, the first part of this chapter summarises the fundamental aspects regarding the theoretical framework of this model. The top quark, its production channels and its decay modes are described in the second part. Special emphasis is put on different top quark properties as far as corresponding measurements are presented in this thesis.

### 2.1 The Standard Model of Particle Physics

The *Standard Model of Particle Physics*, which is usually denoted as Standard Model or simply SM, is a theory which emerged from the 1960s and 1970s and which characterises all known elementary particle interactions excluding gravity. It is nowadays the most precise theoretical framework to describe elementary particles, whose properties are measured to a large precision in a variety of experiments, as well as their interactions. The particles described by the SM are fermions (the so-called quarks and leptons) and bosons with the so-called force carriers or mediators, referred to as gauge bosons. The SM incorporates quantum electrodynamics (QED), the Glashow-Weinberg-Salam theory of electroweak processes [3–5] and finally quantum chromodynamics (QCD) [6–8].

Gauge bosons are responsible for mediating the different interactions between the initially massless quarks and leptons, whose mass is generated by the so-called Higgs mechanism, according to the laws of electroweak theory [9, 10]. In this context, the Higgs boson is a massive scalar elementary particle predicted by the Standard Model. The interactions between the Standard Model particles can be predicted by melding quantum mechanics as well as special relativity into a quantum field theory. The SM gives furthermore rise to conservation laws compliant with Noether's theorem since it rests on a combination of local gauge symmetries.

So far, the SM has met every experimental observation and test since the mid 20th century. It does, however, not include dark matter or gravitation as well as non-zero neutrino masses - even though these are specified by extensions - and is not able to solve the hierarchy problem. This results in a limitation of the validity of the Standard Model to energy scales at which gravity is small compared to the other three kinds of interactions introduced above.

These different aspects of the SM are illustrated in more detail in the following subchapters.

### 2.1.1 Quarks, Leptons and Mediators

Pursuant to the Standard Model, all matter is made of three kinds of elementary particles, as depicted in the introductory paragraph: *leptons*, *quarks* and *bosons*. Quarks and leptons are summarized to *fermions* as they constitute both spin-1/2-particles whereas the bosons, which comprise the mediators or also called gauge bosons and the Higgs particle, carry integer spin.

Six leptons and six “flavours” of quarks can be distinguished in total. Leptons as well as quarks are grouped into three *generations* or families with increasing masses. This also applies to antifermions having the same mass as the related particle - as long as *CPT* (*charge parity time*) is conserved - but opposite electric charge. The six leptons are classified by charge  $Q$ , electron number  $L_e$ , muon number  $L_\mu$  and tau number  $L_\tau$ . All six quarks flavours are defined similarly by charge, upness  $U$ , downness  $D$ , strangeness  $S$ , charm  $C$ , bottomness  $B$  and topness  $T$  [11].

Under consideration of chirality and handedness, it can be deduced that all quarks and leptons form left-handed *doublets* but right-handed *singlets*. The three generations of left-handed leptons can thus be arranged according to:

$$\begin{pmatrix} \nu_e \\ e \end{pmatrix}_L, \quad \begin{pmatrix} \nu_\mu \\ \mu \end{pmatrix}_L, \quad \begin{pmatrix} \nu_\tau \\ \tau \end{pmatrix}_L.$$

All lepton generations are composed of an electrically neutral neutrino  $\nu_i$  and a lepton  $\ell = e, \mu, \tau$  with negative charge  $Q = -e$  while the left-handed up-type quarks ( $u, c, t$ ) with charge  $Q = 2/3 \cdot e$  and the left-handed down-type quarks ( $d, s, b$ ) with negative charge  $Q = -1/3 \cdot e$  are arranged as follows:

$$\begin{pmatrix} u \\ d' \end{pmatrix}_L, \quad \begin{pmatrix} c \\ s' \end{pmatrix}_L, \quad \begin{pmatrix} t \\ b' \end{pmatrix}_L.$$

The weak eigenstates ( $d', s', b'$ ) cited in the left-handed doublets have to be distinguished from the mass eigenstates representing the “physical” quarks  $d, s$  and  $b$ .

As long as the mixing of the first two quark generations is taken into account, the coefficients of these weak eigenstates which are linear combinations of the mass eigenstates can be put in a two-dim. matrix, the Cabibbo matrix with the Cabibbo angle. In 1973, KOBAYASHI and MASKAWA universalised this Cabibbo scheme to handle all three existing quark generations so that the weak eigenstates are connected with the physical quark states by the  $3 \times 3$  *CKM matrix* denoted as  $V$  [12]:

$$\begin{pmatrix} d' \\ s' \\ b' \end{pmatrix} = \begin{pmatrix} V_{ud} & V_{us} & V_{ub} \\ V_{cd} & V_{cs} & V_{cb} \\ V_{td} & V_{ts} & V_{tb} \end{pmatrix} \cdot \begin{pmatrix} d \\ s \\ b \end{pmatrix}.$$

This unitary matrix  $V$  is characterised by three real parameters and one imaginary phase factor, which, in turn, causes *CP* (*charge parity*) violation [13, 14].

Analogous to the CKM matrix, a correspondent matrix can be defined for the lepton sector, the Pontecorvo–Maki–Nakagawa–Sakata (PMNS) matrix. This matrix was introduced primarily to describe neutrino oscillations mathematically [15, 16].

## 2.1 The Standard Model of Particle Physics

All SM particles introduced above are listed in Table 2.1. Several particle properties according to the caption are added [11, 13]. The *weak hypercharge*  $Y$  is defined as  $Y = 2(Q - T_3)$ . For the sake of completeness, the gauge bosons are also included in the table although they are described more extensively in Subsection 2.1.2.

Particles		Q [e]	C	s	$T_3$	Y
Leptons	$\begin{pmatrix} \nu_e \\ e \end{pmatrix}_L$	$\begin{pmatrix} 0 \\ -1 \end{pmatrix}$	-	$\frac{1}{2}$	$\begin{pmatrix} +\frac{1}{2} \\ -\frac{1}{2} \end{pmatrix}$	-1
	$\begin{pmatrix} \nu_\mu \\ \mu \end{pmatrix}_L$	$\begin{pmatrix} 0 \\ -1 \end{pmatrix}$	-	$\frac{1}{2}$	$\begin{pmatrix} +\frac{1}{2} \\ -\frac{1}{2} \end{pmatrix}$	-1
	$\begin{pmatrix} \nu_\tau \\ \tau \end{pmatrix}_L$	$\begin{pmatrix} 0 \\ -1 \end{pmatrix}$	-	$\frac{1}{2}$	$\begin{pmatrix} +\frac{1}{2} \\ -\frac{1}{2} \end{pmatrix}$	-1
Quarks	$e_R$	-1	-	$\frac{1}{2}$	0	-2
	$\mu_R$	-1	-	$\frac{1}{2}$	0	-2
	$\tau_R$	-1	-	$\frac{1}{2}$	0	-2
	$\begin{pmatrix} u \\ d' \end{pmatrix}_L$	$\begin{pmatrix} +\frac{2}{3} \\ -\frac{1}{3} \end{pmatrix}$	r,g,b	$\frac{1}{2}$	$\begin{pmatrix} +\frac{1}{2} \\ -\frac{1}{2} \end{pmatrix}$	$+\frac{1}{3}$
	$\begin{pmatrix} c \\ s' \end{pmatrix}_L$	$\begin{pmatrix} +\frac{2}{3} \\ -\frac{1}{3} \end{pmatrix}$	r,g,b	$\frac{1}{2}$	$\begin{pmatrix} +\frac{1}{2} \\ -\frac{1}{2} \end{pmatrix}$	$+\frac{1}{3}$
	$\begin{pmatrix} t \\ b' \end{pmatrix}_L$	$\begin{pmatrix} +\frac{2}{3} \\ -\frac{1}{3} \end{pmatrix}$	r,g,b	$\frac{1}{2}$	$\begin{pmatrix} +\frac{1}{2} \\ -\frac{1}{2} \end{pmatrix}$	$+\frac{1}{3}$
Gauge Bosons	Photon $\gamma$	0	-	1	0	0
	$Z^0$	0	-	1	0	0
	$W^\pm$	$\pm 1$	-	1	$\pm 1$	0
	8 Gluons $g$	0	r,g,b	1	0	0
Higgs Boson		0	-	0	$-\frac{1}{2}$	+1

Table 2.1: Particles and mediators in the Standard Model. The particle properties electric charge  $Q$ , colour  $C$ , spin  $s$ , the third component  $T_3$  of weak isospin  $T$  as well as weak hypercharge  $Y$  are listed [11, 13].

Quarks, except for top quarks, as shown in Chapter 2.2.3, form *hadrons* which are categorised into *baryons* having an odd half-integral spin and *mesons* carrying integer spin. All quarks are not able to act as free particles which is denoted as *confinement* [11].

The masses of the different fermions vary over a broad range. In Table 2.2, masses of all leptons and fermions are listed, showing that the top quark mass is by far the largest. This makes the top quark so special in the framework of the Standard Model, which is explained in more detail in Section 2.2.

Lepton	Mass $m$ in [MeV/ $c^2$ ]	Quark	Mass $m$ in [MeV/ $c^2$ ]
$e$	0.510998928(11)	$u$	$2.3^{+0.7}_{-0.5}$
$\mu$	105.6583715(35)	$c$	$1275 \pm 25$
$\tau$	1776.82(16)	$t$	$173500 \pm 600 \pm 800$
$\nu_e$	$< 2 \cdot 10^{-6}$	$d$	$4.8^{+0.7}_{-0.3}$
$\nu_\mu$	$< 0.19$	$s$	$95 \pm 5$
$\nu_\tau$	$< 18.2$	$b$	$4180 \pm 30$

Table 2.2: Masses of fermions as given in [13]. More information concerning the top quark value is given in Section 2.2.3.

### 2.1.2 Interactions and the Higgs Mechanism

The Standard Model comprises three elementary particle interactions: electromagnetic, weak and strong ones. As mentioned in the introductory part of this chapter, the SM is a gauge theory which means that *local gauge symmetries* serve to characterise these interactions. Hence, the *Lagrangian* is locally invariant under a transformation of a specific gauge group. This group is also a so-called *Lie group*. To be more accurate, local gauge symmetries can be mathematically expressed with the help of unitary and special unitary Lie groups, denoted as  $U$  and  $SU$ , respectively. The number of gauge fields which correspond to a certain interaction, that conforms with the number of generators of a group, is  $n^2$  ( $U(n)$  group) or  $n^2 - 1$  ( $SU(n)$  group). The latter number  $n^2 - 1$  is equivalent to the dimension of a group of order  $n$ .

Electromagnetic interactions can be expressed by the Lie group  $U(1)_{\text{em}}$ . Together with a spinor field  $\phi$  and a real number  $\theta$ , the corresponding phase transformation is  $\phi \rightarrow \phi' = e^{i\theta}\phi$ . A  $SU(2)$  group serves to describe weak interactions. This group is generated by the three *Pauli matrices*  $\sigma_i$  with  $i = 1, 2, 3$ . The underlying phase transformation is  $\phi \rightarrow \phi' = e^{i\vec{\sigma}\vec{\alpha}}\phi$  with  $\vec{\alpha} = (\alpha_1, \alpha_2, \alpha_3)$  where  $\alpha_1, \alpha_2, \alpha_3 \in \mathbb{R}$ . The associated massless gauge fields are denoted as  $W_\mu^i$ . Electroweak theory [3–5] combines both weak and electromagnetic interactions to the symmetry group  $SU(2)_L \otimes U(1)_Y$  with the index  $L$  implying that the weak isospin current couples only to left-handed fermions and the index  $Y$  denoting the weak hypercharge, which is the generator of  $U(1)_Y$ . This group contains a massless gauge field referred to as  $B_\mu$ .  $U(1)_{\text{em}}$  is a subgroup of this group [17].

The group  $SU(2)_L \otimes U(1)_Y$  is composed of an isotriplet of the vector fields  $W_\mu^i$  with a coupling strength  $g$ , a weak isospin current  $J_\mu^i$  and the single vector field  $B_\mu$ . The latter couples to the weak hypercharge current  $j_\mu^Y$  with a strength commonly denoted as  $\frac{g'}{2}$ . The basic electroweak interaction can then be written as:

$$-i \cdot g(J^i)^\mu W_\mu^i - i \cdot \frac{g'}{2}(j^Y)^\mu B_\mu.$$

The gauge bosons are obtained as linear combinations of the different gauge fields. In this context, the so-called *Weinberg angle* or *weak mixing angle*  $\theta_W$  specifies the mixing between the groups  $SU(2)_L$  and  $U(1)_Y$ . The definition is as follows:

$$\sin \theta_W = \frac{g'}{\sqrt{g^2 + g'^2}} \quad \text{or accordingly:} \quad \tan \theta_W = \frac{g'}{g}.$$

The angle is measured to be  $\sin^2 \theta_W = 0.23116(12)$  [13] and associates furthermore the electromagnetic charge with the coupling constants  $g$  and  $g'$ :  $e = g \cdot \sin \theta_W = g' \cdot \cos \theta_W$ . The two neutral gauge bosons,  $\gamma$  and  $Z^0$  as the mediators of the neutral currents of electromagnetism and weak interactions, can be expressed by  $W_\mu^3$  and  $B_\mu$  representing neutral fields as:

$$\begin{aligned} A_\mu &= B_\mu \cos \theta_W + W_\mu^3 \sin \theta_W & (\text{boson } \gamma), \\ Z_\mu &= -B_\mu \sin \theta_W + W_\mu^3 \cos \theta_W & (\text{boson } Z^0). \end{aligned}$$

Finally, the fields  $W_\mu^\pm$  serve to characterise the charged bosons as follows:

$$W_\mu^\pm = \sqrt{\frac{1}{2}}(W_\mu^1 \mp i \cdot W_\mu^2) \quad (\text{charged bosons } W^\pm).$$

As they are described by linear combinations of massless gauge fields, all these four gauge bosons are massless in the model of electroweak interactions. The corresponding Lagrangian is of the following form:

$$\begin{aligned} \mathcal{L}_{\text{EW}} = & -\frac{1}{4}W_{\mu\nu}^i W_i^{\mu\nu} - \frac{1}{4}B_{\mu\nu}B^{\mu\nu} \\ & + \bar{L}\gamma^\mu(i\partial_\mu - g\frac{\sigma_i}{2}W_\mu^i - \frac{g'}{2}YB_\mu)L + \bar{R}\gamma^\mu(i\partial_\mu - \frac{g'}{2}YB_\mu)R. \end{aligned}$$

The first two terms describe the interactions between the gauge fields themselves, the last terms are used to express the interactions between the particles that are mediated by the corresponding gauge bosons. The wave functions  $L$  and  $R$  signify a left-handed fermion doublet and a right-handed fermion singlet, according to their notation.

Experiments have proven that the  $W^\pm$  and  $Z^0$  bosons (commonly written as  $W$  and  $Z$ ) are massive. Massive gauge bosons cause a symmetry breaking of the  $SU(2)_L \otimes U(1)_Y$  group and the electroweak model needs to be extended: The Higgs mechanism with the so-called Higgs boson, briefly introduced in the following, serves to generate the particle masses in a gauge invariant way [9, 10].

Explicit mass terms cannot be added to the Lagrangian since this would infringe gauge invariance and inhibit renormalisability. However, spontaneous symmetry breaking of the electroweak symmetry allows for a consistent incorporation of gauge boson masses. As a consequence, the Lagrangian is kept gauge invariant, as desired, and solely the symmetry of the vacuum is broken.

The starting point is an appropriate choice of a Higgs field. To formulate the Higgs mechanism, four real scalar fields  $\phi_k$  belonging to  $SU(2) \times U(1)$  are used. The four fields are arranged in an isospin doublet with weak hypercharge  $Y = 1$ , written as:

$$\phi = \begin{pmatrix} \phi^+ \\ \phi^0 \end{pmatrix} \quad \text{with} \quad \begin{aligned} \phi^+ &= (\phi_1 + i\phi_2)/\sqrt{2}, \\ \phi^0 &= (\phi_3 + i\phi_4)/\sqrt{2}. \end{aligned}$$

The symmetry breaking is caused by this complex scalar doublet and gives rise to an additional term in the Lagrangian, which is:

$$\mathcal{L}_{\text{Higgs}} = (D_\mu\phi)^\dagger(D^\mu\phi) - V(\phi^\dagger\phi) \quad \text{with} \quad V(\phi^\dagger\phi) = \mu^2\phi^\dagger\phi + \lambda(\phi^\dagger\phi)^2,$$

where  $D_\mu$  constitutes a covariant derivative.  $V(\phi^\dagger\phi)$  represents the Higgs potential depending only on the combination  $\phi^\dagger\phi$  and defined by the choice of the parameters  $\mu$  and  $\lambda$ . With  $\mu^2 < 0$  and  $\lambda > 0$  the vacuum expectation value  $v$  is given by  $v^2 = -\mu^2/\lambda$ . Then, an appropriate ground state  $\phi_0(v)$  needs to be chosen.

If  $v \neq 0$ , spontaneous symmetry breaking around the minimum occurs, responsible for the creation of a real massive boson that can be identified with the Higgs boson

## 2 The Standard Model and the Role of the Top Quark Therein

with spin 0 and a mass of  $m_H^2 = 2v^2\lambda$ . The Higgs mechanism induces that gauge bosons acquire a mass which can be written in terms of the vacuum expectation value  $v$ :

$$m_W = \frac{1}{2}vg \quad \text{and} \quad m_Z = \frac{1}{2}v\sqrt{g^2 + g'^2}.$$

On the other hand, the photon mass is zero,  $m_\gamma = 0$ , as desired. Since the parameters  $\mu$  and  $\lambda$  are unknown, the Higgs mass cannot be constrained or even predicted by this theory. Current measurements based on data collected with the ATLAS and the CMS detector at the LHC yielded, if the recently observed boson is in fact the Higgs particle, Higgs masses of  $m_H = 126.0 \pm 0.4$  (stat.)  $\pm 0.4$  (syst.) GeV [1] and  $m_H = 125.3 \pm 0.4$  (stat.)  $\pm 0.5$  (syst.) GeV [2], respectively.

Apart from the masses of gauge bosons, the Higgs mechanism also generates those of all fermions. They couple to the Higgs field with the *Yukawa coupling*, labelled as  $y_f$  and constituting another parameter of the SM. After adding another corresponding term to the SM Lagrangian, the calculation of the fermion masses can be performed and results in the following expression:

$$m_f = \frac{1}{\sqrt{2}}vy_f.$$

The Yukawa coupling of the top quark is  $y_t \approx 1$ , much larger than those of the other quarks. This is due to the fact that the top quark is the fermion with the highest mass, as shown in Table 2.2, resulting in such a large coupling to the Higgs field.

Quantum chromodynamics or QCD describes strong interactions with the symmetry group  $SU(3)_C$ , generated with the help of the eight *Gell-Mann matrices*  $\lambda_a$  with  $a = 1, \dots, 8$ . Conventionally, the eight generators are chosen to be  $T_a = \lambda_a/2$ . As the gluon is the related gauge boson, eight gluon fields  $G_\mu^a$  exist that carry colour charge themselves, denoted by the index  $C$ . Three different kinds of colour, as the quantum number of the strong interaction, arise: red, blue and green (and the corresponding anticolours). It is noteworthy that the invariance under transformations of the group  $SU(3)_C$  does merely apply to colourless bound states.

Together with the gluon fields, the coupling constant  $g_s$ , the mass  $m$ , the respective covariant derivative and the quark field  $q$ , the Lagrangian of QCD is finally of the following form:

$$\mathcal{L}_{\text{QCD}} = \bar{q}(i\gamma^\mu\partial_\mu - m)q - g_s\bar{q}\gamma^\mu T_a q G_\mu^a - \frac{1}{4}G_{\mu\nu}^a G_a^{\mu\nu}.$$

The different  $G_{\mu\nu}^a$  denote field strength tensors and contain a term which specifies the self-interaction between the gauge bosons because these gluons carry colour charge themselves.

## 2.1 The Standard Model of Particle Physics

Eventually, the electroweak as well as the strong interactions can be joined together to form the *Standard Model Symmetry Group*:

$$SU(3)_C \otimes SU(2)_L \otimes U(1)_Y.$$

The different mediators, as they have been introduced in this subchapter and their properties are listed in Table 2.3. The theory which describes the corresponding interactions is given as well. In contrast to all other fundamental forces, the strong force increases with distance. The underlying effect, the so-called *quark confinement*, explains why free quarks - quarks outside of bound states - cannot be observed. Hence, it is not possible to separate quarks from each other with increasing energies, however, the creation of an additional pair of quarks with opposite colour charge gets energetically preferred then. As a result, new bound states emerge which include the original quarks. Consequently, quarks originating from high energy collisions form jets of hadrons while diverging from the collision point. This does not apply to top quarks, as mentioned above and explained in the next subsection [11, 17].

Force	Strong	Electromagnetic	Weak
Theory	Chromodynamics	Electrodynamics	Flavourdynamics
Mediator	Gluon	Photon	$W, Z$
El. Charge [ $e$ ]	0	0	$Q_W = \pm 1$ $Q_Z = 0$
Colour	8 comb.	-	-
Coupl. Const.	$\alpha_s(m_Z) \approx 0.1184$	$\alpha_{em} \approx 0.0073$	$\alpha_w \approx 0.0316$
Mass [ $\text{GeV}/c^2$ ]	0	$< 10^{-27}$	$m_W = 80.385 \pm 0.015$ $m_Z = 91.1876 \pm 0.0021$

Table 2.3: The three fundamental forces incorporated in the Standard Model and their properties [11, 13].  $m_W$  and  $m_Z$  refer to the masses and  $Q_W$  and  $Q_Z$  to the electric charge of the corresponding bosons. The coupling constants  $\alpha_i$  and  $g_i$  for the different forces  $i$  are related to each other [17].

Even though SM predictions could be validated successfully over the last years and although latest LHC results indicate that a recently discovered boson [1, 2] may be the Higgs particle, the Standard Model cannot be regarded as a complete theory. Several shortcomings were listed at the beginning of this chapter. Nevertheless, various theories emerged to solve the still existing problems of the Standard Model, which rest on various types of new particles or even new kinds of interactions which can possibly be observed at the LHC. Some often discussed theories involve additional dimensions, supersymmetry or, for example, technicolor models.

## 2.2 The Top Quark

The bottom quark, as the fifth quark, was experimentally verified in 1977 [18]. Consequently, another quark, the so-called top quark, with which the bottom quark forms the third quark generation was predicted to exist. But this heaviest of all quarks could only be observed with the high collision energies reached at the Tevatron collider. It was thus first detected in 1995 - due to its unique properties a long time after its prediction and after the discovery of all other SM quarks: The quark was discovered in  $t\bar{t}$  production by both the CDF and DØ experiment at Tevatron Run I - in proton-antiproton  $p\bar{p}$  collisions at a centre-of-mass energy of  $\sqrt{s} = 1.8$  TeV [19, 20]. It took another 14 years until 2009 before those two collaborations could confirm that the observation of electroweak production of single top quarks at Tevatron Run II at  $\sqrt{s} = 1.96$  TeV succeeded [21, 22].

Due to its large mass, the top quark is expected to play a special role in electroweak symmetry breaking mechanisms. Apart from that, this quark can also be able to provide a sign of physics beyond the SM which stresses the importance of measuring its properties in more detail. Possible production mechanisms and decay schemes of the top quark are presented in the following before properties of the top quark are discussed - with special attention paid to single top quarks and the explanation of  $W$  boson helicities.

### 2.2.1 Top Quark Production

Top quarks are produced either as a single quark or as  $t\bar{t}$  pairs whereby the latter production process occurs much more frequently. Before the production mechanisms are explained in more detail, the QCD factorisation theorem is introduced.

**Top Quark Production: The QCD Factorisation Theorem** Perturbative quantum chromodynamics (pQCD) describes top pair production at high energy interactions of proton-antiproton  $p\bar{p}$  (at the Tevatron) or proton-proton  $pp$  (at the LHC) collisions. These hard scattering processes originate from the interaction between quarks and gluons, that constitute the components of both colliding hadrons. Those quarks and gluons are usually summarised to partons which are in fact the interacting particles in hadron-hadron colliders.

To estimate the cross-section of top quark events, here exemplarily shown for top quark pairs, parton distribution functions (PDFs)  $f_i(x_i, Q^2)$  are needed, which describe the probability density for observing a parton  $i$  having a momentum fraction  $x_i$  at momentum transfer  $Q^2$  within a hadron [23–25]. The cross-section of two incoming and colliding partons  $i$  and  $j$ , denoted as  $\hat{\sigma}^{ij \rightarrow t\bar{t}}$ , is then convolved with the PDFs  $f_i$  and  $f_j$ , which are calculated at a so-called factorisation scale  $Q^2 = \mu_F^2$ .  $\mu_R$  is a further introduced scale, a renormalisation scale, which is, like  $\mu_F$ , chosen to correspond to the energy scale of the analysed collision. To evaluate a cross-section involving top quarks, it is commonly set:  $m_t = \mu_F = \mu_R$ . Regarding the LHC with its proton-proton collisions, the  $t\bar{t}$  cross-section with the top quark mass  $m_t$ , the centre-of-mass energy of the  $pp$  collision  $\sqrt{s}$  and of the parton-parton collision  $\sqrt{\hat{s}}$

can be written as [26, 27]:

$$\sigma^{pp \rightarrow t\bar{t}}(\sqrt{s}, m_t) = \sum_{i,j=g,q,\bar{q}} \int dx_i dx_j f_i(x_i, \mu_F^2) f_j(x_j, \mu_F^2) \cdot \hat{\sigma}^{ij \rightarrow t\bar{t}}(m_t, \sqrt{\hat{s}}, x_i, x_j, \alpha_s(\mu_R^2), \mu_R^2).$$

In general terms, this relation is usually referred to as *QCD factorisation theorem*.

**Top-Antitop Quark Pairs**  $t\bar{t}$  pairs are produced via the strong interaction by  $q\bar{q}$  annihilation or via  $gg$  fusion with a quark  $q$  and an antiquark  $\bar{q}$ . Three leading order Feynman diagrams can be distinguished for gluon fusion  $gg \rightarrow t\bar{t}$  while one Feynman diagram visualises the reaction  $q\bar{q} \rightarrow t\bar{t}$ . The diagrams are shown in Fig. 2.1.

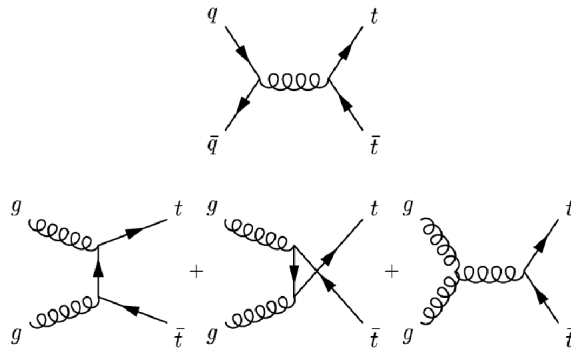


Figure 2.1:  $t\bar{t}$  production via the strong interaction. Four lowest order Feynman diagrams of both  $q\bar{q}$  annihilation (top) and gluon fusion (bottom) are depicted [27].

The production cross-section of these processes rises with increasing energy of the colliding particles. This can be seen in Fig. 2.2 in which the cross-sections of different important physics processes are shown as a function of the centre-of-mass energy. The given top quark cross-section includes the production of top quark pairs and single top quarks. This top quark production cross-section at the design centre-of-mass energy of the LHC exceeds the value which could be measured at the Tevatron by far. Consequently, the LHC experiments are able to acquire a huge amount of events in which top quarks are involved. However, Fig. 2.2 also reveals that the cross-section of several other Standard Model processes is much larger than the one of top quarks complicating a detection.

In order to determine the total cross-section  $\sigma_{t\bar{t}}$  of top quark pairs, several different theoretical calculations at the precision of approximate next-to-next-to-leading order (NNLO) or of next-to-next-to-leading logarithmic (NNLL) order exist, which use different techniques for the higher order approximation.  $\sigma_{t\bar{t}}$  depends on the top quark mass  $m_t$  and is evaluated for values of this mass which is close to the current world average. The NNLO result for  $t\bar{t}$  production at the Tevatron at  $\sqrt{s} = 1.96$  TeV is:  $7.07^{+0.36}_{-0.39}$  pb [28] based on a top quark mass of  $173 \text{ GeV}/c^2$ , the result for the LHC at  $\sqrt{s} = 7$  TeV amounts to:  $166.8^{+16.5}_{-17.8}$  pb [29] using the tool HATHOR [30]. This prediction rests on an assumed top quark mass of  $172.5 \text{ GeV}/c^2$ .

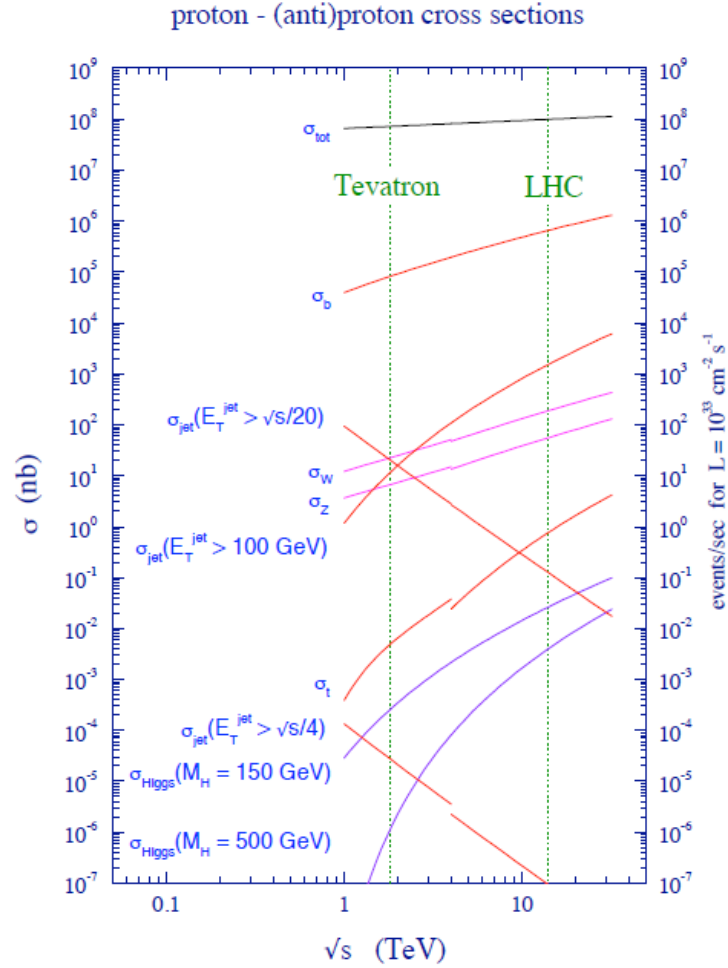


Figure 2.2: Cross-sections of various physics processes in  $p\bar{p}$  and  $pp$  collisions at the Tevatron and the LHC, respectively. The corresponding luminosities are given as well. The vertical lines represent the centre-of-mass energy at the Tevatron during its Run II and the design centre-of-mass energy at the LHC which amounts to  $\sqrt{s} = 14$  TeV. The top quark production cross-section is referred to as  $\sigma_t$  and includes  $t\bar{t}$  as well as single top quark events. At lower energies, the cross-section based on  $p\bar{p}$  collisions is given, the one based on  $pp$  collisions is shown at higher energies. The step in the  $\sigma_t$ -curve between these regions describing  $p\bar{p}$  and  $pp$  collisions at  $\sqrt{s} = 4$  TeV arises due to the fact that valence quarks instead of sea quarks - which are less likely to occur - contribute to  $q\bar{q}$  annihilation in  $p\bar{p}$  collisions [31].

A certain parton momentum fraction  $x$  is needed for the production of a  $t\bar{t}$  pair at a fixed value of  $\sqrt{s}$ .  $x$ , as the ratio of a parton momentum to the total momentum, decreases with growing energy and is also called Bjorken- $x$ . At small values of  $x$ , the values of the parton density distributions of both quarks and gluons increase. As the growth in the parton densities of gluons is greater than the increase in the parton densities of quarks, not only the overall  $t\bar{t}$  cross-section rises but also the parton density values of quarks are outvalued by those of gluons with larger and larger centre-of-mass energies. That is why  $q\bar{q}$  annihilation predominates the  $t\bar{t}$  production at the Tevatron while at the LHC, caused by its higher centre-of-mass energy in comparison to the Tevatron,  $t\bar{t}$  pairs are predominantly produced via  $gg$  fusion.

The different ratios between the contributions of two production mechanisms at the Tevatron and at the LHC are further reinforced due to the following circumstance: In  $pp$  collisions, the antiquark  $\bar{q}$  in the initial state of  $q\bar{q}$  annihilation needs to be a sea quark, whereas it may be a valence quark included in the antiproton in  $p\bar{p}$  collisions. Such a valence quark occurs with a higher frequency - independent of the centre-of-mass energy. Hence,  $q\bar{q}$  annihilation is further suppressed at a  $pp$  collider in comparison to a  $p\bar{p}$  collider [27, 32].

Different parton distribution functions (PDFs) are shown in Fig. 2.3 revealing that for smaller fractions  $x$  the gluon function exceeds all considered quark PDFs while only for very large  $x$  the up and down quark functions from the proton are dominant - in compliance with the above explanations.

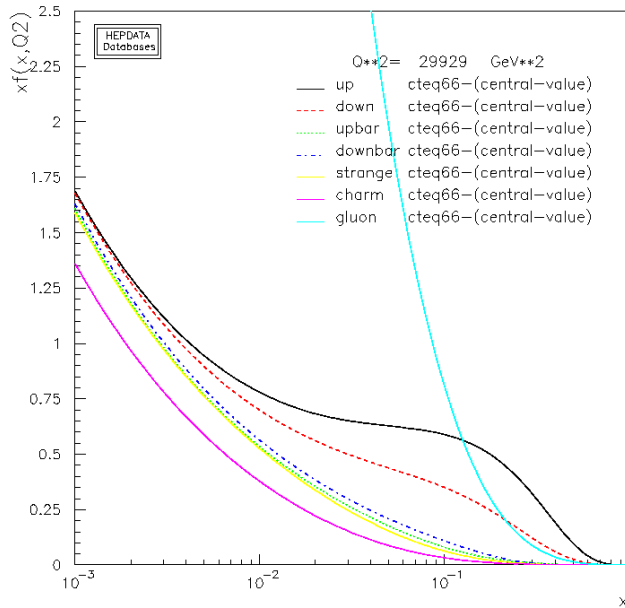


Figure 2.3: Different parton distribution functions (PDFs) for protons at the scale  $Q^2 = m_t^2$  with a top quark mass of  $m_t = 173 \text{ GeV}/c^2$ . The plot can be produced with a tool available at [33]. The illustrated functions are based on the CTEQ66 PDF set [34].

At Tevatron Run II with  $\sqrt{s} = 1.96$  TeV, 85% of all top quark pairs were produced via  $q\bar{q}$  annihilation, 15% originated from gluon fusion. At the LHC, when it reaches the design centre-of-mass energy of  $\sqrt{s} = 14$  TeV, about 90% of all  $t\bar{t}$  pairs are expected to be produced via gluon fusion, the remaining 10% via quark-antiquark annihilation. At a centre-of-mass energy of  $\sqrt{s} = 7$  TeV, on which the measurements presented in this thesis are based, the gluon fusion rate exceeds the  $q\bar{q}$  annihilation rate with a ratio of roughly 80%:20%.

Measurements of the  $t\bar{t}$  production cross-section with the ATLAS detector at  $\sqrt{s} = 7$  TeV have already been performed in a variety of channels. A current combination of measurements in the dilepton, the single lepton and the all-hadronic (see below) final states leads to:  $\sigma_{t\bar{t}} = 177 \pm 3$  (stat.) $^{+8}_{-7}$  (syst.)  $\pm 7$  (lumi.) pb [35].

A combination of cross-section measurements with the CMS detector results in:  $\sigma_{t\bar{t}} = 165.8 \pm 2.2$  (stat.)  $\pm 10.6$  (syst.)  $\pm 7.8$  (lumi.) pb [36], at the same centre-of-mass energy using the same decay channels.

In 2012, the LHC runs at a centre-of-mass energy of  $\sqrt{s} = 8$  TeV so that the corresponding cross-section measurements will reveal larger values.

**Single Top Quarks** The production of a single top quark is realisable through the weak interaction via three different subprocesses that are displayed in Fig. 2.4. The virtuality of the exchanged boson allows for a distinction between these three processes. In the  $t$ - or  $s$ -channel, for example, the  $W$  boson is the mediator of single top processes. The Feynman diagrams visualising these processes at lowest order (LO) can be found in Fig. 2.4a and Fig. 2.4c, respectively. The predominant production mechanism is the  $t$ -channel production, characterised by the exchange of a virtual  $W$  boson. The  $Wt$  process constitutes the associated production of an on-shell  $W$  boson and a single top quark and is shown in Fig. 2.4b. It has the second largest cross-section whereas the  $s$ -channel Drell-Yan type production contributes comparatively little to the entire single top cross-section. The  $t$ -channel production rate has been determined at the Tevatron [37, 38] while the  $Wt$  process, usually referred to as  $Wt$  production, has never been observed before the LHC started operating.

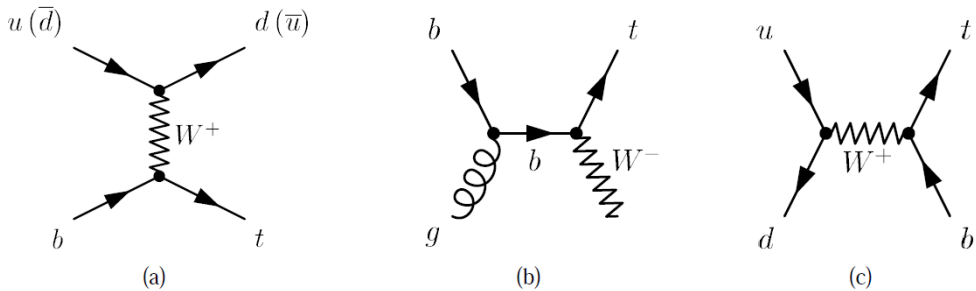


Figure 2.4: Single top quark production via the weak interaction. The lowest order (LO) Feynman diagrams of (a)  $t$ -channel production, (b) associated  $Wt$  production and (c)  $s$ -channel production are given [39].

Approximate next-to-next-to-leading order (NNLO) calculations can be exploited to evaluate the cross-sections of the three different processes introduced above and illustrated in Fig. 2.4 and used to predict the numbers of produced single top events - depending on the assumed top quark mass [40–42]. Since the measurement of the  $Wt$  production rate is studied in this thesis later on, the computed cross-sections are listed in Table 2.4.

Production Process	$t$ -channel	$Wt$	$s$ -channel
Cross-section $\sigma$ [pb]	$64.57^{+3.32}_{-2.62}$	$15.74^{+1.34}_{-1.36}$	$4.63^{+0.29}_{-0.27}$

Table 2.4: Predictions for single top quark production cross-sections for the top mass  $m_t = 172.5 \text{ GeV}/c^2$  for all three production processes shown in Fig. 2.4 and obtained from [40–42].

The sum over all individual three single top quark cross-sections listed here results in the total single top production cross-section which amounts to approximately half of the  $t\bar{t}$  cross-section, compared to the values shown in the last paragraph. A comparison of the numbers thus reveals that both values are of the same order of magnitude, but isolating a single top event from background processes is more challenging because fewer jets occur in the corresponding event. This explains why single top production processes were only observed 14 years after the discovery of the top quark in  $t\bar{t}$  production [37, 38]. Another aspect concerning single top quark production is that more top quarks than antitop quarks are produced at the LHC since it is a proton-proton collider and antitop quarks solely originate from sea quarks.

A recent measurement performed with the ATLAS detector at  $\sqrt{s} = 7 \text{ TeV}$  results in a  $Wt$  production cross-section of:  $\sigma_{Wt} = 16.8 \pm 2.9 \text{ (stat.)} \pm 4.9 \text{ (syst.) pb}$  [43], while the current measurement of the  $t$ -channel production with the ATLAS detector at  $\sqrt{s} = 7 \text{ TeV}$  yielded:  $\sigma_{t\text{-ch.}} = 83 \pm 4 \text{ (stat.)}^{+20}_{-19} \text{ (syst.) pb}$  [44]. For the  $t$ -channel, CMS results are also available as well, the cross-section at a centre-of-mass energy amounts to:  $\sigma_{t\text{-ch.}} = 70.2 \pm 5.2 \text{ (stat.)} \pm 10.4 \text{ (syst.)} \pm 3.4 \text{ (lumi.) pb}$  [45].

### 2.2.2 Top Quark Decays

In contrast to the top quark production with all its different channels, the decay of the top quark is less diverse: Top quarks always decay into a down-type quark and a  $W$  boson via the weak interaction. The probability for the down-type quarks to act as decay products of the top quark decay is expressed by the different CKM matrix elements which comprise top quarks. According to the measured value of  $|V_{tb}|$ , as given in Section 2.2.3, the top quark decays almost exclusively into a  $W^+$  boson and a  $b$  quark, the antitop quark into a  $W^-$  boson and an antibottom quark. This fact can also be expressed in terms of branching ratios, considering the unitarity of the CKM matrix and three generations of quarks:

$$\frac{\mathcal{B}(t \rightarrow Wb)}{\mathcal{B}(t \rightarrow Wq)} = \frac{|V_{tb}|^2}{|V_{td}|^2 + |V_{ts}|^2 + |V_{tb}|^2} = |V_{tb}|^2 \approx 1, \quad (2.1)$$

where  $q$  contains all down-type quarks  $d$ ,  $s$  and  $b$ . The branching ratio  $\mathcal{B}$  is defined as  $\mathcal{B}_i = \Gamma_i/\Gamma$  and thus constitutes the fraction of particles which decay via a certain decay mode  $i$  with respect to the total number of decaying particles.  $\Gamma_i$  denotes the corresponding partial decay width. The ratio of branching fractions given above can consequently be written as a ratio of decay widths. Also direct measurements of this ratio have been performed leading to:  $\Gamma_{Wb}/\Gamma_{Wq} = 0.91 \pm 0.04$ , with  $q$  containing again  $d$ ,  $s$  and  $b$  [13] quarks. This result, which is close to the expectation mentioned in Eq. (2.1) and based on the assumption of CKM unitarity, stresses how rare the decay of top quarks into the lighter ones  $s$  and  $d$  in fact is.

The  $b$  quarks resulting from top quark decays hadronise to form jets. These  $b$  jets include  $B$  mesons, which may possess a decay vertex that is displaced from the initial interaction point, referred to as primary vertex. This is due to their comparatively long lifetime of about 1.5 ps that results in a flight length path of more than 1 mm. Such a displaced or secondary vertex enables a differentiation between  $b$  jets and jets originating from light quarks having only a primary vertex. The  $W$  boson, on the contrary, can decay into two light quarks  $q_1$  and  $\bar{q}_2$  which then hadronise to jets like the  $b$  quarks or, alternatively, the boson can decay into a charged lepton  $\ell$  and the corresponding antineutrino. These types of decay constitute a hadronic or, respectively, leptonic decay.  $\ell$  is used to describe leptons and can hence be an electron  $e$ , a muon  $\mu$  or a tau lepton  $\tau$ . Estimated branching ratios  $\mathcal{B}$  of the different  $W$  decay channels are summarised in Table 2.5. A further colour factor  $N_C$  with  $N_C^{\text{lep}} = 1$  and  $N_C^{\text{had}} = 3$  needs to be considered for a proper estimate.

Final States	$e\nu_e$	$\mu\nu_\mu$	$\tau\nu_\tau$	$u\bar{d}/d\bar{u}$	$c\bar{s}/s\bar{c}$
$N_C$	1	1	1	3	3
$\mathcal{B}$	$\frac{1}{9}$	$\frac{1}{9}$	$\frac{1}{9}$	$\frac{1}{3}$	$\frac{1}{3}$

Table 2.5: Estimated branching ratios of the final states from different  $W$  boson decays. For the hadronic decays, the most probable final states according to the CKM matrix are listed. As the products of such a decay depend on the charge of the initial  $W$  boson, both possibilities of combinations are specified.

**Decay Channels of Top Quark Pairs** As both  $W$  bosons originating from a top quark pair decay independently, three different combinations of the two decay channels arise: *all-jets*, *dileptonic* or *lepton+jets*. The latter characterises a channel with one  $W$  boson decaying hadronically while the other decays into leptons.

Leptonic decays into tau leptons are disregarded in the following approach because final states containing this heaviest lepton are intricate to identify due to its decay into either quarks or lighter leptons. With the help of Table 2.5, the probabilities of leptonically and hadronically decaying  $W$  bosons yield  $P_{\text{had}} = 2/3$  and  $P_{\text{lep}} = 2/9$ . These numbers allow for an estimation of the branching fractions of the different decay channels of top quark pairs:

The *all-jets decay channel* is characterised by two  $W$  bosons both decaying into quarks. Then, the branching ratio for this decay is relatively large and amounts to  $\mathcal{B} = 2/3 \cdot 2/3 = 4/9$ . The resulting six jet signature including the two  $b$  jets resembles that of QCD multijet background complicating the separation of signal and background. But in contrast to the other two channels, this one benefits from not having any missing transverse energy from a neutrino which must be taken into consideration.

The *dileptonic decay channel* has a branching ratio of  $\mathcal{B} = 2/9 \cdot 2/9 = 4/81$  since both participating bosons decay leptonically into an electron or a muon. The signature comprises two oppositely charged leptons, two  $b$  jets and a large amount of missing transverse energy  $E_{\text{T}}^{\text{miss}}$  (see also Chapter 5.1) caused by two undetected neutrinos emerging from the  $W$  decays. The dileptonic final state possesses the cleanest signature with two leptons featuring high transverse momenta  $p_{\text{T}}$  but, at the same time, has the lowest branching ratio.

The *lepton+jets decay channel*, finally, is specified by one leptonically and one hadronically decaying  $W$  boson. Hence, the signature is composed of four jets, including the two bottom jets and two jets originating from lighter quarks, one isolated lepton  $\ell = e, \mu$  with high transverse momentum and missing transverse energy. Energy and momentum conservation allow for the reconstruction of the momentum of the involved neutrino causing missing transverse energy. The branching ratio amounts to  $\mathcal{B} = 2 \cdot 2/9 \cdot 2/3 = 8/27$  and thus outvalues the one of dileptonic events, but the channel suffers from more background.

To conclude, for the measurement of the  $W$  polarisation described in one of the upcoming chapters, only those lepton+jets decay events are taken into account as the underlying decay channel constitute a compromise between an adequate branching ratio and a small background [27, 46]. To be exact, merely events in the muon+jets channel are considered and selected. It should be added that the signal events also contain dileptonic  $t\bar{t}$  events and lepton+jets events with a tau lepton subsequently decaying leptonically.

**Decay Channels of Single Top Quarks** To analyse the  $Wt$  production, two  $W$  bosons need to be considered because of the top quark predominantly decaying into a  $W$  boson and a  $b$  quark. Thus the discussion of decay channels is comparable to the description of top quark pair decays. In order not to repeat it, solely the chosen decay channel is delineated: The associated  $Wt$  production is studied in the lepton+jets decay channel or, to be more precise, in the  $\mu$ +jets decay channel with one hadronically and one leptonically (with  $\ell = \mu$ ) decaying  $W$  boson. The analysis possesses also a certain acceptance to signal events with a  $W$  boson decaying into a  $\tau$  lepton while this lepton subsequently decays either according to  $\tau \rightarrow e\nu_e\nu_\tau$  or  $\tau \rightarrow \mu\nu_\mu\nu_\tau$ , similar to the chosen  $t\bar{t}$  decay channel. The experimental signature of single top quark events in this analysis can thus be described as follows: It comprises one isolated charged lepton  $\ell = \mu$ , missing transverse energy  $E_T^{\text{miss}}$  because of at least one neutrino and at least two jets with high transverse momentum  $p_T$ . The LO Feynman diagram represents the 3-jet signature where one jet is a  $b$  jet while the other two are light ones coming from the hadronically decaying  $W$  boson. This signature dominates over the 2- and 4-(inclusive)-jet signature that contribute to the signal although being more influenced by background. The contribution of the 2-jet signature can be explained by overlapping jets in the beam pipe or jets with a too small energy not fulfilling the selection criteria while the 4-(inclusive)-jet signature has to be taken into account due to fake lepton events (see below) or due to initial and final state radiation, which can be defined as the radiation of gluons or photons in the initial or final state of an event. Events with two (inclusively) tagged  $b$  jets are considered in the analysis as well because jets wrongly tagged as  $b$  may occur. This decay channel is chosen for reasons already mentioned in the last paragraph: It can be regarded as a compromise between a high branching ratio and a comparatively small background. All events with 2 (excl.), 3 (excl.) or 4 (incl.) jets in the final state, as they are considered in the analysis, - corresponding to the 2-(excl.)-, 3-(excl.)- and 4-(incl.)-jet signature - are denoted as 2-, 3- and 4-jet bin.

**Relevant Background Contributions** One relevant background contribution for both analyses presented in this thesis is  $W$ +jets production caused by the misidentification of a light jet tagged as a  $b$  jet or by one jet being a heavy flavour jet. In Fig. 2.5, two Feynman diagrams for the  $W$ +jet production with one jet in the final state are exemplarily shown. QCD multijet production is another noteworthy background which arises either due to a high- $p_T$ , isolated lepton within a jet emerging from the lepton+jets decay of a heavy flavour hadron or due to a hadronic jet misidentified as a lepton, which is why it is also called fake lepton background. Single top events constitute a relevant background for the  $W$  polarisation measurement while  $t\bar{t}$  production is a noteworthy background source for the measurement of the  $Wt$  production cross-section.

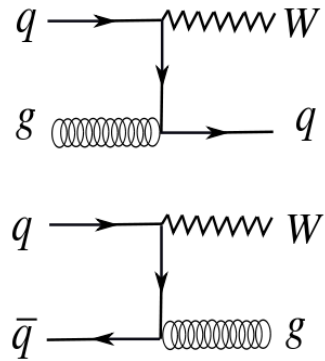


Figure 2.5:  $W$ +1 jet production: Compton process (top) and  $q\bar{q}$  annihilation (bottom).

### 2.2.3 Top Quark Properties

One of the most remarkable properties of the top quark is its mass that was measured to [13]:

$$m_t = 173.5 \pm 0.6 \text{ (stat.)} \pm 0.8 \text{ (syst.) GeV}/c^2,$$

and is thus much larger than the one of the bottom quark, the weak isospin partner of the top quark. A further comparison between the total uncertainty and  $m_t$  as the current world average shows a high relative precision of the top mass measurement exceeding the precision of the other measured quark masses:  $\sigma_{\text{rel}} = \sigma_{\text{tot}}/m_t \approx 0.58\%$ . The top quark is presumed to carry charge  $Q = +2/3 \cdot e$  and to have spin  $s = 1/2$ . A current measurement of the top quark charge using the ATLAS detector can be found in [47]. Another important study in the field of top quark physics is the measurement of the spin correlation between top and antitop quarks. This correlation has been observed with the ATLAS detector recently [48].

Because of its large mass, top quarks have a very short lifetime of about  $\tau_t = 1/\Gamma_t \approx 5 \cdot 10^{-25}$  s [49].  $\Gamma_t$ , related to the lifetime  $\tau_t$ , is the total decay width of the top quark. Due to a time of  $\tau_{\text{had}} \approx 3 \cdot 10^{-24}$  s required to form bound state hadrons, the top quark decays before hadronisation might take place. As a consequence thereof, bound states containing top quarks cannot exist. This allows for an experimental test of the properties of the bare top quark through its decay products. A hadronisation process would be responsible for losing information about the underlying decay.

The total width  $\Gamma = \hbar/\tau$  is proportional to  $|V_{tb}|^2$  with the CKM matrix element  $V_{tb}$  and features a dependence on  $m_W/m_t$  with the  $W$  boson mass  $m_W$  pursuant to Fermi's Golden Rule and [49] with the Fermi coupling constant  $G_F$ :

$$\Gamma(t \rightarrow Wb) = \frac{G_F}{8\pi\sqrt{2}} \cdot m_t^3 |V_{tb}|^2 \left( 1 - 3 \left( \frac{m_W}{m_t} \right)^4 + 2 \left( \frac{m_W}{m_t} \right)^6 \right).$$

With the Born approximation, the decay width can be determined to about:  $\Gamma_t^B \approx 1.44$  GeV. Taking furthermore the QCD coupling  $\alpha_s$  into account, which is related to  $g_s$  and which depends on  $m_t$ , the total decay width can be estimated by using  $m_t = 171 \frac{\text{GeV}}{c^2}$  according to [50, 51]:

$$\Gamma(t \rightarrow Wb) = \Gamma_t^B \cdot (1 - 0.81\alpha_s - 1.81\alpha_s^2) \approx 1.28 \text{ GeV}.$$

A very recent measurement of  $\Gamma_t$  was performed with the  $D\bar{O}$  experiment at the Tevatron collider at  $\sqrt{s} = 1.96$  TeV and yielded:  $\Gamma_t = 2.00_{-0.43}^{+0.47}$  [52].

The CKM matrix element  $V_{tb}$  is one of the less accurately known quantities in the field of top quark physics.  $V_{tb}$  determines the coupling strength at the  $Wtb$  vertex, specified in more detail below, in combination with the universal electroweak coupling constant. Using a measurement of the single top quark production cross-section enables a calculation of the absolute value of  $V_{tb}$  because this cross-section scales with  $|V_{tb}|^2$ .

By applying unitarity constraints, CKM matrix elements except for  $V_{tb}$  can be used to indirectly evaluate  $|V_{tb}|$  with comparatively large precision which results in  $|V_{tb}|$ -

values close to one. The current value is  $0.999146^{+0.000021}_{-0.000046}$  [13], based on the assumption of CKM unitarity. If such an assumption does not hold,  $|V_{tb}|$  can solely be derived by using a measurement of single top quark production, which stresses the relevance of such a study.

### 2.2.4 W Boson Polarisation

One of the interesting features of top quark decays is the helicity of the  $W$  bosons since the  $W$  boson polarisation allows to test the  $Wtb$ -vertex Lorentz structure and to look for physics beyond the SM. The helicity is formally defined as the projection of the spin onto the direction of momentum.

As mentioned earlier, the top quark as a fermion carries spin  $s = 1/2$ , like the bottom quark, while the  $W$  boson is a particle having spin  $s = 1$ . The  $W$  boson and the  $b$  quark need to have opposite momenta in the rest frame of the top quark. If also conservation of the angular momentum is considered, three different possibilities for the spins in the rest frame of the top quark can be distinguished. These are visualised in Fig. 2.6 and referred to as the three possible helicity states, correspondent to three different polarisation states: The illustration displays that the polarisation of the  $W$  bosons can be longitudinal, left-handed or right-handed. The thin arrows specify the flight direction of both the  $W$  boson and the  $b$  quark, the broader ones indicate the spin direction.

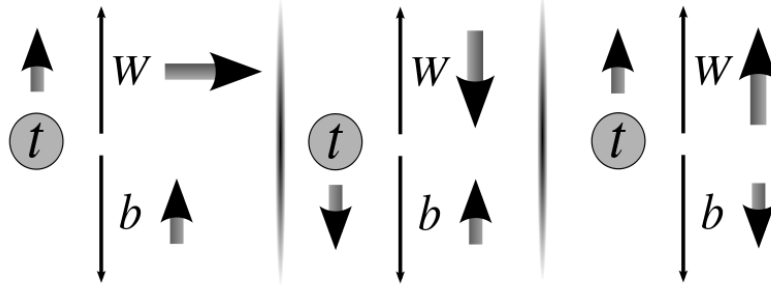


Figure 2.6: Possible helicity states in the decay of the top quark. The polarisation of the  $W$  boson can either be longitudinal (left), left-handed (middle) or right-handed (right).

The  $Wtb$  vertex has a V-A (“vector minus axial vector”) structure so that the SM Lagrangian of this vertex can be written as:

$$\mathcal{L} = -\frac{g}{\sqrt{2}} \bar{b} \gamma^\mu V_{tb} \frac{1}{2} (1 - \gamma^5) t W_\mu^- + h.c.$$

The V-A structure manifests in the term  $1/2 \cdot \gamma^\mu (1 - \gamma^5)$ . The  $Wtb$  vertex has a large impact on the probability with which the different helicity states may occur: Due to the V-A structure, the production of right-handed  $W$  bosons is heavily suppressed. In the limit of a massless bottom quark, the helicity fraction for right-handed  $W$  bosons is even zero. The three helicity fractions are usually denoted as  $F_L$

for the left-handed,  $F_R$  for the right-handed and  $F_0$  for the longitudinally polarised  $W$  bosons. They can be defined via the corresponding decay widths as:

$$F_0 = \frac{\Gamma(t \rightarrow W_0 b)}{\Gamma(t \rightarrow W b)}, \quad F_L = \frac{\Gamma(t \rightarrow W_L b)}{\Gamma(t \rightarrow W b)}, \quad F_R = \frac{\Gamma(t \rightarrow W_R b)}{\Gamma(t \rightarrow W b)}.$$

The indices  $L$ ,  $R$  and  $0$  directly refer to left-handed, right-handed or longitudinally polarised  $W$  bosons. Correspondingly, the partial decay widths are often written as  $\Gamma_0$ ,  $\Gamma_L$  and  $\Gamma_R$  with  $\Gamma(t \rightarrow W b) = \Gamma_0 + \Gamma_L + \Gamma_R$ . These helicity fractions can be extracted from measurements of the angular distribution of the particles originating from the top quark decay. The angle  $\theta^*$  is defined as the angle between the momentum direction of the charged lepton from the  $W$  boson decay and the reversed momentum direction of the  $b$  quark which directly originates from the top quark decay, both boosted into the rest frame of the  $W$  boson. The angular distribution depends on the helicity fractions  $F_0$ ,  $F_L$  and  $F_R$  and yields:

$$\frac{1}{\sigma} \frac{d\sigma}{d \cos \theta^*} = \frac{3}{4} \sin^2 \theta^* F_0 + \frac{3}{8} (1 - \cos \theta^*)^2 F_L + \frac{3}{8} (1 + \cos \theta^*)^2 F_R.$$

At tree level, the following expressions hold for the three helicity states:

$$F_0 = \frac{(1 - y^2)^2 - x^2(1 + y^2)}{(1 - y^2)^2 + x^2(1 - 2x^2 + y^2)},$$

$$F_L = \frac{x^2(1 - x^2 + y^2 + \sqrt{\lambda})}{(1 - y^2)^2 + x^2(1 - 2x^2 + y^2)},$$

$$F_R = \frac{x^2(1 - x^2 + y^2 - \sqrt{\lambda})}{(1 - y^2)^2 + x^2(1 - 2x^2 + y^2)},$$

where  $x = m_W/m_t$ ,  $y = m_b/m_t$  and  $\lambda = 1 + x^4 + y^4 - 2x^2y^2 - 2x^2 - 2y^2$ . These fractions are predicted with the help of NNLO QCD calculations to be about [53]:

$$F_0 = 0.687 \pm 0.005$$

$$F_L = 0.311 \pm 0.005$$

$$F_R = 0.0017 \pm 0.0001.$$

Deviations from these expected values could be a hint for BSM physics. In the analysis presented here, the distributions of  $\cos \theta^*$  are exploited to determine the helicity fractions since these distributions are different for all these three possible polarisation states.

Recent ATLAS measurements using the lepton+jets and the dilepton channel of top quark pair events yielded the following values for the three helicity fractions:  $F_0 = 0.67 \pm 0.07$ ,  $F_L = 0.32 \pm 0.04$  and  $F_R = 0.01 \pm 0.05$  [54]. CMS measured the three helicity fractions in the lepton+jets channel to:  $F_0 = 0.57 \pm 0.09$ ,  $F_L = 0.39 \pm 0.06$  and  $F_R = 0.04 \pm 0.06$  [55]. These measurements have been performed at  $\sqrt{s} = 7$  TeV.

## *2 The Standard Model and the Role of the Top Quark Therein*

## 3 The ATLAS Experiment

This thesis has been performed within the ATLAS Collaboration. ATLAS is a multipurpose detector which is located at the Large Hadron Collider at CERN<sup>1</sup> in Geneva. This chapter introduces the LHC, which began operating at the end of 2009, and covers a more detailed description of the ATLAS detector. Apart from that, several detector observables, which are important for the analyses presented in the subsequent chapters, are defined.

### 3.1 The Large Hadron Collider

The Large Hadron Collider (LHC) [56–58] is a collider which serves to accelerate protons as well as heavy ions and which is currently the most powerful particle accelerator worldwide. In this thesis, it is focused on proton-proton ( $pp$ ) collisions and, correspondingly, the discussion of the experimental setup of the LHC is based on the acceleration and collision of protons. The LHC was built in the tunnel of the former Large Electron Positron Collider (LEP) [59] lying approximately 150 m under ground. The accelerator has a circumference of 27 km. Since the analyses presented in this thesis use data which was collected by the ATLAS detector [60–62] in 2011 when the LHC served to collide protons at a centre-of-mass energy of  $\sqrt{s} = 7$  TeV, the following description of the LHC is based on this centre-of-mass energy. Since 2012, the LHC is operating at a centre-of-mass energy of  $\sqrt{s} = 8$  TeV. In 2011, the ATLAS detector collected  $pp$  collision data which corresponds to an integrated luminosity of about  $5.25 \text{ pb}^{-1}$  [63] while the instantaneous luminosity was about  $10^{32} \text{ cm}^{-2}\text{s}^{-1}$ . After a further shutdown period, the LHC is expected to reach  $\sqrt{s} = 14$  TeV at a design luminosity of  $10^{34} \text{ cm}^{-2}\text{s}^{-1}$ .

The resulting particle collisions are recorded by the four main detector experiments: ATLAS and CMS [64] as the so-called multipurpose detectors, LHCb [65], an asymmetric detector concentrating on  $B$ -physics, and ALICE [66] which is used to analyse the quark-gluon plasma in heavy ion collisions to study conditions comparable to those shortly after the Big Bang.

**Design** This paragraph presents the design of the LHC more thoroughly. All proton beams which enter the collider need to be preaccelerated in a chain of older, already existing and smaller ring or linear accelerators placed at CERN that were upgraded in the last years to fulfil all LHC requirements. A sketch of the LHC and its preaccelerators including the four main experiments can be found in Fig. 3.1.

---

<sup>1</sup>European Organisation for Nuclear Research, name originating from: Conseil Européen pour la Recherche Nucléaire.

### 3 The ATLAS Experiment

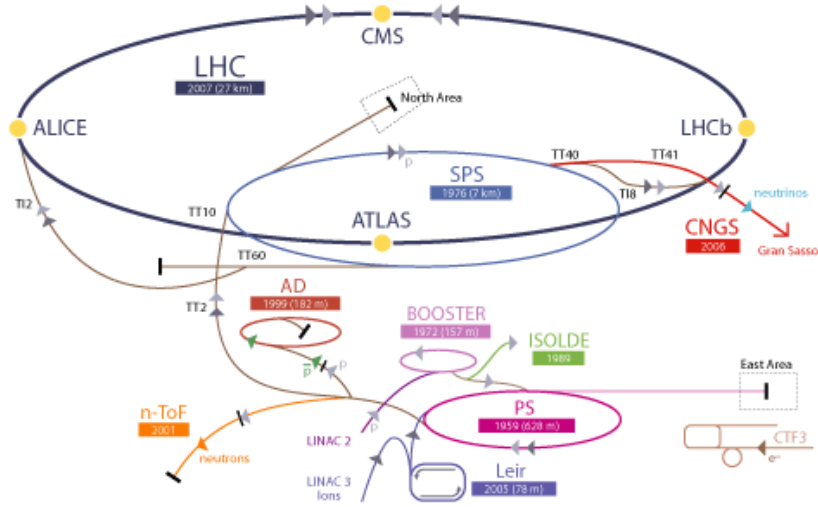


Figure 3.1: The LHC and the corresponding accelerator chain as well as the four main experiments at the interaction points in the framework of the entire CERN accelerator complex [67].

The protons which originate from the ionisation of hydrogen atoms are first accelerated to 50 MeV in a linear collider called LINAC2 and then transferred to the Proton Synchrotron Booster to reach an energy of 1.4 GeV. In the Proton Synchrotron (PS) as the oldest accelerator of the complex built more than 50 years ago, the protons gain an energy of 25 GeV after leaving the booster. The Super Proton Synchrotron (SPS) with a circumference of 7 km accelerates the protons in a next step to the injection energy of the LHC which amounts to 450 GeV. From the SPS, bunches of protons enter the separate beam pipes in both opposite directions around the LHC ring and are then accelerated simultaneously with the help of radio frequency cavities situated inside the beam pipe and providing an ultrahigh vacuum of  $10^{-10}$  mbar. After the protons reach their final energy of 3.5 TeV (equivalent to  $\sqrt{s} = 7$  TeV) in 2010 and 2011 and to 4 TeV in 2012, they collide at four different interaction points. The points where the beam pipes cross are directly at the centre of the four main detectors mentioned above.

The protons are accelerated in bunches which consist of about  $10^{11}$  particles each. Up to 2,808 bunches and a bunch crossing which is expected every 25 ns result in a design luminosity of  $10^{34}$   $\text{cm}^{-2}\text{s}^{-1}$ . This is, depending on how the beam is focused, equivalent to at least 20 inelastic collisions per bunch crossing on average. In 2011, the bunch spacing amounted mainly to 50 ns.

In total, 1,232 superconducting dipole magnets with a magnetic field of maximally up to 8.6 T keep the beams on their circular path while 392 quadrupole magnets are responsible for correcting the position of the beams and for focusing them. Both the acceleration cavities and the guidance magnets of the LHC use superconducting technologies. The dipole magnets are cooled down to reach temperatures of about 1.9 K. The use of superfluid helium allows for such high central field strengths.

### 3.2 Detector Observables and Coordinates

In this section, several frequently used detector variables and observables related to detector experiments are specified as they are used in the following analyses and on the following pages which introduce the ATLAS detector and all its different components more in-depth.

Apart from the instantaneous luminosity, the integrated luminosity  $\int \mathcal{L} dt$  constitutes a commonly used variable. It is usually measured in inverse barns  $\text{b}^{-1}$  (picobarns and femtobarns are realistic scales) with  $1\text{b} = 10^{-28} \text{m}^2$ . It complies with the number of collisions occurring within a particular time interval and can be rendered into a number of events for a specific physics process which are collected with a detector like ATLAS if the cross-section  $\sigma$  of this process is known. The corresponding relation is:  $N = \sigma \int \mathcal{L} dt$ .

To characterise positions inside the detector, *cylindrical coordinates*  $(r, \theta, \phi)$  are commonly used.  $r$  denotes the radial distance from the beam axis and  $\phi$  the azimuthal angle, which defines the direction vertical to the beam axis. The third coordinate  $\theta$  represents the polar angle which is the angle between the particle's flight direction and the beam axis. But instead of this angle  $\theta$ , the *pseudorapidity*  $\eta$  is normally applied as the third coordinate. With its dependence on  $\theta$ , it is defined according to:

$$\eta = -\ln \tan \frac{\theta}{2}.$$

Differences measured in  $\eta$  are invariant under Lorentz boosts. The differential cross-section as a function of the pseudorapidity is rather flat in the detector region close to the beam axis which constitutes another advantage of using  $\eta$  since this area comprises a comparatively high particle density. Distances  $\Delta R$  are specified in the  $\eta$ - $\phi$ -plane pursuant to:

$$\Delta R = \sqrt{\Delta\phi^2 + \Delta\eta^2}.$$

Instead of the initially defined system, also the coordinate system  $(\phi, \eta, z)$  can be used where the  $z$ -axis with the third coordinate  $z$  is equivalent to the beam axis. Momenta and energies of particles are often given as transverse momenta  $p_{\text{T}}$  and transverse energies  $E_{\text{T}}$  which can be written as:

$$p_{\text{T}} = \sqrt{p_x^2 + p_y^2} = |p| \sin \theta \quad \text{and as} \quad E_{\text{T}} = E \sin \theta.$$

In this context,  $x$  and  $y$  are Cartesian coordinates which span the transverse plane as the plane perpendicular to the beam axis.

### 3.3 The ATLAS Detector

ATLAS (A Toroidal LHC ApparatuS) as one of the two multipurpose detectors located at the LHC is constituted of different subdetectors. The four main parts are an inner detector, a calorimeter system, a muon spectrometer and a magnet system, composed of a solenoid and a toroidal system, which are described more precisely in the subsequent paragraphs. In Fig. 3.2, an overview of the entire detector and its subsystems is displayed. The detector weighs approximately 7,000 t in total, is about 44 m long and measures 25 m in diameter.

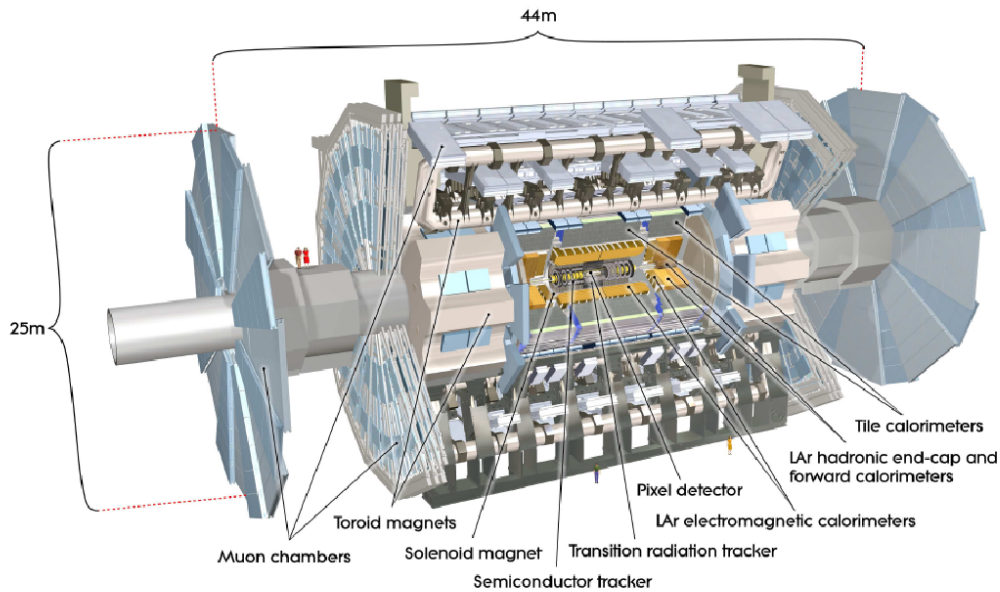


Figure 3.2: Sketch of the ATLAS detector and its subsystems [60].

As a multipurpose detector, ATLAS is engineered to allow for a measurement of a large variety of different physics processes. That is why the detector covers the overall  $4\pi$  solid angle and measures a broad range of particle momenta. Several other requirements have to be fulfilled as well in order to obtain a considerable accuracy in all subdetectors to collect collision data to the highest possible extent. For instance, multiple interactions which occur due to the high beam intensities have to be distinguished from each other to fully reconstruct the corresponding events. Particles originating from the primary vertex or interaction point can be detected by the successive layers of ATLAS while traversing the detector. Charged particles are directly measured in the innermost detector layers with the help of tracking chambers located there. Due to the magnetic field caused by the superconducting solenoid, the particle trajectory is bent in the inner part of the detector, which can be exploited to obtain the momentum and the sign of charge of the associated particle. The electromagnetic and hadronic calorimeters placed around the solenoid magnet serve to measure the energy of the traversing particles. The particles lose

energy because of interactions with the detector material and are stopped in the calorimeters. The calorimeter cells are used to calculate the deposited energy. The muon spectrometer as the outermost layer of ATLAS detects muons which leave the calorimeters - as they constitute minimum ionising particles pursuant to the Bethe-Bloch formula [13] -, enables a measurement of the muon momentum and triggers on these leptons. Such measurements exploit the bending of the tracks caused by the toroidal magnetic field.

### 3.3.1 Inner Detector

The *Inner Detector* (ID) of the ATLAS experiment beginning a few centimetres from the beam axis consists of three subdetector systems: the *Pixel Detector*, the *Semiconductor Tracker* (SCT) and the *Transition Radiation Tracker* (TRT). Both the Pixel Detector and the SCT are based on a silicon semiconductor technology while the TRT contains a gas composed of xenon, carbon dioxide and oxygen in which transition radiation is induced. In Fig. 3.3, a longitudinal as well as a transverse section of the ID are displayed, showing the dimensions of the various subdetector layers. In total, the cylindrical volume of the ID has a length of 6.2 m and a radius of about 1.1 m. The design of the Inner Detector allows for a measurement of particle momenta in a pseudorapidity range of  $|\eta| < 2.5$ . It provides a momentum resolution of  $\sigma_{p_T}/p_T^2 = \sqrt{(0.05\%)^2 + (1\%)^2}$ .

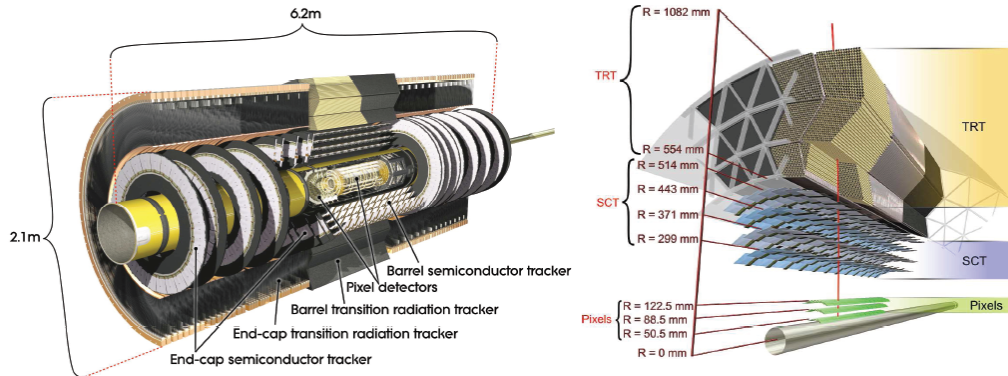


Figure 3.3: The Inner Detector of the ATLAS experiment: The left picture presents a sketch of the Inner Detector with the different subdetectors. The figure on the right displays a transverse section of the ID. It contains the distances of the detector layers with respect to the beam line [60].

The Pixel Detector is composed of three layers as concentric cylinders in the barrel part and three endcap disks on each side which are vertical to the beam axis. This subdetector starts 5 cm away from the interaction point and is thus the detector part which is built closest to the beam pipe. 1,744 modules are distributed over these layers and disks that are composed of more than 80 million readout channels. Each of this readout channels is equivalent to an  $n^+$ -on- $n$ -doped silicon pixel which

### 3 The ATLAS Experiment

operates as a sensor. These pixels with a thickness of 250  $\mu\text{m}$  cover an area of at least  $50 \times 400 \mu\text{m}^2$ . The structure allows for a high precision measurement of tracks and the identification of primary and secondary vertices helping to detect, for example, tau leptons or jets coming from heavy flavour quarks. This identification of  $b$  jets, the so-called  $b$ -tagging, is explained in the analysis chapters in more detail.

Comparable in concept and function is the SCT which consists of long silicon strips instead of small pixels hence comprising a larger area. The strip pitch amounts to 80  $\mu\text{m}$ . The strips are included in 4,088 modules resulting in 6.3 million readout channels in the SCT, arranged parallel to the beam axis in four layers of the barrel region and radially oriented in nine endcap disks.

The detecting elements of the TRT are about 350,000 drift tubes, so-called straws, filled with the gas mixture mentioned above and having a radius of 2 mm each. The barrel part is composed of 73 planes of these straw tubes parallel to the beam axis, while in the endcap part even 160 straw planes with a radial orientation are present. Apart from measuring particle tracks via ionisation, the TRT exploits transition radiation to detect particles, which can be explained as follows: Relativistic charged particles emit photons when they cross - while travelling through the detector - the interface of two media having different dielectric constants  $\epsilon_r$ . Depending on the rate of emitted photons, different kinds of particles can be discriminated. Electrons due to their low mass cause considerable transition radiation whereas heavier particles produce only fewer photons. Pions constitute an example of such heavier particles. Silicon trackers provide a better spatial resolution than the TRT, but due to the filling gas of the TRT, the drift time of, e.g., electrons is significantly reduced leading to a smaller impact from neighbouring bunch crossings.

#### 3.3.2 Calorimeter System

Two calorimeter systems surrounding the Inner Detector are employed by the ATLAS experiment covering a large  $|\eta|$ -range with  $|\eta| < 4.9$ : an inner *electromagnetic calorimeter system* and an outer *hadronic calorimeter system*. Both are so-called *sampling calorimeters* that are characterised by alternating layers of passive and dense absorber material and active material, connected to a read-out system. The calorimeter system with its compact size absorbs the energy of particles in the detector which enables a measurement of the energy deposit of these particles. In most ATLAS calorimeters, liquid argon (LAr) functions as the active medium used to measure the particle energies. The calorimeter system is able to quantify the energy of different kinds of charged and neutral particles as well as of jets. It covers a broad energy range beginning with several GeV up to the TeV scale and allows for a determination of the energy mismatch of a particle reaction which is equal to missing transverse energy  $E_{\text{T}}^{\text{miss}}$ . A sketch of the calorimeter system partitioned into various cells is presented in Fig. 3.4.

The EM calorimeter possesses a fine granularity which is concomitant with a high resolution necessary for measurements of the electron or photon energy. The hadronic calorimeter, on the contrary, allows for an appropriate measurement of jets and  $E_{\text{T}}^{\text{miss}}$

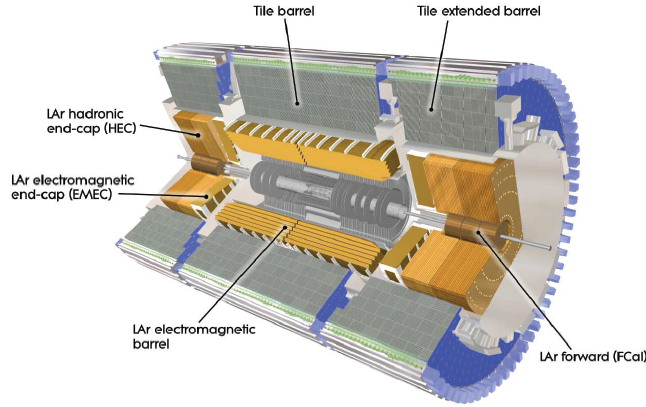


Figure 3.4: The calorimeter system of the ATLAS experiment: The different components of the electromagnetic and the hadronic calorimeters are displayed [60].

with its coarser constituents. A proper specification of  $E_T^{\text{miss}}$  requires the large  $|\eta|$ -coverage of the forward hadronic calorimeter of  $|\eta| < 4.9$ , given above, so that all particles of one event can be detected.

The thickness of the calorimeter components in the barrel part of the system is consistent with at least 22 radiation lengths, denoted as  $X_0$ , and amounts to at least 24 radiation lengths in the endcap region. In this context, the radiation length is a measure of the distance over which a particle loses its energy except for the fraction  $1/e$ . These numbers depend in particular on the pseudorapidity region and can increase to up to 38  $X_0$ . Leaving the entire calorimeter, a particle has usually passed a sufficient number of radiation lengths, large enough for an adequate suppression of punch-through effects to the muon spectrometer.

The electromagnetic (LAr EM) calorimeter is based on an accordion geometry to ensure a uniform and especially fast response. According to its abbreviation, the EM calorimeter uses liquid argon as the active medium over which Kapton electrodes are spread. Lead plates function as the passive absorber material. Both active and passive calorimeter parts cover a range of  $|\eta| < 3.2$ . Each of the three different parts, in which the EM calorimeter is divided, is placed in an own individual cryostat. The calorimeter has a fine cell granularity, e.g. in  $\eta$  of about  $\Delta\eta = 0.025$ , which, as explained above, is responsible for the adequate spatial resolution of this calorimeter. The energy resolution of a calorimeter is in general expressed by:  $\sigma_E/E = a/\sqrt{E} \oplus b$ , with a stochastic term  $a$  and a constant term  $b$ . The resolution of the ATLAS electromagnetic calorimeter is about [61]:

$$\frac{\sigma_E}{E} = \frac{10\%}{\sqrt{E}} \oplus 0.7\%.$$

In order to entirely contain hadronic particles and jets penetrating the EM calorimeter, hadron calorimeters are built outside of the latter. This sampling calorimeter is composed of plastic scintillating tiles - which is why it is also referred to as tile calorimeter - and iron absorbers in the central or barrel part with  $|\eta| < 1.7$  while the

### 3 The ATLAS Experiment

forward region covering a detector space up to  $|\eta| < 4.9$  is made up of a calorimeter which uses liquid argon as the active material. The energy resolution of this calorimeter in the barrel and endcap region amounts to [61]:

$$\frac{\sigma_E}{E} = \frac{50\%}{\sqrt{E}} \oplus 3\%.$$

#### 3.3.3 Muon System

The muon spectrometer as the outermost layer of ATLAS is composed of four different sorts of muon chambers. It serves to measure the momenta of muons which leave the calorimeter system and have energies exceeding 3 GeV in a pseudorapidity range of  $|\eta| < 2.7$ . The magnetic field of the air-core toroidal magnet system is responsible for bending the resulting muon tracks. The orientation of the fields in the barrel and the endcap region ensures that muon tracks are predominantly rectangular to the magnetic field lines.

The design of this system can be seen in Fig. 3.5. It contains both tracking chambers allowing for precision measurements and trigger systems. In the barrel region, *Monitored Drift Tubes* (MDT) are applied for tracking and *Resistive Plate Chambers* (RPC) serve to trigger events whereas *Cathode Strip Chambers* (CSC, apart from MDTs) operate as tracker and *Thin Gap Chambers* (TGC) as trigger in the endcap part of the muon system. The eight octants in which the muon system is split overlap in the azimuthal angle  $\phi$  to ensure a full coverage of the detector. In both parts of the system, muons usually cross three longitudinal layers of the spectrometer.

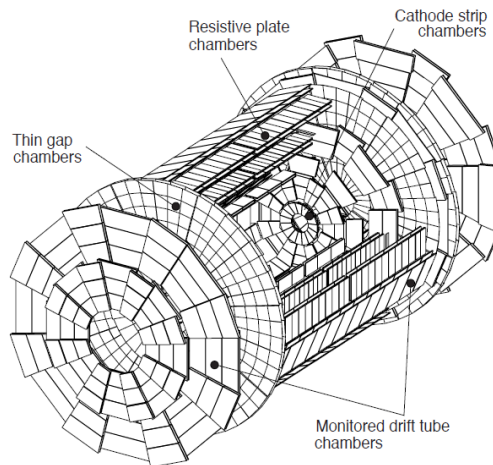


Figure 3.5: The muon system of the ATLAS experiment with its four different components [60].

The dimensions of the muon system demand a good acquaintance of the system with regard to the chamber position to avoid a performance loss concerning the reconstruction. The choice of the technologies used for tracking muons was dominated by the idea of obtaining high precision with respect to the existing particle flux.

The trigger chambers are required to be fast and efficient depending on the actual conditions in both the barrel and endcap parts of the muon spectrometer.

In the barrel region up to  $|\eta| < 2.0$ , MDT chambers are assembled in three layers of chambers and in most layers of the endcap region. On the contrary, CSCs are only installed in the innermost layer of the endcaps. The MDTs are made of aluminium with a tube diameter of 30 mm. Cathode Strip Chambers are installed in the endcap region on the innermost wheel close to the beam pipe ( $2.0 < |\eta| < 2.7$ ) due to a larger number of background events there. The chambers are multiwire proportional chambers segmented into strips having orthogonal directions. The MDT reach a resolution of 80  $\mu\text{m}$ , the resolution of one single CSC amounts to 40  $\mu\text{m}$  in the bending plane.

Resistive Plate Chambers serve to induce a very fast trigger signal. Each chamber is composed of two bakelite plates and a gas-filled gap in between. Thin Gap Chambers finally contain two cathode plates with an anode wire in between. The TGCs are characterised by a small drift time thus providing a rapid signal.

### 3.3.4 Magnet System

The ATLAS magnet system causes a bending of the charged particle trajectories traversing the detector which enables a measurement of the particle momenta. The ATLAS detector uses a solenoid magnet that is responsible for magnetic field for the Inner Detector while barrel and endcap toroidal systems of magnet coils are employed to produce a magnetic field in the area where the muon chambers are located. The magnet system is based on superconducting magnets which are cooled by liquid helium to reach a temperature of about 4.5 K. A sketch of the system is displayed in Fig. 3.6.

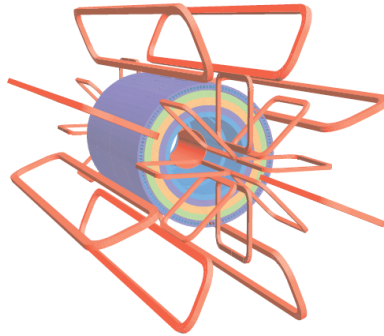


Figure 3.6: The magnet system of the ATLAS experiment including parts of the electromagnetic calorimeter [60].

The solenoid is placed between the Inner Detector and the calorimeters. Hence, it was engineered to have a low weight and to contain as little material as possible to minimise energy losses of particles passing the solenoid before they enter the calorimeter system. It causes an axial field with a strength of 2 T in the central region of the Inner Detector.

The toroidal magnetic field is induced by three independent air-core toroid systems used in the barrel and both endcap regions. Each system is composed of eight superconducting coils providing a magnetic field that amounts to about 3.9 T in the central part and increases to more than 4 T in the forward detector.

#### 3.3.5 Trigger System

Due to the fact that each bunch crossing causes enormously large amounts of data and since most detected events are assumed to be less appreciable QCD scattering events, a *three-level trigger system* is used to identify the most worthwhile signal events to retain for more extensive analyses while rejecting undesired background events. This is also essential because the large amount of data collected by the ATLAS detector cannot be stored for later exploration. To be more precise, the design luminosity of the LHC, which is, as stated above,  $10^{34} \text{ cm}^{-2}\text{s}^{-1}$ , provides a bunch collision rate of 40 MHz. The three-level trigger is needed to reduce the rate drastically to about 200 Hz.

The data acquisition system (DAQ) collects the data from all different subdetectors of the ATLAS experiment and retains it until the trigger decided about keeping or deleting the corresponding data. The first-level trigger is hardware-based and abbreviated as L1. In particular, it concentrates on finding photons, jets, electrons, muons or hadronically decaying tau leptons or a large total transverse energy as well as a high momentum mismatch in the transverse plane. The trigger needs less than 2.5  $\mu\text{s}$  to identify Regions-of-Interest (RoI) in the  $\eta$ - $\phi$ -space. The event rate is reduced to about 75 kHz with the L1 trigger.

The next two levels are denoted as L2 and Event Filter (EF) and constitute the high-level trigger. Both levels are software-based. The L2 trigger decreases the event rate to 3.5 kHz and serves to analyse the sort of trigger objects and to determine the energy and direction of the RoIs. Eventually, the EF provides an additional drop of the event rate approximately to the anticipated 200 Hz. Only events which pass all three trigger levels are permanently stored and finally reconstructed.

## 4 Profile Likelihood Analysis

This thesis presents two different measurements in the field of top quark physics which are both based on profile likelihood fits. The main concept of a profile likelihood analysis is introduced in this chapter. More information about the individual measurements as well as the analysis-specific implementation of profile likelihood fits is given in the subsequent chapters in which the different studies and the obtained results are described in more detail.

### 4.1 Why Profile Likelihood Fits?

Due to various systematic uncertainties which have to be taken into account, data analyses including measurements of top quark properties are known to be complex. For instance, the uncertainty on the jet energy scale, the amount of initial and final state radiation or the estimate of background contributions need to be considered.

Profile likelihood fits constitute an opportunity to significantly reduce the associated uncertainties by constraining them in the corresponding measurement. In this context, the different systematic variations enter the minimisation process of the likelihood itself as further fit parameters, which is a very remarkable attribute of profile likelihood fits. The additional fit parameters are referred to as nuisance parameters  $k_j$  with  $1 \leq j \leq N_{\text{prof}}$  - while  $N_{\text{prof}}$  specifies the number of systematic uncertainties that are used in the profile likelihood fit - so that for each considered systematic effect such a parameter is added. The size of the corresponding systematic uncertainty is directly adjusted by these parameters since the fitted values gathered from the fit constitute the quantity which best fits the data [68]. It is worth mentioning that not all systematic uncertainties can be profiled, i.e. can enter the fit as nuisance parameters. This is explained in Chapter 5 and Chapter 6.

As the integrated luminosity of both measurements addressed in this thesis amounts to at least  $\int \mathcal{L} = 2 \text{ fb}^{-1}$ , enough statistics is available to properly investigate to which extent the size of the systematics is consistent with the data and to properly rescale the systematic uncertainties accordingly. The uncertainty on the fit results of all nuisance parameters can be interpreted as follows: The corresponding value is used to define a 68% confidence level range in which all systematic variations are compatible with the underlying data.

## 4.2 Mathematical Aspects of a Profile Likelihood Fit

A profile likelihood can be defined as a likelihood which is maximised with respect to certain nuisance parameters.

To express it mathematically<sup>1</sup>, let  $\theta$  be a vector parameter which can be subdivided into two other vectors, a vector parameter of interest, denoted as  $\alpha$  and a nuisance vector parameter  $k$ .  $\theta$  can then be written as  $\theta = (\alpha, k)$ . The *likelihood function* is consequently of the following form:

$$\mathcal{L}(\theta|x) = \mathcal{L}(\alpha, k|x),$$

with a vector  $x$  that contains  $n$  independent observations. A likelihood function for a parameter with only few dimensions can easily be visualised by a graph. This graph represents a reversed parabola, as long as the corresponding likelihood is comparatively smooth. The maximum of this parabola is equivalent to a maximum likelihood estimator (MLE). For higher-dimensional parameters, however, the likelihood function cannot be employed in such a way. To surmount this problem, a *profile likelihood* can be used with a low-dimensional parameter of interest  $\alpha$  and a higher-dimensional nuisance parameter  $k$ . The profile likelihood is defined as:

$$L(\alpha|x) = \sup_k \mathcal{L}(\alpha, k|x),$$

with the supremum of the original likelihood [69]. This notation reflects that the profile likelihood is maximised with respect to  $k$ . Consequently, the nuisance parameters  $k$  can be expressed as  $f(\alpha)$  which means as a function of the parameter of interest  $\alpha$  and thus be replaced, leading to the following equivalent notation of the profile likelihood:  $L(\alpha, f(\alpha)|x)$ . Hence, the number of independent parameters is significantly reduced.

In the analyses presented above, the negative logarithmic likelihood is computed and minimised which is equivalent to maximising a likelihood. In Fig. 4.1, the foregoing explanations are presented graphically for such a minimisation of the profile likelihood. The above contour plot represents exemplarily a two-dimensional problem with the parameter of interest  $\alpha$  shown on the abscissa. The contour lines which are shaded from white to black conform with higher and lower values of the negative logarithmic likelihood. Likelihood-based confidence regions are marked by the thicker lines, the dashed one shows the behaviour of the negative logarithmic profile likelihood for the parameter of interest  $\alpha$  with regard to the parameter values. The asterisk in the middle indicates the position of the optimal choice of the parameters. The plot at the bottom displays the negative logarithmic profile likelihood as a function of  $\alpha$ . This emphasises how the desired minimum can be found with a profile likelihood fit and visualises the concept of such fits as used for the studies presented in this thesis.

---

<sup>1</sup>For reasons of clarity, no vector arrows are used in this paragraph.

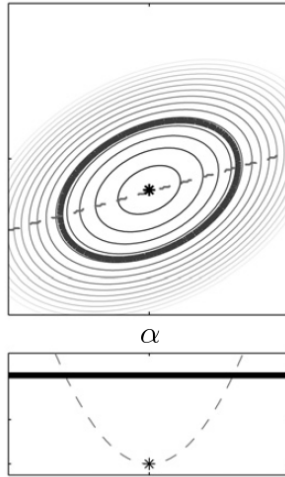


Figure 4.1: Contour plot visualising a two-dimensional problem (top) and the corresponding profile likelihood with its parabola shape as a function of the parameter of interest which is shown on the abscissa (bottom). More explanations are given in the text. The thick lines are used to mark certain confidence regions [70].

### 4.3 Profile Likelihood Analyses with Template Fits

The profile likelihood fits presented in this thesis are based on template fits. These rest on the idea of adding separate templates obtained from Monte Carlo simulation and auxiliary measurements of all signal and background contributions. With the help of fit parameters, the sum of these contributions is fitted to data in order to gain the number of corresponding signal and background events. In the following, these templates are denoted as nominal templates  $H$ .

Concerning the profile likelihood fit, further templates or distributions for the different systematic uncertainties are added to the minimisation process. All nuisance, or profiling, parameters  $\vec{k}$  which are added to the fit are presumed to possess Gaussian-shaped uncertainties around a nominal value of zero. A nuisance parameter value of  $\pm 1$  corresponds to a  $\pm 1\sigma$ -variation of the related systematic uncertainty. For each variation of  $+1\sigma$  and  $-1\sigma$ , also referred to as up- and down-variation, such an additional template is used.

The essential step during the minimisation process is an interpolation between the distributions that include the  $\pm 1\sigma$ -variations and the nominal distribution. This interpolation is also called *morphing* as the shape of the templates is *morphed* from  $H(-1\sigma)$  to  $H(\text{nominal})$  to  $H(+1\sigma)$ , and it is controlled by the underlying profiling parameters. This interpolation, or morphing, step is performed for all nuisance parameters, each of them representing one systematic uncertainty, and converts or morphs the three templates of the shape of one certain systematic effect into a sustained evaluation of the related uncertainty for all bins with nuisance parameters that express this estimation mathematically. This step is carried out for all available signal and background contributions and explained in Subsection 4.4.

The output of the morphing step are distributions or histograms for the different

#### 4 Profile Likelihood Analysis

signal and the background contributions. These are added as stated above and can be written as a combined distribution  $H_{\text{sum}}$  which depends on all the nuisance parameters  $\vec{k}$  and additional necessary normalisation parameters and which is then fitted to the data distribution  $H_{\text{data}}$ . Several fitting procedures are considered in the framework of this thesis, described in Chapter 5 and Chapter 6, respectively.

Fig. 4.2 exemplarily shows the three different templates  $H(-1\sigma)$ ,  $H(\text{nominal})$  and  $H(+1\sigma)$  to visualise the concept of morphing between such different templates. The distributions correspond to one certain systematic uncertainty, the jet energy scale (JES, see Section 5.1.4). These are used in the measurement of the  $W$  boson helicity fractions, as explained thoroughly in Chapter 6. They contain the signal events related to the helicity fraction  $F_0$  and depict how far the three templates may differ from each other. To which extent the bin entries vary between the templates is revealed by the ratio plots at the bottom of Fig. 4.2.

The estimation of the uncertainties on the fit parameters resulting from the profile likelihood fit is discussed in Chapter 5 and Chapter 6. In these analysis chapters, it is also outlined which systematic uncertainties can be profiled and how the different templates, including the  $\pm 1\sigma$  variations, can be obtained.

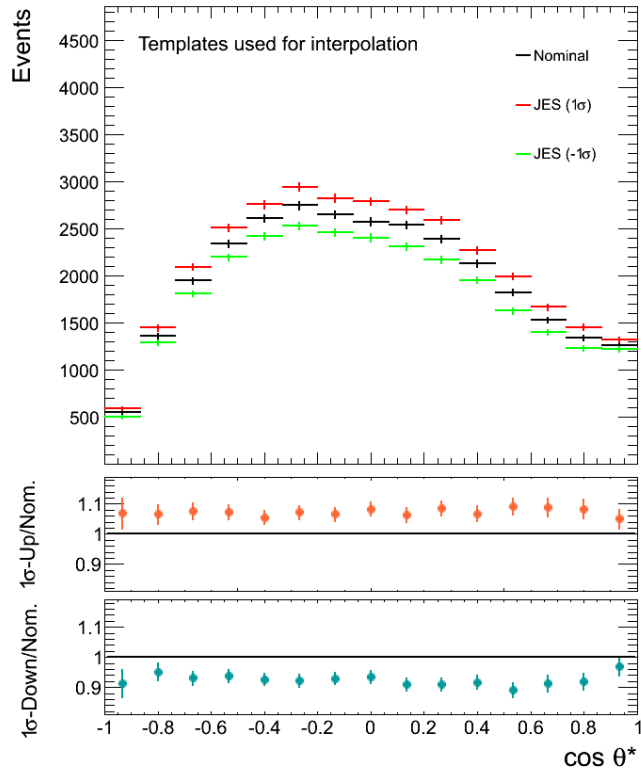


Figure 4.2: Three different templates  $H(-1\sigma)$ ,  $H(\text{nominal})$  and  $H(+1\sigma)$  are shown to exemplarily picture the idea of interpolating or morphing between those template distributions. This plot is explained in more detail in Chapter 6.3.2 where the corresponding analysis is described.

## 4.4 Interpolation Methods

To morph the templates from  $H(-1\sigma)$  to  $H(\text{nominal})$  to  $H(+1\sigma)$  (in the following abbreviated as  $H_{-1\sigma}$ ,  $H_{\text{nom}}$  and  $H_{+1\sigma}$ ) with the given nuisance parameters, a technique is used which is usually called *vertical template morphing* [71]. In the simplest case, the morphing or interpolation step is equivalent to a *linear interpolation*. Such a step needs to be done separately in each bin and for all systematic uncertainties represented by the nuisance parameters, which is reflected by the indices:  $j$  refers to the corresponding systematic uncertainty while  $i$  denotes a bin of the templates. The linear interpolation can then be written as:

$$H_{\text{int},ij} = H_{\text{nom},ij} + k_j \cdot \frac{H_{+1\sigma,ij} - H_{-1\sigma,ij}}{2}. \quad (4.1)$$

The difference between the up- and down-templates is thus handled as if it complies with a first-order Taylor expansion performed around  $H_{\text{nom}}$ . This approach is usually not most reliable since the above equation does not yield  $H_{\pm 1\sigma,ij}$  for  $k_j = \pm 1$ .

By using a *piecewise linear interpolation*, this can be solved so that a value of  $k_j = \pm 1$  yields  $H_{\pm 1\sigma,ij}$ . An important characteristic of this approach, in comparison to the former one, is its dependence on the sign of  $k_j$ . If  $k_j > 0$ , a linear interpolation between  $H_{+1\sigma}$  and  $H_{\text{nom}}$  is performed, if  $k_j < 0$ , it is performed between  $H_{\text{nom}}$  and  $H_{-1\sigma}$ :

$$H_{\text{int},ij} = H_{\text{nom},ij} + k_j \cdot \frac{H_{+1\sigma,ij} - H_{\text{nom},ij}}{2} \quad \text{if } k_j > 0 \quad (4.2)$$

$$H_{\text{int},ij} = H_{\text{nom},ij} + k_j \cdot \frac{H_{\text{nom},ij} - H_{-1\sigma,ij}}{2} \quad \text{if } k_j < 0. \quad (4.3)$$

An even more sophisticated interpolation is a quadratic one characterised by a quadratic interpolation for  $|k_j| < 1$  and a linear extrapolation beyond this range in such a way that the resulting interpolation function is continuous. This leads to:

$$H_{\text{int},ij} = H_{\text{nom},ij} + k_j \cdot \frac{H_{+1\sigma,ij} - H_{-1\sigma,ij}}{2} + k_j^2 \cdot \left( \frac{H_{+1\sigma,ij} + H_{-1\sigma,ij}}{2} - H_{\text{nom},ij} \right) \quad \text{if } |k_j| \leq 1, \quad (4.4)$$

$$H_{\text{int},ij} = H_{+1\sigma,ij} + (k_j - 1) \cdot \left( \frac{3}{2}H_{+1\sigma,ij} + \frac{1}{2}H_{-1\sigma,ij} - 2H_{\text{nom},ij} \right) \quad \text{if } k_j > 1, \quad (4.5)$$

$$H_{\text{int},ij} = H_{-1\sigma,ij} + (k_j + 1) \cdot \left( -\frac{3}{2}H_{-1\sigma,ij} - \frac{1}{2}H_{+1\sigma,ij} + 2H_{\text{nom},ij} \right) \quad \text{if } k_j < -1. \quad (4.6)$$

Throughout the remainder of this thesis, this method is simply called *quadratic interpolation*. This interpolation function has, compared to the latter, no kink at  $k_j = 0$  but also describes the template shapes exactly at  $k_j = \pm 1$  and prevents significant deviations from a linear increase for  $|k_j| > 1$ .

If more than one nuisance parameter and consequently more than one systematic effect is regarded during the fit and thus during the interpolation step, the for-

#### 4 Profile Likelihood Analysis

mulae presented above need to be extended. This can be done by linearly adding the deviations from the nominal value caused by each effect to the nominal value  $H_{\text{nom},ij}$  which is only feasible because the nominal template applies to all nuisance parameters:  $H_{\text{nom},ij} = H_{\text{nom},i} \forall j$ .

Furthermore, an interpolation function depending on systematic variations larger than  $|1\sigma|$  can be defined as well. To better estimate this interpolation function, also templates which correspond to a  $\pm 2\sigma$ - and a  $\pm 3\sigma$ -variation of the related systematic uncertainty need to be available. The bin entries of a certain bin of all seven distributions (nominal with  $\pm 1\sigma$ -,  $\pm 2\sigma$ - and  $\pm 3\sigma$ -variations) which belong to one specific nuisance parameter  $k_j$  and one signal or background contribution are plotted as a function of  $k_j$ . Then, a quadratic fit to all these data points is performed (see Fig. 4.3, more information follows below). The  $\pm 2\sigma$ - and  $\pm 3\sigma$ -variations allow to increase the precision of the quadratic fit.

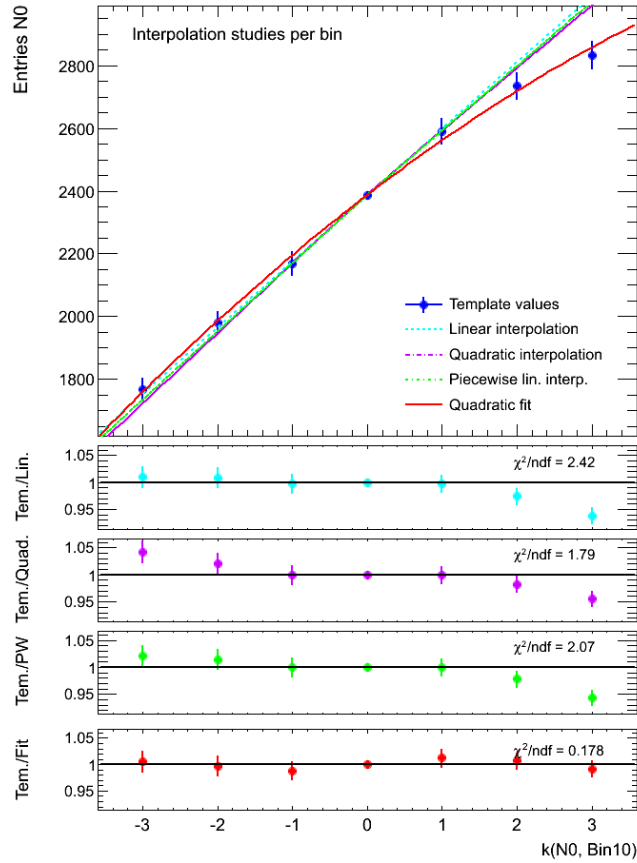


Figure 4.3: Interpolation curves of different interpolation methods for one exemplary bin. This plot is discussed in more detail in Chapter 6.2.2. The different bin entries of the underlying templates are marked in blue while the interpolation curves are coloured and hatched according to the legend. At the bottom, the ratios of the bin entry to the corresponding value of the interpolation curves are drawn.

The resulting fitted function serves as the interpolation function for the certain considered bin. Generalising this procedure to all bins  $i$  of all available input signal and background contributions and to all nuisance parameters  $k_j$  results in a new interpolation method which can be used apart from the other ones introduced above. In the following chapters, this interpolation method is referred to as *quadratic fit interpolation*.

Such a quadratic fit can certainly also be performed if only  $\pm 1\sigma$ -variations are available. Then, the quadratic interpolation introduced above and this fit-based interpolation resemble each other to a large extent, as long as  $|k_j| < 1$ , but if  $|k_j|$  exceeds one, the treatment of  $k_j$ -values is different.

The interpolation curves of all these morphing methods can be plotted for one single template bin including the bin entries of the underlying bin. These plots are studied more extensively in Chapter 6.2.2, one of the plots discussed there is already shown in Fig. 4.3 to visualise the behaviour of the different interpolation curves. Exemplarily, one bin of the signal distribution  $H_{N_0}$  containing the events with a longitudinally polarised  $W$  boson, based on the nuisance parameter  $k(\text{JES})$  is chosen. In the bottom half, the ratio of the bin entries, denoted as ‘‘Tem.’’, to the different interpolation curves at that position is calculated.

The resulting histogram  $H_{\text{int}}$  as the output of the morphing step serves to calculate  $H_{\text{sum}}$  which is fitted to  $H_{\text{data}}$  as explained in the previous section.

## 4.5 The Likelihood Function

The logarithmic likelihood function which is used in the minimisation process can be written with a set of systematic uncertainties  $\vec{k}$  added to the fit, with normalisation factors for the existing signal and with background contributions  $\vec{N}_S$  and  $\vec{N}_B$  as:

$$\begin{aligned}
 -2 \ln L(\vec{N}_S, \vec{N}_B, \vec{k}) = & 2 \sum_{m=1}^{N_{\text{bins}}} (H_{\text{sum},m} - H_{\text{data},m} \cdot \ln H_{\text{sum},m}) \\
 & + \sum_{i=1}^{N_{\text{bkg}}} \frac{(N_{B,i} - N_{B,\text{exp},i})^2}{\sigma_{N_{B,\text{exp},i}}^2} + \sum_{j=1}^{N_{\text{prof}}} k_j^2 + \text{norm.} \quad (4.7)
 \end{aligned}$$

$N_{\text{bins}}$  represents the number of bins of the corresponding templates,  $N_{\text{bkg}}$  the number of background parameters. The second sum of Eq. (4.7) is also called *penalty term* for the background parameters. This penalty term constitutes a Gaussian constraint with a mean of  $\mu_i \hat{=} N_{B,\text{exp},i}$  and a standard deviation of  $\sigma_i = \sigma_{N_{B,\text{exp},i}}$  and forces the fit result to be close to  $N_{B,\text{exp},i}$ . The explicit choice of both  $N_{B,\text{exp},i}$  and  $\sigma = \sigma_{N_{B,\text{exp},i}}$  depends on the measurement and the chosen fitting method.

The second last term constitutes a penalty allowing for a consideration of all nuisance parameters  $\vec{k}$  directly in the likelihood function. It equals a Gaussian constraint on  $\vec{k}$  with a mean of  $\mu = 0$  and a standard deviation of  $\sigma = 1$ . This choice reflects the expectation of the nuisance parameters possess Gaussian-shaped uncertainties, based on these values for  $\mu$  and  $\sigma$ .

The last constant term, abbreviated as ‘‘norm.’’, corrects the logarithmic likelihood so that it represents a normalised likelihood function.

## 4.6 Remarks Concerning the Implementation of the Fit

Two different methods to implement the profile likelihood fit are applied. One is based on a TMinuit minimisation where the corresponding commands are provided by the data analysis framework ROOT [72]. The minimisation function as well as the interpolation algorithm have to be set up individually compliant with the remarks stated above. HistFactory [73], which is based on RooFit [74], constitutes another tool with which such a profile likelihood fit can be performed. Both fitting techniques are referred to as TMinuit and HistFactory fit, respectively, throughout the remainder of this thesis.

The HistFactory fit provides a workspace allowing to directly define the various systematic uncertainties and the associated templates. The fit including the morphing step is then performed rather automatically so that no individual implementations are necessary. The HistFactory tool uses a piecewise linear interpolation by default and automatically imposes a Gaussian constraint on all nuisance parameters for which up and down variations are used in the fit. Moreover, a scale factor for the luminosity is added by default to the HistFactory fit as a further fit parameter. Its expected value and the associated uncertainty are defined in advance, following the remarks in Section 5.1.4. With the help of RooFit commands, the fitted values and different algorithms to calculate uncertainties can be accessed afterwards.

As the TMinuit fit is rather self-implemented with all its features, it allows for much more additional studies, e.g. various interpolation methods can be tested more easily. However, setting up the fit with two different tools enables a cross-check of the obtained results which thus helps to validate the quality and reasonableness of profile likelihood fits. Besides, the HistFactory tool offers an opportunity to easily perform pseudo-experiments. This is demonstrated in the next chapter, dealing with a measurement of the  $Wt$  production cross-section, in particular in Section 5.3.

## 4.7 Examples of Profile Likelihood Analyses

Recently, several studies have been performed based on profile likelihood fits to extract a certain signal out of a measured data set. For example, one of the most precise measurements of the top quark pair cross-section at ATLAS could be realised by using profile likelihood fits [75]. Also in the field of Higgs physics, those fits constitute an appropriate technique to gain possible signal events. After a new boson has been found at the LHC lately, profile likelihood fits may serve as a suitable opportunity to improve the measurements of this particle which is possibly the Higgs boson, i.e. reduce the contributing backgrounds [1, 2]. This underlines the significance of studying profile likelihood fits more extensively, as it is described in the subsequent chapters.

# 5 Measurement of the $Wt$ Production in the Muon+Jets Channel

This chapter focuses on the first measurement performed in the framework of this thesis: A measurement of the  $Wt$  production rate in the muon+jets channel. Since a profile likelihood fit is used in this analysis to measure the cross-section of single top quarks in the chosen production channel, emphasis is put on the setup of such a profile likelihood analysis. In comparison to the second measurement, discussed in the next chapter, in which a deeper understanding of the fitting method and the validation of the fit is in the centre of attention, it is mainly concentrated on the description of the planning as well as the implementation of the analysis and on the presentation of how a profile likelihood fit works, illustrating its advantages and strengths.

This chapter is organised as follows: First, some information about the fundamentals of the  $Wt$  production measurement - including selection and reconstruction, systematic uncertainties or the employed likelihood discriminant - is given. These topics are relevant for the measurement but outlined relatively briefly since an extensive description would exceed the scope of this thesis. In the subsequent section, the profile likelihood fit as it is used for this measurement is introduced whereas the third section serves to present the different obtained results.

## 5.1 $Wt$ Production: Fundamentals of the Measurement

In this section, simulated event samples, the definition of physics objects as well as various systematic uncertainties related to this analysis are described, followed by some information about the background estimation and the event analysis.

### 5.1.1 Simulated Event Samples and Data Samples

The data sample used in the following analysis is based on an integrated luminosity of  $\int \mathcal{L} dt = 2 \text{ fb}^{-1}$  and has been collected with the ATLAS experiment at a centre-of-mass energy of  $\sqrt{s} = 7 \text{ TeV}$ .

The calculation of the acceptances and the estimation of the background contributions was done with Monte Carlo generated samples, processed with the full ATLAS detector simulation based on GEANT4 and passed through the identical analysis chain used for the data [76, 77].

The signal  $Wt$  sample, the one for  $t\bar{t}$  as well as the samples for the other single top channels, which all constitute background samples, are produced with the MC@NLO generator [78–80] in combination with the CTEQ6.6 [34] parton distribution function (PDF) set using a top quark mass of  $m_t = 172.5 \text{ GeV}/c^2$ . These samples

are then normalised to cross-section computations at approximate NNLO [40–42]. ALPGEN generates the  $W$ +jets and  $Z$ +jets samples with the help of the MLM matching scheme [81] as well as the CTEQ6L PDF set [82]. The resulting cross-sections are again normalised to NNLO calculations afterwards, based on the FEWZ programme [83]. HERWIG [84] generates diboson events  $WW$ ,  $WZ$  and  $ZZ$ , which are normalised to NLO calculations based on MCFM [85]. QCD multijets events are modelled with ALPGEN. The QCD background estimation rests on data-driven methods whereas data is used to perform the  $W$ +jets background evaluation. The HERWIG shower model - interfaced to JIMMY [86] for the underlying event simulation - serves to hadronise the simulated Monte Carlo (MC) events.

Apart from that, particular samples are applied for systematic studies which are covered in Section 5.1.4. Both the generator (MC@NLO or POWHEG) and the showering model (HERWIG or PYTHIA) [87, 88] are varied for this purpose. Parameters that are responsible for altering the initial state (ISR) and final state radiation (FSR) are merely varied in the PYTHIA programme. The latter, though, cannot be interfaced to MC@NLO which means that the leading-order generator AcerMC [89], interfaced to PYTHIA, is applied for the determination of the systematic effects caused by the uncertainties originating from ISR and FSR.

### 5.1.2 Definition of Physics Objects

The analysis concentrates on the  $Wt$  production in the muon+jets channel excluding electrons so that the event reconstruction solely requires reconstructed muons, jets and missing transverse energy. This procedure conforms to the common top group recommendations [90], supplemented by an additional muon isolation requirement. The electron selection is described as well, since electron-related systematic uncertainties still need to be considered.

**Muons** All triggered muon events require a first level (L1) muon trigger chamber track associated with a 11 GeV transverse momentum  $p_T$ -threshold which is assigned to a muon track detected and reconstructed at the EF trigger level. The corresponding  $p_T$ -threshold of the EF trigger is set to 18 GeV. Further information about the ATLAS trigger system can be found in Section 3.3.5.

These muon spectrometer hits are then matched with tracks recorded by the Inner Detector in order to fully reconstruct muon candidates. For that purpose, the complete track information of both subdetectors is exploited and also material effects are considered. Final candidates must exceed a transverse momentum of  $p_T > 25$  GeV and need to be in the pseudorapidity region of  $|\eta| < 2.5$ . Moreover, other - especially Inner Detector - requirements have to be fulfilled by the muon candidates. For instance, they must satisfy an isolation requirement and a classification as tight is essential. Isolation criteria are used to reduce the amount of background events with a muon having large  $p_T$  coming from a heavy flavour decay; those muons are usually within a jet. A correct reconstruction of the muon momentum furthermore requires scale shifting and resolution smearing. Eventually, muon identification efficiencies are measured and adequate, necessary correction factors are derived [91].

**Electrons** At the first trigger level, electrons are expected to have an energy of  $E_T > 16$  GeV. The trigger electron object then requires  $E_T > 22$  GeV with the energy resulting from the EM scale. With the help of  $Z \rightarrow ee$  and  $W \rightarrow e\nu$  events, the trigger efficiency and the data/MC efficiency ratio can be estimated.

Selected offline electrons possess values of  $p_T > 25$  GeV and  $|\eta_{cl}| < 2.47$  where  $\eta_{cl}$  refers to the EM cluster position. Electrons detected in the barrel-endcap overlap region of the ATLAS calorimeter system with  $1.37 < \eta_{cl} < 1.52$  are removed. For a successful object selection, the matching with a trigger object is essential. Furthermore, isolation criteria are applied to suppress photon conversions and other background events related to jet activity like hadronic jets that fake electrons or electrons that originate from heavy flavour processes. Besides, a correction of the electromagnetic cluster energy is required. Correction scale factors concerning trigger, identification and reconstruction can finally be determined.

**Jets** The anti- $k_t$  algorithm [92, 93], which behaves like an idealised cone algorithm, employing a width parameter  $\Delta R$  of 0.4 using so-called topoclusters from the 4/2/0 clustering algorithm is applied to reconstruct jets. A calibration of these jets from the electromagnetic scale with the help of MC-based correction factors for  $p_T$  and  $\eta$  is performed. Such a factor corrects, on average, the measured jet- $p_T$  to the particle level in the simulations. Imposing further jet reconstruction requirements ensures a rejection of jets which are suspected to have arisen from detector noise. After the application of cleaning cuts, jets are counted if  $p_T > 25$  GeV and  $|\eta| < 2.5$  [94].

**Missing Transverse Energy** Missing transverse energy  $E_T^{\text{miss}}$  is defined as the amount of energy which is not measured by a detector but anticipated because of conservation laws regarding energy and momentum. As  $E_T^{\text{miss}}$  thus constitutes a measure of the momentum of the non-detectable and therefore escaping neutrinos, it can be computed as the vector sum over all topoclusters belonging to the event. However, this quantity also comprises energy losses caused by the detector resolution and detector inefficiencies. In this analysis, it is further refined by corrections at object level for contributions which are due to identified leptons or jets.

**b-Tagging** The unique properties of  $b$  jets allow to distinguish these jets from those originating from the hadronisation of lighter jets. In particular, the existence of a secondary vertex facilitates the identification of  $b$  jets out of lighter ones, as already mentioned in Section 2.2.2, and is referred to as  $b$ -tagging.

The *IP3D+JetFitter*  $b$ -tagging algorithm [95], as a combination of the *IP3D* and the *JetFitter* algorithm, is employed for the  $Wt$  production rate measurement. The *IP3D* tagger is based on a likelihood ratio technique to differentiate between light and  $b$  jets while the latter applies a Kalman filter to obtain the positions of the  $b$ - and  $c$ -vertices. The chosen tagger *IP3D+JetFitter* eventually merges the results of the two algorithms by using an artificial neural network. With a weight cut of 2.0, a  $b$ -tagging efficiency of 60% is achieved [95].

### 5.1.3 Event Selection

The selection of single top events in the analysed  $Wt$  channel is realised in two steps: The first one selects events in data and MC with a single top signature. The composition of the data sample is computed by applying the background model to the corresponding events. The application of tighter selection cuts is performed in the second step. This step serves to isolate the single top signal, which is composed of events with 2 (excl.), 3 (excl.) and 4 (incl.) jets including one or at least two jets tagged as  $b$  jets. The requirements of this step can be summarised as follows:

All suitable events are required to pass various cleaning cuts to be selected. Selected events need to contain exactly one isolated muon with  $p_T > 25$  GeV and  $E_T^{\text{miss}} > 25$  GeV apart from at least two jets with  $p_T > 25$  GeV with one exclusively and two inclusively tagged  $b$  jets. A QCD multijet veto is applied because fake leptons from QCD multijet events tend to have a low transverse  $W$  boson mass and a low  $E_T^{\text{miss}}$  with respect to signal events so that events need to fulfil:  $m_T(W) + E_T^{\text{miss}} > 60$  GeV [96]. In addition, the loss of front end boards in the liquid argon calorimeter in 2011, leading to a hole in the calorimeter coverage, is considered in the MC simulations by reweighting the samples [97].

### 5.1.4 Systematic Uncertainties

The evaluation of systematic uncertainties follows the common top group prescription and standard ATLAS procedures [98]. As up- and down-variations of the different systematic uncertainties are needed for the profile likelihood analysis, all qualified systematics are varied to produce the corresponding samples. The different sources of systematic uncertainties used in the fit are described in depth in the following:

**Lepton Energy Scale and Resolution**<sup>1</sup> The effect of the lepton energy scale uncertainty (EES for electrons, MS\_SCALE for muons) on the selected event sample is estimated by scaling the transverse momentum of the lepton up and down by  $\pm 1\sigma$ .  $Z \rightarrow ee$  and  $Z \rightarrow \mu\mu$  events are used for this calculation. The evaluation of the impact of the lepton energy resolution depends on the underlying lepton: In case of electrons (EER), the electron energy is smeared in data to estimate the effect. In case of muons, the estimation is performed technically in the same way but individually in the muon spectrometer (MUS\_MS) and the Inner Detector (MUS\_ID).

**Jet Energy Scale and Resolution** The jet energy is of fundamental importance in physics analyses. The aim of measuring this quantity is the determination of the original parton momentum at the origin of the jet. Therefore, an energy correction needs to be evaluated so that the jet energy measured in the calorimeter cells can be scaled first to the energy of the particles constituting the final states of detected events and then to the underlying partons. This reconstruction of momenta at parton level enables a comparison with theoretical calculations. In the context of such

<sup>1</sup>Although the  $Wt$  production is analysed in the muon+jets channel in this report, the selected events with one good muon may include electrons so that the analysis is still sensitive to this lepton and the associated uncertainties thus need to be taken into account.

jet energy and jet energy scale (JES) measurements the corresponding uncertainties need to be taken into consideration:

The size of the JES uncertainty can be calculated with the help of two parameters of the reconstructed jet:  $p_T$  and  $\eta$ . A certain tool called MultijetJESUncertaintyProvider scales the energy of all jets by  $\pm 1\sigma$ . Depending on these quantities  $p_T$  and  $\eta$ , the JES uncertainty varies between 2% and 5% in the central region and between 3% and 7% in the forward region of pseudorapidity. Uncertainties due to pile-up events (5% in the central, 8% in the forward region) or  $b$ -tagged jets (1.1%-3.2%) are also taken into account, where the term ‘‘pile-up’’ refers to multiple proton-proton interactions in the same bunch crossing.

The jet energy resolution (JER) needs to be considered as well. Its impact is determined by smearing the jet energy in data. The associated uncertainty amounts to 4-45%.

**Jet Reconstruction Efficiency** The jet reconstruction efficiency (JEFF) occasions a systematic uncertainty whose estimation is based on the idea of randomly dropping jets from events. The variation from the nominal sample can then be calculated directly. Assigned are uncertainties of 1-2%.

**Missing Transverse Energy** Two additional systematic uncertainties need to be considered in the context of missing transverse energy.

- a) Uncertainties due to a soft jet with  $p_T < 20$  GeV not included in the jet-related uncertainties from above and due to unassociated calorimeter cells, which are assumed to be 100% correlated, constitute one uncertainty ( $E_T^{\text{miss}}$ ).
- b) Further pile-up effects influence the  $E_T^{\text{miss}}$ -determination leading to a second uncertainty ( $E_T^{\text{miss}} + \text{pile-up}$ ).

**$b$ -Tag Heavy Flavour and Light Flavour Scale Factor Uncertainty** This uncertainty accounts for the  $b$ -tagging data and Monte Carlo scale factor. It is estimated in the MC samples - individually for  $b$  and  $c$  quarks as heavy flavour quarks (BTAG) and for light flavour quarks (MISTAG), abbreviated as  $l$  quarks. The size of the associated uncertainties amounts to 9%-16% and 12%-45%, respectively.

**Initial and Final State Radiation (ISR/FSR)** An additional uncertainty arises due to the dependence of both the signal acceptance and the  $t\bar{t}$  background uncertainty on the ISR/FSR model. It can be evaluated by using a set of single top and  $t\bar{t}$  samples generated with AcerMC+PYTHIA with several different ISR/FSR tunes (Perugia Soft/Hard tune variations [99] are used), which is equivalent to a separate and simultaneous change of ISR and FSR contributions.

**MC Generator and Parton Shower Modelling** Also the modelling of MC events and the parton shower model lead to systematic effects on the samples. These effects are only calculated for the  $t\bar{t}$  background and can be estimated by comparing the MC@NLO and POWHEG generators using POWHEG+PYTHIA (POWPHY) and POWHEG+HERWIG (POWHE).

**Background Cross-Section Normalisation** The uncertainties on the cross-section of several background sources, for example, caused by scale variations or PDFs, constitute further systematic uncertainties. The acceptance from cross-sections obtained from MC and theoretical predictions is exploited to estimate the event yields from  $t\bar{t}$ ,  $Z$ +jets and diboson (di) processes. Cross-section uncertainties are assigned as follows: 10% to the  $t\bar{t}$ , 5% to the diboson and 60% to the  $Z$ +jets background.  $s$ - and  $t$ -channel as other non-signal single top processes (single top) are assigned with an uncertainty of 14%.

The various  $W$ +jets samples possess cross-section uncertainties which are evaluated on the basis of an uncertainty of 100% for both the  $Wb\bar{b}+Wc\bar{c}$  fractions and the  $Wc$  fraction. These systematics are abbreviated as “ $Wb\bar{b}+Wc\bar{c}$ ” and “ $Wc$ ” in the following. An uncertainty of 25% is furthermore applied in all the  $Wb\bar{b}+Wc\bar{c}$  and  $Wc$  samples individually between the rates of any two jet bins; these uncertainties are referred to as “ $Wb\bar{b}+Wc\bar{c}$ jet” and “ $Wc$ jet”.

**$W$ +jets Shape Uncertainty** In the context of  $W$ +jets background processes, a shape uncertainty has to be taken into consideration. It is based on the variation of different parameters, namely the ALPGEN parameters `ptjmin` and `iqopt3`, while producing the  $W$ +jets samples, resulting in a reweighting of these  $W$ +jets samples afterwards.

**QCD or Fake Lepton Background Normalisation** A fitting method, which is briefly explained in Subsection 5.1.5, is used to normalise the QCD multijet or fake lepton background. Comparing this procedure to an alternative QCD multijet background evaluation leads to a systematic uncertainty of 50%. This effect is assumed to be uncorrelated so that the systematic variation is done separately in both the signal and pretagged sample resulting in two systematic uncertainties, called QCD and preQCD.

**Luminosity** The uncertainty on the luminosity (LUMI) amounts to 3.9% for the 2011 data-taking period on which this measurement is based [100].

### 5.1.5 Background Estimation

The estimation of different background rates is addressed in this subsection. To begin, the numerous background contributions in the lepton+jets channel are discussed, followed by a closer examination of the  $W$ +jets and the QCD multijet background. In order to obtain shape and normalisation of the remaining backgrounds, MC samples and theoretical cross-sections are employed. The chosen procedure affects parameters used in the profile likelihood fit.

#### Background Contributions in the Lepton+Jets Channel

The background due to  $W$ +jets production which can arise because one of the jets is a heavy flavour jet or because of the misidentification of a light jet as a bottom one is the most relevant background for single top quark production and dominant in

the 2-jet signature.  $t\bar{t}$  production constitutes the most important background contribution in the 4-jet signature. The  $t\bar{t}$ -related lepton+jets signature is comparable to the corresponding  $Wt$ -related lepton+jets signature, just a second  $b$  jet which is not accurately tagged as a jet coming from a  $b$  quark needs to exist. A relevant instrumental background is QCD multijet production, as introduced above. Hadronic jets misidentified as a lepton or by the occurrence of isolated, high- $p_T$  leptons found within a jet due to a semileptonically decaying heavy flavour hadron are responsible for this background contribution. Further but smaller background sources are diboson production, namely  $WW$ ,  $WZ$  and  $ZZ$ , and  $Z$ +jets events.

### The $W$ +Jets Background

As the normalisation and the heavy flavour fractions in the  $W$ +jets sample are not precisely known, the systematic uncertainties on the fractions  $Wb\bar{b}+Wc\bar{c}$  and  $Wc$ , as shown in Section 5.1.4, are comparatively large. In order to reduce the sensitivity to these uncertainties, data-driven methods have been set up to obtain the  $W$ +jets background directly from data. These methods are commonly based on the tagging fractions in the selected samples with one or two jets or on charge asymmetry, which means that the asymmetric cross-sections for both negatively and positively charged prompt leptons coming from the  $W$  boson decay serve to gain the  $W$ +jets events. Since the LHC is a  $pp$  collider, negatively charged  $W$  bosons can solely originate from sea quarks, thus causing this asymmetry.

The evaluation of correction factors for the normalisation and the heavy flavour fractions of the  $W$ +jets samples is necessary to appropriately predict the number of background events in the signal region, namely  $b$ -tagged  $Wb\bar{b}$ ,  $Wc\bar{c}$ ,  $Wc$  and  $Wll$  events with a light lepton  $l$ . The unknown normalisation factors are usually denoted as  $K$ -factors which need to be determined for three flavours:  $b\bar{b}$ ,  $c$  and  $ll$  - because the ones for  $b\bar{b}$  and  $c\bar{c}$  are supposed to be identical. To extract them, seven different scenarios exist in total, which can be found in Table 5.1. The different listed scenarios include a variation of the number of jet bins, the use of charge asymmetry (CA), as depicted above, or the use of an additional factor  $K_{t\bar{t}}$  in order to consider contributions from  $t\bar{t}$  events.

Scenario	Description
1	1-4 jets in final state, CA, $K_{t\bar{t}}$ fit
2	1+2 jets in final state, CA, no $K_{t\bar{t}}$ fit
3	1-4 jets in final state, CA, no $K_{t\bar{t}}$ fit
4	1-4 jets in final state, no CA, $K_{t\bar{t}}$ fit
5	1+2 jets in final state, no CA, no $K_{t\bar{t}}$ fit
6	1-4 jets in final state, no CA, no $K_{t\bar{t}}$ fit
7	1+2 jets in final state, analytical

Table 5.1: Overview of the seven different scenarios for the evaluation of the  $K$ -factors. They are specified by the number of jets in the final state (the used jet bins), by the use of charge asymmetry or by the factor  $K_{t\bar{t}}$ .

The evaluation of the  $K$ -factors in the signal region can be described as follows: Event migrations occurring between the jet bins are caused by the uncertainties which arise because of initial and final state radiation. The signal is thus obtained from a combination of the 2-(excl.)-, 3-(excl.)- and 4-(incl.)-jet bin although a majority of  $Wt$  signal events is anticipated to be in the 3-jet bin. The signal region then constitutes the amount of events remaining after the application of a cut on the likelihood discriminant. By using pseudo-data, the chosen cut value of 0.6 can be extracted. To then find the most suitable scenario to obtain the  $K$ -factors, pseudo-data is used. To be more exact, the analysis is performed based on pseudo-data and redone for all considered systematic variations. Scenario 6 (according to the numbers given in Table 5.1) with all four jet bins, no  $t\bar{t}$  contributions for the fit and no charge asymmetry leads to most adequate results. The observed systematic uncertainties are comparable in all jet bins and remarkably correlated between these different jet bins and flavours.

### The QCD Multijet Background

A matrix method [101, 102] is exploited to estimate the QCD multijet background using the event yields from data after tight and loose lepton selections,  $N^{\text{tight}}$  and  $N^{\text{loose}}$ , are applied. The tight event selection criteria complies with the lepton identification criteria stated above whereas the loose selection is based on the same criteria excluding the lepton isolation requirements.

The background can then be determined as a function of these event yields and as a function of both the fake and the real efficiency of the matrix method,  $\varepsilon_{\text{fake}}$  and  $\varepsilon_{\text{real}}$ . Except for the statistical uncertainties on these four variables, an appropriate evaluation of the QCD multijet background requires the consideration of several further effects. Two relevant ones are a contamination effect caused by prompt muons or the so-called cross-talk with the  $W$ +jets normalisation.

#### 5.1.6 Event Analysis and Likelihood Discriminant

A likelihood discriminant serves to extract the  $Wt$  production single top events after the preselection. In total, about 70 variables have been tested to estimate their quality as possible discriminators between the desired  $Wt$  signal and background events. For instance, four-momentum variables of  $b$ -tagged or untagged jets, muons, reconstructed  $W$  bosons or reconstructed top quarks, different event kinematics, the sum of the momenta  $H$  and the sum of the transverse momenta  $H_T$  of different object combinations, variables like sphericity and aplanarity and angular correlation variables have been explored. None of these variables yields an adequate signal isolation, which means that a simple sequential cut-based analysis is not sensitive enough, and a likelihood discriminant is applied instead. The tool TMVA (ROOT Toolkit for Multivariate Data Analysis) [103] allows for a combination of several variables. In particular, the following three are chosen: pseudorapidity of the muon in the event  $\eta(\mu)$ , distance between the first and the second jet  $\Delta R(j_1, j_2)$  and the sphericity using all involved jets and including single muon as these variables reflect a compromise between mitigation of systematic effects, discrimination power and stability of the discriminant.

## 5.1 $Wt$ Production: Fundamentals of the Measurement

From these discriminating input variables, the likelihood discriminant is constructed after carrying out a Gaussian transformation with the help of the projective likelihood option provided by the TMVA package. The likelihood discriminant  $y_{\mathcal{L}}$  is defined as the ratio of the signal to the sum of signal and background likelihoods leading to the following expression for a certain event  $i$ :

$$y_{\mathcal{L}}(i) = \frac{\mathcal{L}_S(i)}{\mathcal{L}_S(i) + \mathcal{L}_B(i)}.$$

The individual likelihoods  $\mathcal{L}_{S/B}(i)$  are products of the related probability functions of the discriminating input variables. Linear correlations measured in the training sample and being used to decorrelate the input variables separately for background and signal events are taken into account by the tool TMVA. As the training of the likelihood classifier is based on simulated events, the modelling of the output distribution has to be tested with observed events.

The number of jets separates the signal sample into different independent analysis channels. After a normalisation to the luminosity, the resulting discriminant distributions are thus produced individually for different jet multiplicities. As requested, the data is well distributed over the entire discriminant range while the signal is explicitly visible above the background contributions for large likelihood response values, as shown in Fig. 5.1.

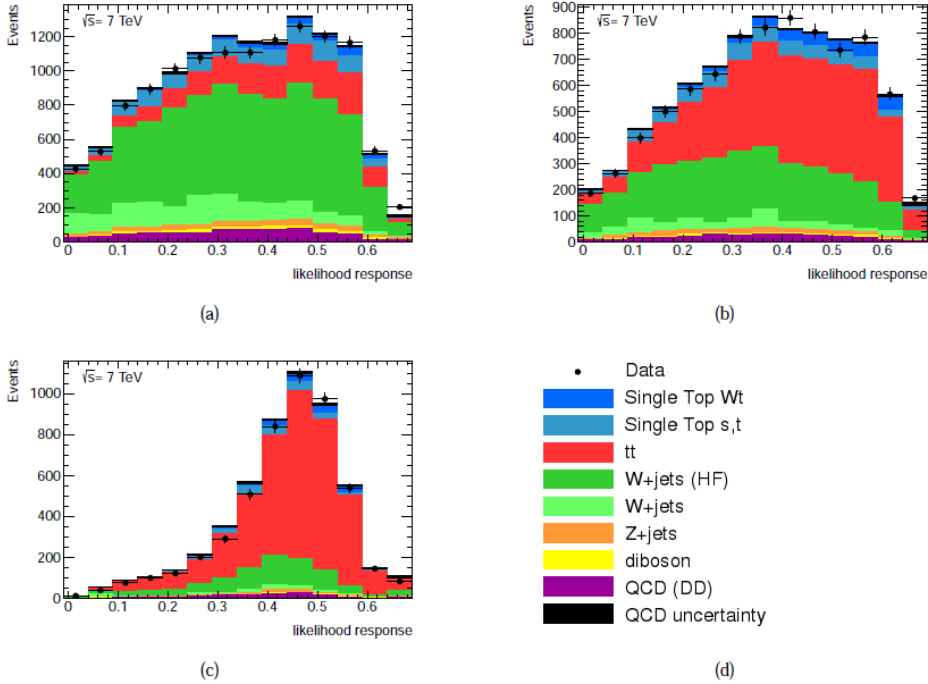


Figure 5.1: Likelihood discriminant distrib. resulting from the input variables  $\eta(\mu)$ ,  $\Delta R(j_1, j_2)$  and sphericity for different jet multiplicities: The (a) 2-excl.-, (b) 3-excl.- and (c) 4-incl.-jet bins after  $b$ -tagging as well as (d) the related legend [104].

## 5.2 Profile Likelihood Fits to Measure the $Wt$ Production Cross-Section

The profile likelihood analysis in the context of a cross-section measurement of single top quarks in the  $Wt$  production channel is further discussed in this section after the main aspects of profile likelihood fits have already been introduced in Chapter 4.

### 5.2.1 Technical Aspects

The interpolation or morphing step as part of the profile likelihood fit in which the shape of the corresponding templates is morphed from  $H(-1\sigma)$  to  $H(\text{nominal})$  to  $H(+1\sigma)$  was already explained in Section 4.3. To measure the  $Wt$  production rate, the interpolation step is performed separately for signal  $S$  and background  $B$ , which means that two distributions or histograms constitute the output of this interpolation,  $H_S$  and  $H_B$ .

These two histograms depend on the nuisance parameters  $\vec{k}$ , on a signal parameter  $N_{Wt}$  and on background parameters  $\vec{N}_B$ , where  $N_{Wt}$  acts as a normalisation or scale parameter. Those parameters constitute prefactors with which each template or, to be more accurate, each bin of the corresponding histogram is multiplied. The background parameters are addressed in the next paragraph.

The input templates used in the interpolation step are discriminant distributions based on the likelihood discriminant introduced in the last paragraph. More information about the distributions, which comprise events with 2 (excl.), 3 (excl.) or 4 (incl.) jets, can be found in Subchapter 5.2.3. The templates for each systematic variation (up and down) result from Monte Carlo simulation whereas the data-driven background determination is reperformed for all systematic variations. This allows for a propagation of potential effects in data to the analysis.

For this measurement, a piecewise linear interpolation is applied, as it was introduced in Section 4.4.

Starting from  $H_S$  and  $H_B$ , the distribution  $H_{\text{sum}}$ , which is then fitted to the data distribution  $H_{\text{data}}$ , can be calculated. Two different fitting procedures are discussed for the  $Wt$  production measurement.

The first approach is based on using three additional normalisation parameters for the background to adjust the size of the background, separately for each bin:  $N_{B,i}$  with  $i = 2, 3, 4$  while  $i$  denotes the jet bin, in other words, the number of jets in the associated events. In this particular case,  $H_{\text{sum}}$  is derived according to  $H_{\text{sum}}(\vec{k}, \vec{N}_B, N_{Wt}) = H_S(\vec{k}, N_{Wt}) + H_B(\vec{k}, N_{Wt}) \cdot N_B$  where  $N_B$  represents a factor which includes all background parameters  $N_{B,i}$ . An additional fit parameter operating as a scale factor of the signal distribution  $H_S$  is not implemented. This is due to the fact that the signal also affects the background templates to a certain extent since these background estimates are data-driven. The corresponding effect is absorbed in the up- and down-templates with a variation of the  $Wt$  signal of 100%. The signal parameter  $N_{Wt}$  is thus fitted as if it were a nuisance parameter fitting shape and normalisation of *both* the signal and background templates during the minimisation process.

As the  $N_{B,i}$  function as prefactors, they scale the entire background distributions entering the fit which may result in undesired correlations. This is due to the fact that it is sufficient to only express the  $W$ +jets background normalisation with these parameters. The different nuisance parameters  $\vec{k}$  fit their underlying backgrounds that are taken from Monte Carlo, except the QCD multijet background, which is extracted from data, so that only one single background shape ( $W$ +jets) is applied. The use of scale parameters would require the availability of all individual background shapes.

As a consequence, a second fitting procedure is set up with three background parameters  $N_{B,i}$  acting as nuisance parameters. Normalisation and shape are then fitted properly within the one available background shape. To perform a fit in this way,  $\pm 1\sigma$ -templates including up- and down-variations for the  $N_{B,i}$  need to be on hand. They can be gained from pretagged information based on the related statistical uncertainties. These fit parameters enable an appropriate scaling of the  $W$ +jets background, the input template contain all necessary information. The signal parameter  $N_{Wt}$  is treated as in the first approach. The histogram which is finally fitted to data composed of signal and background histograms is of the form:  $H_{\text{sum}}(\vec{k}, \vec{N}_B, N_{Wt}) = H_S(\vec{k}, \vec{N}_B, N_{Wt}) + H_B(\vec{k}, \vec{N}_B, N_{Wt})$ .

The studies shown in this chapter are based on this second improved and more precise method. The first fitting method as being a rough approach serves to cross-check the obtained results, which can be found in App. B.

For the minimisation process, the likelihood function expressed in Eq. (4.7) is employed. If the first fitting method is used, the mean values of the background parameter constraints are set to one, forcing the fit result to be close to this value as well. The related uncertainties are explicitly given in App. B where the fit is analysed. If the background parameters are treated as nuisance parameters, the mean values of the Gaussian prior are consequently zero, the standard deviation is set to one.

### 5.2.2 Nuisance Parameters and Other Fit Parameters

Except for the 28 different systematics defined and described in Subsection 5.1.4, three further uncertainties, those on the  $K$ -factors  $K_{bb}$ ,  $K_c$  and  $K_{ll}$ , as given in Subchapter 5.1.5, enter the profile likelihood fit. In total, 35 fit parameters are thus used, taking  $N_{Wt}$  and the three background parameters into consideration. To adjust the size of the different systematic uncertainties,  $\pm 1\sigma$ -templates are available, separately for the signal and background contributions for all corresponding nuisance parameters. The start values of these parameters for the minimisation process are zero since they are expected to be Gaussian-distributed around this value. As long as the second fitting method is used, the initial values of  $N_{Wt}$  and  $N_{B,i}$  are zero as well. If the  $N_{B,i}$  function as scale factors, they are assumed to be one resulting in start values of  $N_{B,i} = 1 \forall i$ .

In Chapter 6.3.2, it is further discussed for which systematics such a profile likelihood fit is not essential and which systematic effects cannot even be adequately described by nuisance parameters. But to test the behaviour and influence of as much systematic effects as possible, all available effects are fitted via nuisance parameters here.

### 5.2.3 Discriminant Distributions Used for the Fit

Discriminant distributions which are differentiated by the number of jets, as covered above, serve as input to the profile likelihood fit. In total, six different distributions for six different decay channels are available, for events with 2 (excl.), 3 (excl.) and 4 (incl.) jets in the final state, as before referred to as 2-, 3- and 4-jet bin, separated further into events with one exclusively or two inclusively tagged  $b$ -jets. Seven different scenarios exist to derive the  $W$ +jets background and hence to evaluate the  $K$ -factors, introduced in Section 5.1.5. Most of the studies presented in this chapter rest on scenario 6 - according to the numbers in Table 5.1 - since this one has been proven to yield the most adequate results. Nonetheless, some tests with other scenarios are shown as well.

The limited statistics leads to a straitened potential of the fit. To exploit it as effectively as possible, all six different input samples, for all the channels, are combined. This combined distribution then functions as input histogram.

Before combining or merging the histograms in such a way, a binning of the templates is essential to have sufficient stability and enough statistics during the fit. Binned templates in which the entries of all of the six single input channels given above with a likelihood discriminant ranging from zero to one ( $0 \leq y_{\mathcal{L}} \leq 1$ ) are pooled into 14 bins are used for the fits whose results are shown in the next section. The first 13 bins include the entries belonging to a discriminant range of  $0 \leq y_{\mathcal{L}} \leq 0.65$  with range of  $\Delta y_{\mathcal{L}} = 0.05$  covered by each bin. The last bin comprises the remaining entries as solely a few events feature such large discriminant values. For reasons of clarity, the new histogram that contains 84 bins after merging, defined to be equal in width, ranges from zero to six meaning that each of the six jet-bin distributions covers a segment having size one on the abscissa as the discriminant axis.

A number of tests varying the number of bins have been done in order to find an adequate binning method. Using too few bins, however, may lead to a significant information loss concerning the shape of the distribution. On the other hand, MC fluctuations may influence the profile likelihood fit if the binned histogram is composed of 20 or more bins. An increase in the number of bins could have a noticeable effect on the fit results - especially in the signal region with fewer events where the discriminant exceeds  $y_{\mathcal{L}} = 0.7$  - caused by those fluctuations.

### 5.2.4 Cross-Section Measurements with Profile Likelihood Fits

The relation between the measured  $Wt$  production cross-section  $\sigma_{Wt}$  and the associated SM expectation  $\sigma_{Wt,SM}$ , as given in Table 2.4, yields:

$$\frac{\sigma_{Wt}}{\sigma_{Wt,SM}} = N_{Wt} + 1. \quad (5.1)$$

This equation is used in this analysis to directly calculate the searched cross-section with the help of the profile likelihood fit results including the signal parameter  $N_{Wt}$ . It reveals that a fitted signal parameter of zero corresponds to a  $Wt$  production cross-section equivalent to the expectation from the Standard Model.

## 5.3 *Wt Production Cross-Section: Results*

The results from different profile likelihood fits set up to calculate the *Wt* production cross-section are described on the subsequent pages. Besides presenting cross-section results, emphasis is also placed on the presentation of a number of studies and tests performed with the different profile likelihood implementations using also already existing tools in order to illustrate the setup of such fits.

It is concentrated on fits using nuisance parameters to adjust the background contributions. As explained in Section 5.2.1, such a fitting method is more elaborate in contrast to the approach using background parameters as scale factors. In order to compare the different methods quantitatively, the latter is outlined in App. B.

The implementations of all fits follow the remarks stated in Chapter 4.6 where two different tools for the fit, TMinuit and HistFactory, have been introduced. Most of the results are gained from TMinuit fits resting on an individually implemented code that allows for more different setups and test options while the HistFactory tool, as it performs the fit rather automatically, serves to cross-check the different results. The use of the HistFactory framework in this analysis is advantageous since it provides a tool with which pseudo-experiments can be performed relatively fast and straightforward.

### 5.3.1 Profile Likelihood Fits Using Background Parameters as Nuisance Parameters

The fitting method based on using  $\pm 1\sigma$ -templates for the background parameters consequently treating them as nuisance parameters is implemented in such a way that the background is scaled properly according to the applied background shape, as explained in Section 5.2.1. The resulting distribution  $H_{\text{sum}}$  originating from this procedure and fitted to data is of the form:  $H_{\text{sum}} = H_S + H_B$ , by neglecting the dependencies.

The results of this fit, which is performed with both the TMinuit and the HistFactory tool as a cross-check, are listed in Table 5.2 and underline the consistency between these two techniques. The differences between the parameter values from both implementations are only in some cases larger than 5%. The fit parameter for the luminosity of the HistFactory fit which functions as a scale factor is very close to one and does thus not noteworthy affect the fit result. To conclude, the HistFactory fit acts as an appropriate cross-check of the TMinuit fit.

The uncertainties on the fit parameters can be directly obtained from the TMinuit fit by using different algorithms. A Hesse algorithm based on the Hessian matrix can be applied. This evaluation considers the full matrix of second derivatives of the function with regard to the variable fit parameters. The given uncertainties comprise both the statistical and the systematic uncertainty of the fit since all nuisance parameters are added to the fit which account for the different systematic effects.

Instead of this Hesse algorithm for the estimation of the uncertainties, also an asymmetric and more sophisticated Minos algorithm can be employed, which is more

5 Measurement of the  $Wt$  Production in the Muon+Jets Channel

Fit: Uncertainty: Parameter	TMinuit			HistFactory
	Hesse	Minos		Hesse
$N_{Wt}$	$0.40 \pm 0.56$	-0.56	+0.57	$0.39 \pm 0.55$
$N_{B,2}$	$-0.06 \pm 1.00$	-1.00	+1.00	$-0.07 \pm 0.99$
$N_{B,3}$	$0.10 \pm 1.00$	-1.00	+0.99	$0.09 \pm 0.99$
$N_{B,4}$	$-0.04 \pm 1.00$	-1.00	+1.00	$-0.05 \pm 0.99$
$k(WbbWc\bar{c})$	$0.00 \pm 1.00$	-1.00	+1.00	$0.00 \pm 0.99$
$k(WbbWc\bar{c}\text{jet})$	$-0.70 \pm 0.42$	-0.46	+0.41	$-0.70 \pm 0.42$
$k(Wc)$	$-0.00 \pm 1.00$	-1.00	+1.00	$-0.00 \pm 0.99$
$k(Wc\text{jet})$	$-0.92 \pm 0.61$	-	+0.60	$-0.91 \pm 0.61$
$k(\text{MISTAG})$	$-0.89 \pm 0.67$	-0.67	+0.67	$-0.90 \pm 0.67$
$k(\text{BTAG})$	$0.49 \pm 0.14$	-0.15	+0.11	$0.49 \pm 0.14$
$k(\text{di})$	$-0.01 \pm 1.00$	-1.00	+1.00	$-0.01 \pm 0.99$
$k(\text{EER})$	$-0.04 \pm 0.78$	-0.91	+0.37	$-0.05 \pm 0.80$
$k(\text{EES})$	$0.13 \pm 0.15$	-0.18	+0.15	$0.13 \pm 0.15$
$k(\text{FSR})$	$0.15 \pm 0.30$	-0.30	+0.16	$0.15 \pm 0.30$
$k(\text{iqopt3})$	$-0.10 \pm 1.00$	-0.99	+1.00	$-0.10 \pm 0.99$
$k(\text{ISR})$	$-0.40 \pm 0.19$	-0.24	-	$-0.40 \pm 0.19$
$k(\text{JEFF})$	$-0.44 \pm 0.76$	-0.76	-	$-0.45 \pm 0.76$
$k(\text{JER})$	$0.62 \pm 0.33$	-0.33	+0.36	$0.61 \pm 0.33$
$k(\text{JES})$	$-0.19 \pm 0.17$	-0.16	-	$-0.19 \pm 0.17$
$k(K_{bb})$	$0.14 \pm 0.54$	-0.53	+0.53	$-0.07 \pm 0.94$
$k(K_c)$	$-0.21 \pm 0.96$	-0.96	+0.97	$-0.27 \pm 0.98$
$k(K_{ll})$	$0.03 \pm 0.98$	-0.98	-	$0.08 \pm 0.99$
$k(E_T^{\text{miss}})$	$0.18 \pm 0.59$	-	-	$0.20 \pm 0.64$
$k(E_T^{\text{miss}} + \text{pile-up})$	$0.29 \pm 0.69$	-1.33	+0.70	$0.30 \pm 0.69$
$k(\text{MS\_SCALE})$	$0.00 \pm 0.08$	-0.22	-	$-0.00 \pm 0.10$
$k(\text{MUS\_ID})$	$0.39 \pm 0.63$	-0.78	+0.64	$0.39 \pm 0.63$
$k(\text{MUS\_MS})$	$-0.00 \pm 0.04$	-0.13	+0.12	$-0.00 \pm 0.05$
$k(\text{POWHE})$	$1.03 \pm 0.50$	-0.50	+0.51	$1.03 \pm 0.49$
$k(\text{POWPY})$	$0.24 \pm 0.50$	-0.50	+0.50	$0.24 \pm 0.49$
$k(\text{preQCD})$	$0.24 \pm 0.99$	-1.00	+0.99	$0.24 \pm 0.99$
$k(\text{ptjmin})$	$-0.17 \pm 1.00$	-1.00	+1.00	$-0.17 \pm 0.99$
$k(\text{QCD})$	$0.12 \pm 0.84$	-0.84	+0.83	$0.12 \pm 0.83$
$k(\text{single top})$	$0.66 \pm 0.94$	-0.93	+0.93	$0.67 \pm 0.93$
$k(tt)$	$0.30 \pm 0.43$	-0.51	+0.43	$0.28 \pm 0.44$
$k(Z+\text{jets})$	$1.67 \pm 0.83$	-0.83	+0.84	$1.67 \pm 0.83$
Luminosity	-	-	-	$1.00 \pm 0.01$

Table 5.2: Fit results of the profile likelihood fit treating the background parameters as nuisance parameters. Fitted values for all parameters are given. The TMinuit Minos uncert. are listed apart from the Hesse uncertainties (separate column; fitted values only in the column containing the Hesse uncert.). Abbreviations follow the remarks in Section 5.1.4. For reasons of comparison, two fractional digits are shown.

elaborate than the former algorithm as non-linearities and parameter correlations are regarded. But because of negative diagonal elements in the error matrix, some Minos values are non-calculable which hints at underlying problems despite the convergence of the fit.

The Hesse uncertainties of both implementations are, in contempt of some smaller deviations, in the same order of magnitude. Table 5.2 also reveals that the Minos uncertainties are comparable to the Hesse ones reflecting the reliability of the less elaborate Hesse algorithm. The abnormal size of the negative  $E_T^{\text{miss}}$ +pile-up uncertainty larger than one, which can also be found in Table 5.2, is analysed in the upcoming sections.

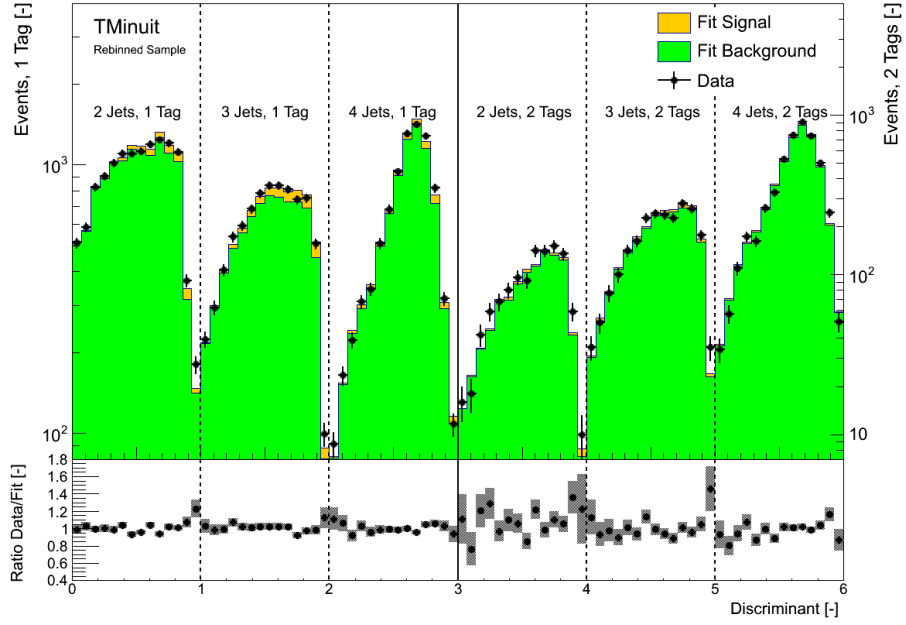
The signal cross-section with respect to the SM value can be calculated with the help of the fitted signal parameter for the TMinuit (TM) and the HistFactory (HF) fit pursuant to Eq. (5.1):

$$\frac{\sigma_{Wt,\text{TM}}}{\sigma_{Wt,\text{SM}}} = 1.40 \pm 0.56 \quad \text{and} \quad \frac{\sigma_{Wt,\text{HF}}}{\sigma_{Wt,\text{SM}}} = 1.39 \pm 0.55.$$

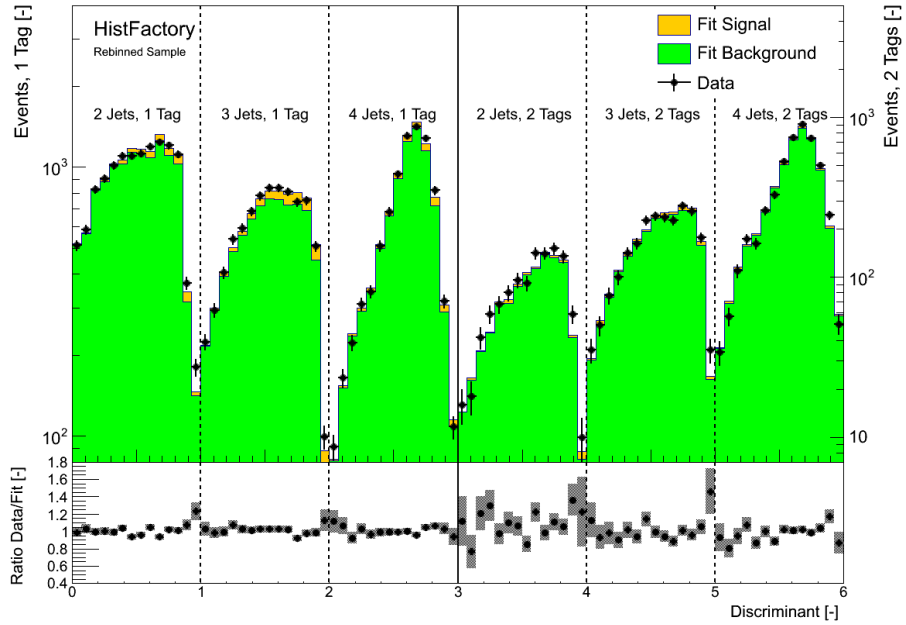
As stated above, means of error propagation are exploited to estimate the uncertainty on the cross-section ratio, based on the uncertainty of  $N_{Wt}$  and containing both the statistical and the systematic uncertainty. The total relative uncertainty of the two implementations amounts to 40% in both cases. The mismatch between the two techniques is about 1% (with regard to the TMinuit value) confirming a high consistency.

The distributions corresponding to the fit results of both implementations are displayed in Fig. 5.2a and 5.2b. The histograms based on the fit results containing signal and background events are plotted with the underlying data distribution. The combined plot is divided into six parts concerning the discriminant axis according to the six different channels which are used during the fit: the 2-(excl.), 3-(excl.) and 4-(incl.)-jet bin with one jet tagged as  $b$  jet or, alternatively, with at least two jets tagged as  $b$  jets. The ratio between the data histogram and the fitted signal+background contributions is determined for each single bin, shown at the bottom. As the ratios are roughly close to one, they demonstrate an adequate quality of both setups.

5 Measurement of the  $Wt$  Production in the Muon+Jets Channel



(a) TMinuit combined fit



(b) HistFactory combined fit

Figure 5.2: Data distributions of the likelihood discriminant and the fitted distributions obtained from the TMinuit (top) and the HistFactory (bottom) combined fit. The labelling allows for an appropriate allocation of the six bins, namely the 2-(excl.)-, 3-(excl.)- and 4-(incl.)-jet bin with one exclusive or two inclusive  $b$ -tags. The ratio of the data to the fit result is plotted at the bottom.

### 5.3.2 Scan of the Signal Parameter

This section deals with a description of a signal parameter scan which can be carried out to further examine and validate the fits presented in the last paragraph. This scan leads to a profile likelihood curve with respect to the signal  $N_{Wt}$ :  $-2 \ln L(N_{Wt})$ , where  $L$  signifies the corresponding profile likelihood value. The generation of such a plot requires the variation of the signal parameter from -1 to +2 in steps of 0.05 while  $N_{Wt}$  is fixed in each step and the fit is reperformed with all remaining fit parameters. The global minimum of the profile likelihood curve is set to zero afterwards. The resulting scans of the TMinuit and the HistFactory fit are depicted in Fig. 5.3a and 5.3b - including a quadratic polynomial with which the curve is approximated - and substantiate the position of the minimum found by the original fit whose results are listed in Table 5.2.

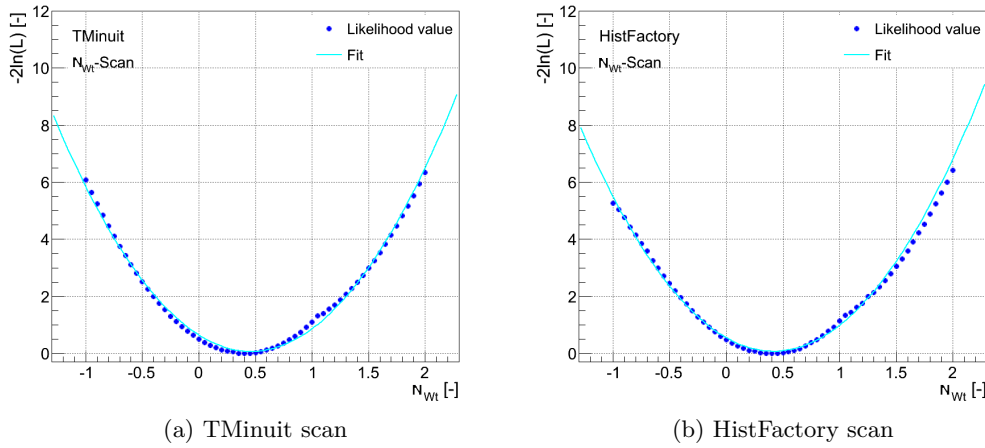


Figure 5.3: Profile likelihood scans for the signal parameter  $N_{Wt}$  resulting from (a) TMinuit or (b) HistFactory fits with varying  $N_{Wt}$ . The global minimum found by the minimisation process is set to zero, the significance can be obtained from a polynomial fit.

Eq. (5.1) allows for a determination of the significance in units of the standard deviation  $\sigma$  which is equal to the square root of the function value at  $N_{Wt} = -1$  which corresponds to the absence of any signal events:  $\sqrt{\Delta(-2 \ln L)}|_{-1}$ . These values are derived from the polynomial fit to the given likelihood values and the related uncertainty is estimated by means of error propagation. The results are:

$$\sqrt{\Delta(-2 \ln L_{\text{TM}})} = (2.42 \pm 0.01) \sigma \quad \text{and} \quad \sqrt{\Delta(-2 \ln L_{\text{HF}})} = (2.35 \pm 0.01) \sigma.$$

A significance of  $5\sigma$  is essential to eventually claim that the anticipated signal exists in fact, but the computed value clearly outvaluing zero hints at least at a potential  $Wt$  signal.

### 5.3.3 Scan of Nuisance Parameters

In order to investigate the applied nuisance parameters in more detail, a scan similar to the one presented in the last paragraph can be performed for the profiling parameters which improves the understanding of the obtained fit results and related uncertainties. But in contrast to the signal parameter scan, the fit is carried out only once and the likelihood value  $-2 \ln L$  is then computed on the basis of the fit results of all other fit parameters - except for the stepwise varied profiling parameter - and the fixed value of the latter parameter. A range from -2 to +2 in steps of 0.02 is examined for each nuisance parameter.

Fig. 5.4 exemplarily displays four of these nuisance parameter scans, all of them based on a TMinuit fit. Most parameter plots are characterised by a parabolic curve as, to give an example, the scans of  $k(\text{ISR})$  and  $k(\text{POWPY})$ , shown in Fig. 5.4a and 5.4b.

The piecewise linear interpolation may cause a discontinuity at  $k_j = 0$  resulting in a “hard” transition between the two areas with different signs of  $k_j$ . This is studied in more detail in the course of the  $W$  boson polarisation measurement (see Chapter 6). A discontinuity occurs in the nuisance parameter scans for EES (see Fig. 5.4c),  $Wb\bar{b}Wc\bar{c}\text{jet}$ ,  $Wc\text{jet}$ , JES,  $E_T^{\text{miss}}$ ,  $E_T^{\text{miss}}+\text{pile-up}$ , MS\_SCALE, MUS\_ID and MUS\_MS, following the labels introduced in Section 5.1.4.

Instead of another interpolation method, as introduced in Section 4.4, which is discussed thoroughly in the framework of the  $W$  boson polarisation measurement, a smoother interpolation is applied. This artificial smoothing is based on additional exponential factors appended to the interpolation term in order to modify the size of single addends. The discontinuities vanish without significantly changing the fit results. The resulting cross-section ratio diminishes to  $\sigma_{Wt,\text{smooth}}/\sigma_{Wt,\text{SM}} = 1.38 \pm 0.56$ , constituting a decrease of 1.5% compared to the original result. Therefore, considering the given uncertainty, which covers this deviation well, it is justified to rate the impact of this hard transition as negligible.

The scan of the parameter  $k(E_T^{\text{miss}}+\text{pile-up})$  has two minima. This shape, visible in Fig. 5.4d, is responsible for the values of the related Minos uncertainties given in Table 5.2. The asymmetric Minos algorithm uses the shape of the function with respect to the underlying parameter to calculate the larger negative uncertainty caused by the second minimum. The Hesse calculation leads to a smaller uncertainty based on the parabola around the found minimum. Deviations from a parabolic curve serve to explain other asymmetric Minos uncertainties although  $k(E_T^{\text{miss}}+\text{pile-up})$  is the only parameter whose curve reveals two minima.

The impact of such a shape with two minima on the fit result can be tested by setting the initial values to those which correspond to the two minima of the likelihood curve. The start values of  $k(E_T^{\text{miss}}+\text{pile-up})$  are thus set to +0.3 and -0.3. Both fits result in a value of  $k(E_T^{\text{miss}}+\text{pile-up}) \approx 0.3$ , the result already obtained from the original fit. Hence, a second minimum does not seem to affect the measurement in this particular case. A parameter showing such a behaviour can be removed from the fit nevertheless to minimise the risk of a potential bias, which is studied in Section 5.3.4.

In order to analyse the impact of single nuisance parameters on the fit results in

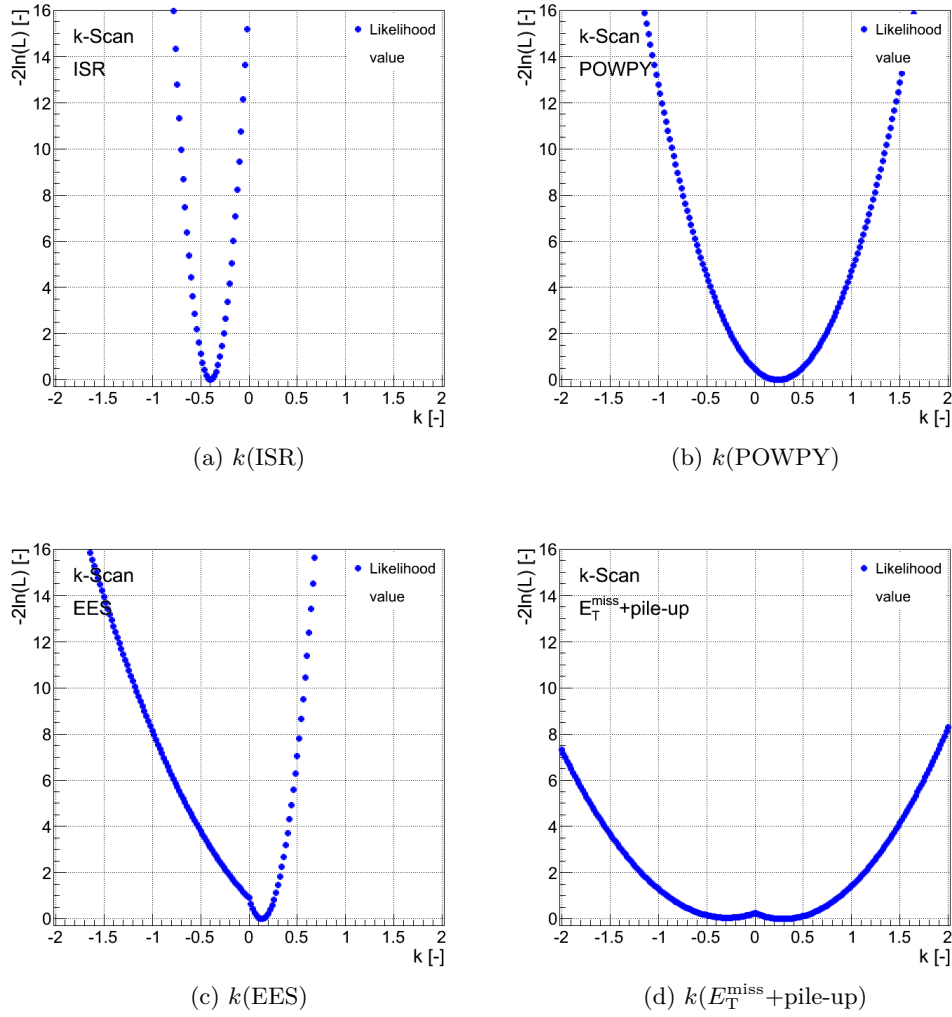


Figure 5.4: Exemplary likelihood scans for four nuisance parameters from TMinuit fits. The global minimum of the curve is set to zero. The captions contain the associated sources of systematic effects.

more depth, one specific nuisance parameter  $k_j$  can be fixed to 0 or  $\pm 1$  according to a  $\pm 1\sigma$ -variation. The fit is redone with the remaining parameters and the fixed parameter  $k_j$ .

The fitted value of  $N_{Wt}$  directly illustrates to which extent the  $Wt$  signal cross-section changes with a variation of the corresponding  $k_j$  over the  $\pm 1\sigma$ -range. Parameters with a narrow likelihood curve and thus small uncertainties influence the signal cross-section most since the variation of those parameters yield likelihood values larger than those at the minimum caused by the large slope of the parabolic curve. But these values are not favoured during a fit due to the large likelihood values far away from the accurate minimum. Consequently, the correct minimum is found which is reinforced by the sensitivity of the minimisation process to parameters whose likelihood curves reveal such a narrow curve like BTAG, JES, ISR or FSR.

In Fig. A.1 and Fig. A.2 in the appendix, several additional plots visualise the effect of parameters on the fitted distributions. Further histograms are plotted which are based on the best fit results excluding the value of the one profiling parameter which is set to  $\pm 1$  complying the  $\pm 1\sigma$ -range. The resulting fitted histograms are compared to the distributions belonging to the fit results of the original fit (see Section 5.3.1). Parameters having small likelihood curves affect the distributions most - which is in accordance with the former findings.

### 5.3.4 Profile Likelihood Fits with Fewer Nuisance Parameters

Several parameters have very little impact on the fit and the fitted values. These parameters are specified by a central value consistent with the initial value of zero and an uncertainty which is constrained by its prior term that amounts to  $\pm 1$ . Hence, a fit is not sensitive to the underlying systematic effect and the exclusion of the related profiling parameter from the fit does not seriously influence the result. In this analysis, this applies to nuisance parameters which describe systematic uncertainties caused by  $Wc$ ,  $Wb\bar{b}Wc\bar{c}$  and diboson processes. The  $Wt$  production cross-section can be computed after removing these parameters with Eq. (5.1) to  $\sigma_{Wt, TM, red1} / \sigma_{Wt, SM} = 1.40 \pm 0.56$  and to  $\sigma_{Wt, TM, red1} / \sigma_{Wt, SM} = 1.39 \pm 0.55$ . After rounding, this value is, as anticipated, equal to the one obtained from the original fit.

Apart from that, the parameters  $k(E_T^{\text{miss}} + \text{pile-up})$ ,  $k(\text{MUS\_MS})$  and  $k(\text{MS\_SCALE})$  can be removed from the fit to minimise the risk of distorting and biasing the result due to a second minimum (applies to  $k(E_T^{\text{miss}} + \text{pile-up})$ ) or a discontinuity at the peak (applies to both  $k(\text{MUS\_MS})$  and  $k(\text{MS\_SCALE})$ ). The following signal cross-section ratio can be derived:  $\sigma_{Wt, TM, red2} / \sigma_{Wt, SM} = 1.36 \pm 0.56$  and to  $\sigma_{Wt, HF, red2} / \sigma_{Wt, SM} = 1.38 \pm 0.56$  for both implementations. These values are still comparable to the fit comprising all parameters. The deviation is about 3% and 1%, respectively, with respect to the original fit, which are definitely covered by the fit uncertainties.

### 5.3.5 Additional Studies

Further studies and tests to examine the profile likelihood analysis in more detail are described in this section. Among other things, the influence on the fitted values caused by the application of binning methods and cuts on the input templates is analysed. To begin with, some MC checks of the fitting method are discussed.

**Checks of the Fitting Method** The nominal templates extracted from Monte Carlo simulation can be used as data input samples in place of the data distributions. The realisation of this test revealed that all nuisance parameters amounted to zero, all normalisation factors were found to be equal to one. The fitted values thus complied with the initial values set before the likelihood minimisation was carried out, confirming the accuracy of the implementations.

**Binning Methods** Rather than merging the events of each single jet bin template into 14 bins, several variations exist to bin the histograms. Table 5.3 lists the results of those binning tests. The number of histogram bins of each jet bin distribution  $N_{\text{bins},S}$ , the number of bins of the combined distribution  $N_{\text{bins,all}}$  involving all jet channels and being used for the fit, the signal production cross-section with its TMinuit uncertainties as well as the relative uncertainty on the cross-section is specified in the table.

$N_{\text{bins},S}$ [-]	$N_{\text{bins,all}}$ [-]	$\sigma_{Wt, \text{TM}}/\sigma_{Wt, \text{SM}}$ [-]	Rel. Unc.
7	42	$1.49 \pm 0.62$	42%
8	48	$1.46 \pm 0.61$	42%
10	60	$1.30 \pm 0.60$	46%
12	72	$1.27 \pm 0.59$	46%
13	78	$1.55 \pm 0.56$	36%
14	84	$1.40 \pm 0.56$	40%
15	90	$1.49 \pm 0.56$	38%
16	96	$1.53 \pm 0.54$	35%
17	102	$1.44 \pm 0.53$	37%
18	108	$1.52 \pm 0.53$	35%
20	120	$1.47 \pm 0.52$	35%

Table 5.3:  $Wt$  production cross-section results - including relative uncertainties - of the profile likelihood fit based on TMinuit for various kinds of histogram binning.

The binning method works as follows: If  $N_{\text{bins},S} \leq 10$ , the first  $N_{\text{bins},S} - 1$  bins each include the entries of a range of  $\Delta y_{\mathcal{L}} = 0.1$ , the remaining events are put together into the last bin. If  $10 < N_{\text{bins},S} \leq 20$ , the first  $N_{\text{bins},S} - 1$  bins each cover a discriminant range of  $\Delta y_{\mathcal{L}} = 0.05$ , and, as before, the remaining events are pooled into the remaining bin. This is done due to the fact that only a few events possess such large discriminant values. Only if  $N_{\text{bins},S} = 10$  or  $N_{\text{bins},S} = 20$ , the last bin comprises the same discriminant range  $\Delta y_{\mathcal{L}}$  compared to all other bins.

Because of possible MC fluctuations or problems with non-convergencies, tests with  $N_{\text{bins},S} > 20$  are not considered, as explained in Section 5.2.3.

An increase in the number of template bins lead to absolute as well as the relative uncertainties which tend to decrease. Moreover, cross-section fluctuations with a varying number of bins occur. The uncertainty indicates that with a lessening number of histogram bins too much information concerning the shape of the distribution is lost. Taking into consideration that possible MC fluctuations will increase with a rising number of bins which may bias the result as well,  $N_{\text{bins},S} = 14$  constitutes an adequate compromise between possibly growing MC fluctuations and a potential loss of information. The cross-section ratio fluctuates around the former fitted value of  $\sigma_{Wt,\text{TM}}/\sigma_{Wt,\text{SM}} = 1.40 \pm 0.56$  belonging to  $N_{\text{bins},S} = 14$ , calculated in Section 5.3.1, by about +11% and -9%. The fluctuations are hence well covered by the fit uncertainties.

**Application of Cuts** Another test performed in the framework of this analysis is the application of cuts on the templates which means that only events with a discriminant value surpassing a specific cut value  $y_{\mathcal{L},\text{cut}}$  are used for the fit whereas events  $i$  with  $y_{\mathcal{L}}(i) < y_{\mathcal{L},\text{cut}}$  are cut away and thus rejected. The input distributions used during the minimisation process are composed of the remaining fractions of events. For reasons of consistency, cut tests presented here are based on input histograms which originally had 14 bins,  $N_{\text{bins},S} = 14$ . The results are listed in Table 5.4. A number of cut values lying in the range  $0.05 \leq y_{\mathcal{L},\text{cut}} \leq 0.30$  have been chosen. The resulting  $Wt$  cross-sections with absolute as well as related relative uncertainties are shown.

Cut Value $y_{\mathcal{L},\text{cut}}$ [-]	$\sigma_{Wt,\text{TM}}/\sigma_{Wt,\text{SM}}$ [-]	Rel. Unc.
0.00	$1.40 \pm 0.56$	40%
0.05	$1.36 \pm 0.57$	42%
0.10	$1.58 \pm 0.59$	37%
0.15	$1.46 \pm 0.59$	40%
0.20	$1.73 \pm 0.63$	36%
0.25	$2.39 \pm 0.66$	28%
0.30	$2.35 \pm 0.68$	29%

Table 5.4:  $Wt$  production cross-section ratios - including relative uncertainties - of the profile likelihood fit based on TMinuit with  $N_{\text{bins},S} = 14$  depending on cut values.

Depending on the chosen cut value, the resulting cross-section is significantly affected and shifted to higher numbers of signal events; large cut values result in cross-sections twice as large as the original fit result. Applying cuts is equivalent to a loss of information as parts of the discriminant distributions are omitted so that the relative uncertainty is assumed to rise with increasing absolute uncertainty. However, the opposite effect is observed owing to the large signal rates. These are potentially due to the disregard of information that normally constrains the background because of the cut. This cut is responsible for a rejection of events in

the part of the distributions with small discriminant values mostly populated by background events. There may, though, also be a systematic effect inducing this growth with rising cut values. As a consequence, additional studies, which allow for a conclusion whether the use of cuts is justified or not, are required.

**Input Templates Based on Different Scenarios** In section 5.1.5, the choice of the scenario on which the input templates are based could be substantiated with the help of pseudo-data tests. Furthermore, fits have been performed based on other templates generated with the remaining different scenarios, as displayed in Table 5.1. The results are given in Table 5.5, the gained cross-section ratios based on these different input scenarios are quite compatible with each other and reveal that other scenarios seem to provide rather adequate results as well but also emphasise the quality of the chosen scenario 6.

The fluctuations between the resulting cross-sections gathered from different scenarios amount to +9% and -11% with regard to the original fit using scenario 6 but are covered well by the given absolute uncertainties.

Scenario	$\sigma_{Wt, \text{TM}}/\sigma_{Wt, \text{SM}} [-]$	Rel. Unc.
1	$1.52 \pm 0.61$	40%
2	$1.52 \pm 0.54$	36%
3	$1.46 \pm 0.54$	37%
4	$1.25 \pm 0.63$	50%
5	$1.39 \pm 0.55$	40%
6	$1.40 \pm 0.56$	40%
7	$1.42 \pm 0.56$	39%

Table 5.5:  $Wt$  production cross-section results - including relative uncertainties - of the profile likelihood fit based on TMinuit with  $N_{\text{bins}, S} = 14$  for several possible scenarios of input templates pursuant to Table 5.1.

### 5.3.6 Pseudo-Experiments

Pseudo-experiments (PEs) are applied to appropriately assess and validate the quality of a profile likelihood fit. They are especially sensitive to potential deviations from the calculated likelihood curve significantly away from the found minimum ( $3\sigma$  and larger) and thus ensure a correct description of the likelihood curve resulting from the minimisation process. In this analysis, pseudo-experiments are studied with respect to the signal parameter  $N_{Wt}$ . More elaborate and extensive tests with pseudo-experiments are applied in the course of the  $W$  boson polarisation measurement as explained in Chapter 6.

With the help of the HistFactory tool, 10,000 pseudo-experiments have been carried out in total, using again nuisance parameters to fit the background contributions. The implementation of pseudo-experiments works as follows: For each pseudo-experiment, new values for all nuisance parameters are generated. The uncertainties on these values equal the uncertainties on the parameters obtained from

the HistFactory profile likelihood fit done before. Solely the signal parameter  $N_{Wt}$  is fixed to its fitted value of  $N_{Wt} = 0.39$ . Afterwards, new observables based on the new set of nuisance parameters are generated and, as the final step, the profile likelihood fit is reperformed with the new generated parameters and observables constituting a pseudo-data set.

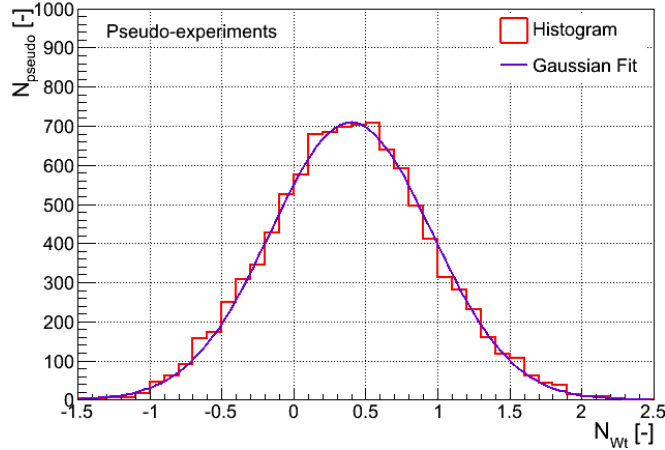


Figure 5.5: 10,000 PEs for the signal parameter  $N_{Wt}$  with an associated Gaussian fit.

The outcome of the pseudo-experiments are 10,000 values for  $\alpha_{Wt}$  which are plotted in a histogram displayed in Fig. 5.5. The distribution reveals a Gaussian shape, as anticipated. This is emphasised by a Gaussian fit. Based on the mean value of the distribution and the corresponding width, the  $Wt$  production cross-section can be evaluated with the help of Eq. (5.1) to:

$$\frac{\sigma_{Wt,pseudo}}{\sigma_{Wt,SM}} = 1.40 \pm 0.56.$$

The parameter uncertainty is estimated by means of error propagation, consistent with the former computations. The difference between this cross-section to the one obtained from both the TMinuit and the HistFactory fit is, as expected, negligible. To conclude, both fitting techniques seem to work smoothly, no remarkable deviations from the original fit can be found and the calculation of the uncertainties can be regarded as accurate.

These studies based on pseudo-experiments can be further validated. A similar test that rests on a no-signal hypothesis (which means that  $N_{Wt}$  amounts to -1) is performed, which then serves to evaluate the probability that the observed signal is only composed of background events. The  $p_B$ -value which expresses this probability amounts to approximately 0.88%. This small percentage further suggests the existence of the  $Wt$  signal. The translation into a significance in units of standard deviations yields approximately  $2.62\sigma$ , similar to the values calculated in Section 5.3.2.

# 6 Measurement of the $W$ Boson Polarisation in the Muon+Jets Channel

The following chapter presents a measurement of the  $W$  boson polarisation, i.e. the  $W$  boson helicity fractions, in the muon+jets channel. Again, a profile likelihood fit plays an essential role in the context of the analysis. The previous chapter focused on the setup of a profile likelihood fit and tests with different input configurations to show how such a fit can be applied. In contrast, this chapter concentrates on the validation of the fitting method and on testing different interpolation algorithms to improve the understanding of the fitting method itself and its numerous features which often constitutes a demanding task. In this context, an overview of a more encompassing analysis which serves to measure the  $W$  boson helicity fractions is given. Some additional studies to cross-check the fit results are addressed in App. C. First, some necessary information concerning the fundamentals of the measurement are outlined. As already explained in the last chapter, these topics are relevant for the underlying analysis but, however, cannot be discussed in very detail in order not to exceed the scope of this thesis. A lot of facts are similar to the analysis in Chapter 5 but are mentioned here again for reasons of completeness and comprehensibility. The section is followed by an introduction of the profile likelihood fit as used for this measurement while the subsequent part deals with a presentation of the obtained results, regarding both the various tests of the profile likelihood fit and the  $W$  boson helicity measurement itself.

## 6.1 $W$ Boson Polarisation: Fundamentals of the Measurement

This section covers main aspects of the  $W$  boson polarisation measurement with respect to Monte Carlo samples, the object and event selection, the event reconstruction and systematic uncertainties. The analysis is based on collision data taken at a centre-of-mass energy of  $\sqrt{s} = 7$  TeV collected with the ATLAS detector in 2011. The corresponding integrated luminosity is about  $\int \mathcal{L} dt = 4.7 \text{ fb}^{-1}$  with an uncertainty that amounts to 1.8% [105].

### 6.1.1 Simulated Event Samples

The Monte Carlo samples used for this analysis are provided by the MC11c production campaign of the ATLAS Production Group [106]. This campaign serves to produce MC samples for data collected in 2011 corresponding to the data reprocessing of that year and associated with an LHC bunch spacing of 50 ns. It applies new

MC generator tunes and new GEANT4 hits [76] and is based on PYTHIA6 pile-up [88]. To be more exact, PYTHIA6 minimum bias events are used for simulating pile-up considering the assumption of variable pile-up rates.

The MC production follows the ATLAS-wide conventions. The top quark reference cross-sections are computed using the MSTW 2008 NLO PDF set [107] based on a top quark mass of  $m_t = 172.5 \text{ GeV}/c^2$ . The  $t\bar{t}$  cross-section is normalised to a reference value of about  $166.8_{-17.8}^{+16.5} \text{ pb}$  [29] originating from approximate NNLO calculations using HATHOR 1.2 [30]. The computation of the resulting uncertainty from this cross-section evaluation is based on the quadratic sum of both the scale and the PDF uncertainties. The scale uncertainty is calculated with the help of independent variations of renormalisation and factorisation scales. The uncertainty on  $\alpha_s$  is considered as well.

The central  $t\bar{t}$  and single top samples ( $Wt$  and  $s$ -channel production) are generated with the MC@NLO generator [78] using the CTEQ6.6 parton distribution functions [82]. The events are hadronised with the HERWIG shower model [84] and interfaced to JIMMY [86] which is employed for the underlying event model. As modelling insufficiencies due to the HERWIG setup arise, single top events from  $t$ -channel production are generated using AcerMC [89]. In order to produce  $t\bar{t}$  samples for the templates which are then used for the fits containing lepton+jets and dileptonic events, the PROTOS generator [108, 109] is employed. This LO generator allows for the construction of separate templates for top quark events with left-handed, right-handed and longitudinally polarised  $W$  bosons.

$W$ +jets and  $Z$ +jets events are generated with ALPGEN [81], the underlying event is added using JIMMY. The  $W$ +jets cross-sections are normalised to NNLO, the  $Z$ +jets samples include the full Drell-Yan contribution from the process  $\gamma^* \rightarrow \ell\ell$ , considering the  $Z/\gamma^*$  interference. HERWIG is used to generate diboson events, namely  $WW$ ,  $WZ$  and  $ZZ$ , while all QCD multijet events are estimated with the help of data-driven methods. The largest contribution of the diboson background events to the top production processes is usually caused by events containing more high- $p_T$  jets in the final state than final state partons in the lowest multiplicity hard process matrix element occur.

### 6.1.2 Definition of Physics Objects

Similar to the  $Wt$  production rate measurement, the reconstruction of events requires the use of reconstructed muons, electrons, jets and missing transverse energy. The description is compliant with [29].

#### Muons

The identification of muons in candidate events is carried out at trigger level as well as offline. Corresponding trigger and top-specific identification scale factors for muons need to be determined. Offline muons pass through further selection steps to reject background events. The specific selection criteria and the results of related efficiency studies are briefly discussed in the following.

At trigger level, muon events require a first level (L1) muon trigger chamber track. Regions-of-Interest in the muon system with a transverse momentum of at least

10 GeV are chosen. The Regions-of-Interests of the L2 and EF trigger are combined to a `Muid` muon track on the condition that these RoIs are closer than  $\Delta R = 0.15$ . Regarding the offline muon selection, in particular combined muons included in the `MuidMuonCollection` are taken into account. Additional cuts, as listed below, ensure that only muons not originating from heavy and light flavour decays are selected:

At first, the muon candidate needs to satisfy the recommendations of the Muon Combined Performance Group (MCP). The muon transverse momentum must exceed a  $p_T$  of 20 GeV, and the muon candidate must be within the pseudorapidity region  $|\eta| < 2.5$ , which is equivalent to the detector acceptance region. Moreover, additional hit requirements and isolation criteria have to be fulfilled. For example, the following inequations need to hold:  $p_T^{0.3} < 2.5$  GeV,  $E_T^{0.2} < 4$  GeV and  $\Delta R(\mu, j) > 0.4$  with a jet  $j$ . Here, only jets  $j$  with  $p_T > 25$  GeV and a jet vertex fraction (JVF) which is larger than 0.75 are considered.  $E_T^{0.2}$  is the sum of the transverse energy in a cone of  $\Delta R = 0.2$  around the muon, while  $p_T^{0.3}$  is the sum of transverse momenta of ID tracks found in a cone of  $\Delta R = 0.3$  around the muon candidate.

Based on these cuts, the trigger efficiency and the muon scale factors can be estimated. The trigger efficiency is defined with regard to the number of offline reconstructed muons fulfilling the selection criteria mentioned above. A systematic bias is caused by a dimuon invariant mass cut, the trigger matching cut and the effect of isolating the tag.

The pure reconstruction efficiency for `Muid` combined muons is calculated for the muon offline identification. The muon-related background contribution in data is determined separately and then subtracted.

## Electrons

$Z \rightarrow ee$  and  $W \rightarrow e\nu$  events are used to calculate the trigger efficiency and the data/MC efficiency ratio. The minimal allowed transverse electron energy amounts to 25 GeV at trigger level.

To successfully reconstruct offline electron candidates, various quality requirements are imposed: Certain Inner Detector requirements need to be fulfilled and the candidate must have  $E_T > 25$  GeV with a transverse energy derived from the calorimeter cluster energy and from the direction of the electron track. Electron candidates from the barrel-endcap overlap region of the calorimeter with  $1.37 < \eta_{cl} < 1.52$  are removed, the maximally allowed value is  $|\eta_{cl}| = 2.47$ . A matching with a trigger object is required, jets having an axis with a distance smaller than  $\Delta R = 0.2$  to the electron are removed. Isolation criteria are essential to exclude further background events, the sources are the ones already mentioned in the context of the  $Wt$  cross-section measurement: photon conversion, fake electrons and electrons coming from heavy flavour processes. Certain criteria exist to isolate electron candidates from jet activity which significantly reduces the above listed background sources. Electron reconstruction efficiencies and corresponding scale factors need to be determined just as the electron energy scale and resolution, which are evaluated with the help of  $Z \rightarrow ee$  events.

## Jet Selection

The reconstruction of jets is based on the anti- $k_t$  algorithm [92, 93], using a width parameter  $\Delta R$  of 0.4, similar to the definition in Chapter 5.1.2. To cover the energy deposit coming from electrons or photons, the algorithm exploits topological clusters in the EM calorimeter. To retrieve the hadronic energy scale after jets traversed the corresponding calorimeters, MC based correction factors for  $p_T$  and  $|\eta|$  are applied for a calibration of these jets. Jets used for the later analyses are calibrated at the electromagnetic and the jet energy scale.

For a proper reconstruction of jets, certain criteria are used which comprises a step to remove electron-jet duplicates or, for example, the jet cleaning. Acceptance cuts on the  $|\eta|$ -acceptance and the missing transverse energy as well as a muon isolation criterion are applied. Apart from that, a cut on the jet vertex fraction is used:  $|JVF| > 0.75$ . If a bad jet occurs, defined as a jet not related to in-time real deposits in the calorimeter system, the corresponding event is vetoed.

## $E_T^{\text{miss}}$ and Related Systematic Uncertainties

The missing transverse energy  $E_T^{\text{miss}}$  as a measure of the non-detectable and consequently escaping neutrinos, is computed with the help of topological clusters which are calibrated at the EM scale. The corresponding correction depends on the energy scale of the underlying object. The contributions of different particles need to be considered for a determination of  $E_T^{\text{miss}}$ :

Muons are added if they are mainly described by the information obtained from the muon spectrometer because of not being primarily measured in the calorimeter system. Topological clusters which are allocated to electrons and jets with high transverse or low transverse momentum - in the latter case, they are denoted as soft jets (**SoftJet**) -, are included. An additional term accounts for the remaining clusters having no high- $p_T$  objects, a so-called **CellOut** term. The missing transverse energy can then be calculated:

$$E_T^{\text{miss}} = \sqrt{(E_x^{\text{miss}})^2 + (E_y^{\text{miss}})^2}, \quad (6.1)$$

with  $E_{x,y}^{\text{miss}} = E_{x,y}^{\text{Muon}} + E_{x,y}^{\text{Electrons}} + E_{x,y}^{\text{Jets}} + E_{x,y}^{\text{SoftJets}} + E_{x,y}^{\text{CellOut}}$ .

To calculate all the different contributions of Eq. (6.1) numerous requirements and criteria need to be fulfilled in each case.

The scale and resolution of the different objects or the description of pile-up events constitute dominant  $E_T^{\text{miss}}$ -related systematic uncertainties. All objects that are mentioned in Eq. (6.1) possess an uncertainty which corresponds to the scale and resolution of the energy and the transverse momentum of this object. Particular tools are used to estimate this uncertainty. In many cases, a 100% correlation between then uncertainty on an object and  $E_T^{\text{miss}}$  is adopted. Pile-up effects arising in jet, **SoftJet** and **CellOut** terms need to be considered as well.

Another source of systematic uncertainty is due to the impact of hardware failures. The loss of front end boards in 2011 caused a hole in the calorimeter coverage which was partly recovered later. This loss is also considered in the MC simulation.

### b-Tagging

In this analysis, the identification of jets containing  $b$  quarks, the  $b$ -tagging, is realised with the ATLAS  $b$ -tagger *MV1*, based on a neural network which combines the information from three high-performance taggers: *IP3D*, *SV1* and *JetFitter*. All three tagging algorithms rest on a likelihood ratio technique which is based on the idea of comparing input variables to smoothed normalised distributions gained from MC simulations for both the  $b$  and light jet hypotheses. The *IP3D* tagger exploits transverse as well as longitudinal impact parameter significances, where the impact parameter constitutes a parameter related to  $b$ -tagging algorithms. The *SV1* tagger is based on the reconstruction of a secondary vertex formed by the  $B$  hadron decay products. Finally, the *JetFitter* tagger employs a Kalman filter to find a common line which includes the position of the primary vertex and of the  $b$ - and  $c$ -vertices. The weight for the *MV1* tagger is then computed based on the jet weights for the three above listed taggers and the  $p_T$  and  $|\eta|$  of the jet. The tagger is used at the 70% efficiency working point (in simulated  $t\bar{t}$  events) which corresponds to a weight of 0.602.

#### 6.1.3 $W$ +jets Normalisation

Since the entire normalisation and the heavy flavour composition are not precisely known in Monte Carlo, a data-driven method is applied to estimate the normalisation of  $W$ +jets events. The so-called charge asymmetry method is exploited to evaluate the overall normalisation. This method is based on the use of the asymmetrical cross-sections for positively and negatively charged leptons which originate from the  $W$  boson decays as explained in Section 5.1.5. The estimation of the  $W$ +jets normalisation as well as the necessary calculation of the flavour scale factors is carried out in all jet bins for both tagged and pretagged events. Further information can be found in [29].

#### 6.1.4 Fake Lepton Estimates

Top quark events in the lepton+jets channel are characterised by leptons having a large transverse momentum in the final state. Although these leptons need to fulfil the various event selection criteria, a certain number of misidentified leptons, referred to as fake leptons are included in the selected sample, as already shown in Section 5.1.5. Due to the relevance of this background for the analysis presented here, the background estimation is outlined more extensively.

Fake lepton events are caused by semileptonic  $b$  jet decays, weakly decaying states with a long lifetime like  $\pi^\pm$  or  $K$  mesons,  $\pi^0$  showers reconstructed as an electron, reconstruction of electrons from conversions or direct photons. These different sorts of background sources significantly depend on the shape of the detector and the fragmentation processes.

The modelling of fake lepton events, i.e. the QCD background, is thus complicated so that data-driven methods are applied for an adequate evaluation of the fake lepton rate [29]. For the estimate, a matrix method depending on the chosen top quark decay channel is used.

The matrix method is based on events which satisfy either the so-called loose or the tight lepton selection requirements. In the muon+jets channel used in this analysis, the tight selection conforms with the common event selection presented in Section 6.1.5 while the loose selection is based on the same criteria excluding the muon calorimeter and track isolation requirements. The number of loose events contains real and fake leptons:  $N^{\text{loose}} = N_{\text{real}}^{\text{loose}} + N_{\text{fake}}^{\text{loose}}$ . With the fake and the real efficiency,  $\varepsilon_{\text{fake}}$  and  $\varepsilon_{\text{real}}$ , defined as the ratio of either fake or real leptons classified as tight to the corresponding ones classified as loose, the number of tight electrons can be written as:  $N^{\text{tight}} = \varepsilon_{\text{real}} N_{\text{real}}^{\text{loose}} + \varepsilon_{\text{fake}} N_{\text{fake}}^{\text{loose}}$ . The number of fake leptons which also pass the tight selection criteria can then be calculated:

$$N_{\text{fake}}^{\text{tight}} = \frac{\varepsilon_{\text{fake}}}{\varepsilon_{\text{real}} - \varepsilon_{\text{fake}}} \cdot (N^{\text{loose}} \varepsilon_{\text{real}} - N^{\text{tight}}).$$

The relative efficiencies  $\varepsilon_{\text{fake}}$  and  $\varepsilon_{\text{real}}$  are estimated based on data. For this purpose, control samples enriched in real or fake muons are used. These control samples have to be selected in a way that they are kinematically characteristic of the signal region. This allows for the desired application of the measured efficiency, which is related to the control region, to the signal region.

### 6.1.5 Event Selection

The event selection for the considered muon+jets channel, is discussed with all its requirements and criteria in this paragraph. The different selection criteria are consistent with the common top group recommendations.

#### Muon+Jets Topology

Events have to fulfil a trigger requirement: The chosen Event Filter trigger needs to be passed in both data and MC. Since different triggers have been used for different periods of data-taking, MC samples have to be reweighted accordingly. An event is required to have a well-defined primary vertex to which more than four tracks are associated.

Exactly one good muon with  $p_{\text{T}} > 20$  GeV must be contained in the event. It has to be matched to the trigger object that recorded the event.

In order to remove muons coming from a semileptonic heavy flavour decay (being inside a jet), an overlap removal is implemented as well. The muon is removed from the event if it overlaps with a jet having a  $p_{\text{T}}$  that is larger than 20 GeV within  $\Delta R < 0.4$ . The event is also rejected if an electron and a muon share a track of the Inner Detector.

Furthermore, the event is required to include at least four jets with a  $p_{\text{T}}$  exceeding 25 GeV. These jets are corrected to the EM+JES scale. Another requirement is imposed on the missing transverse energy in the muon channel:  $E_{\text{T}}^{\text{miss}} > 20$  GeV. Besides, a triangular cut with the transverse mass of the  $W$  boson  $m_{\text{T}}(W)$  is chosen in the muon+jets channel according to:  $m_{\text{T}}(W) + E_{\text{T}}^{\text{miss}} > 60$  GeV. This cut helps to reject QCD multijet events since those tend to have a low missing transverse energy and a low transverse  $W$  boson mass compared to the signal.

Events with LAr noise bursts are disregarded as well. Several criteria are added to handle the lost front end boards in the liquid argon calorimeter.

Finally, a specific *b*-tagging requirement is applied: At least one of the jets contained in the event needs to be tagged with the employed *MV1* algorithm with a working point cut at 0.602 which corresponds to an efficiency of 70%.

### Results of the Event Selection

After the selection of events that fulfil all requirements and corresponding criteria listed above, the expected number of simulated MC events and the number of observed data events can be determined. The calculation also takes scale factors according to trigger, identification, reconstruction and *b*-tagging efficiencies into account. A reweighting step due to pile-up is performed as well. This pile-up reweighting is essential to rescale the Monte Carlo simulation in order to match the measured pile-up distribution.

The numbers of expected and observed events together with the related estimated uncertainties are shown in Table 6.1. The listed uncertainties include the statistical uncertainty as well as the major systematic uncertainties involving those which are due to the jet energy scale and resolution, due to the jet reconstruction efficiency, due to the lepton energy scale and resolution and due to scale factors. Additionally, *b*-tagging-related uncertainties are included as well.

Process	Selected Events
$t\bar{t}$	$26550 \pm 3822$
Single top	$1968 \pm 334$
QCD multijets	$1777 \pm 362$
$W$ +jets	$4465 \pm 1591$
$Z$ +jets	$479 \pm 272$
Diboson	$71 \pm 47$
Total prediction	$35310 \pm 4178$
Data	37919

Table 6.1: Event yields in the muon+jets channel. The given numbers are explained in more detail in the text.

In Fig. 6.1 and Fig. 6.2 the comparison between data and MC after event selection is shown for different lepton and jet quantities explained in the captions. All illustrations reflect that the expected contributions agree with the measured data to a large extent.

#### 6.1.6 Event Reconstruction

In a next step, the full reconstruction of selected events in the muon+jets channel has to be done. For this purpose, a kinematic likelihood provided by the *KL Fitter* tool is employed [110]. Solely the four leading jets in  $p_T$  enter the fit. Breit-Wigner terms for both the  $W$  boson and the top quark are included in the likelihood. They also depend on the masses  $m$  and the decay widths  $\Gamma$  of these particles.

## 6 Measurement of the $W$ Boson Polarisation in the Muon+Jets Channel

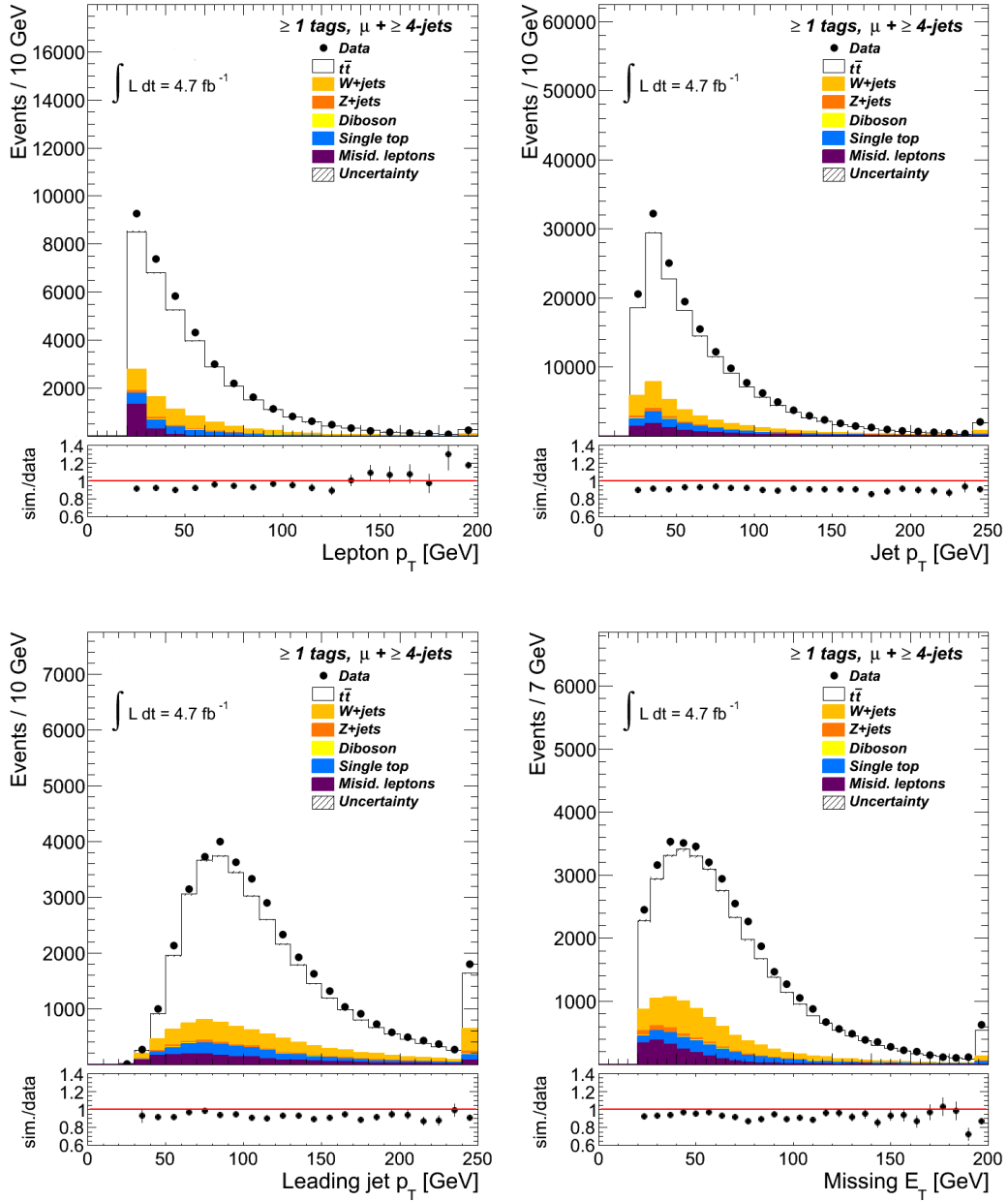


Figure 6.1: Comparison between data and simulated events after the event selection for the 4-incl.-jet bin with at least 1  $b$ -tag. The four plots show the distribution of the transverse momentum  $p_T$  of the reconstructed leptons (top left), of the reconstructed jets (top right) and of the leading jet (bottom left) as well as the distribution of missing transverse energy (bottom right). The different MC related contributions are shown, the hatched bands mark the statistical uncertainty. At the bottom, the ratio between simulated events and data is displayed.

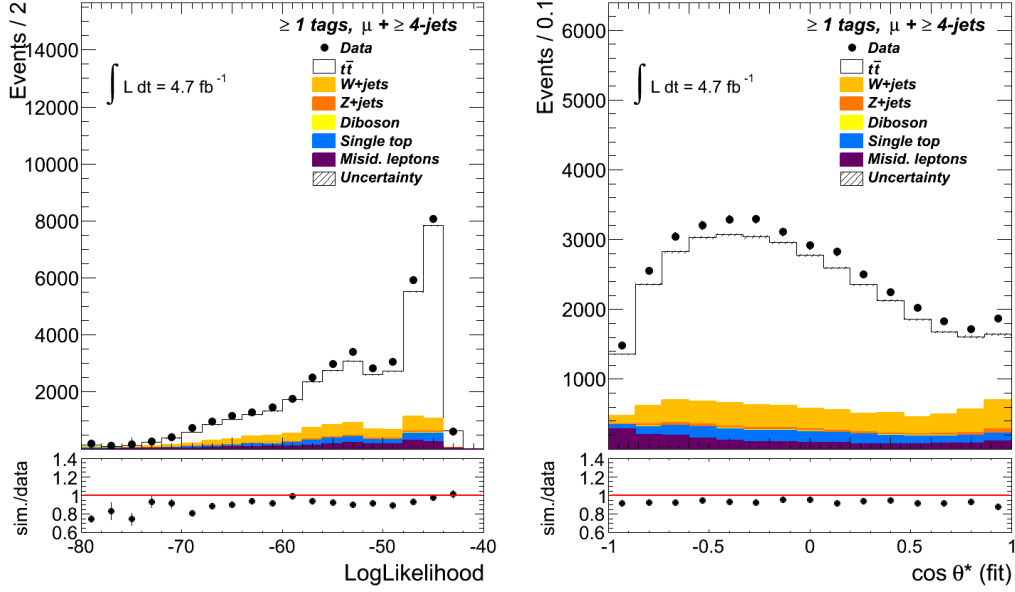


Figure 6.2: Comparison between data and simulated events after the event selection for the 4-incl.-jet bin with at least 1  $b$ -tag. The two plots show the distribution of the logarithmic likelihood (left) and of the fitted  $\cos \theta^*$  (right). “Fit” refers to the use of fitted lepton and jet four-vectors obtained from the KLFFitter (results already gained from the event reconstruction, see Chapter 6.1.6). The different MC-related contributions are shown, hatched bands mark the statistical uncertainty. At the bottom, the ratio between simulated events and data is displayed.

The parameters for the  $W$  boson are fixed to  $m_W = 80.4 \text{ GeV}$  and  $\Gamma_W = 2.1 \text{ GeV}$ , the ones which correspond to the top quark are fixed to  $m_t = 172.5 \text{ GeV}$  and  $\Gamma_t = 1.5 \text{ GeV}$ .

Apart from that, the likelihood also contains transfer functions that relate the measured jets and leptons to the partonic objects with mapping functions that are parametrised with double Gaussian terms. In the following, events are used where all measured particles are matched with the corresponding objects at parton level. The transfer functions are then obtained from these entirely matched events by using an MC@NLO sample and which are parametrised in different pseudorapidity and energy regions. The identification of one or both  $b$  jets is feasible by exploiting  $b$ -tagging algorithms. A further term in the likelihood is the  $b$ -tagging efficiency and the rejection rate of the employed algorithms at the chosen working point  $w$  (see Section 6.1.5).

The likelihood is then computed for all possible jet-parton assignments. The one with the largest probability is chosen and used to reconstruct the final angular  $\cos \theta^*$ -distributions. These are different for the three  $W$  boson helicity states and are thus used for the  $W$  boson polarisation measurements.

### 6.1.7 Systematic Uncertainties

Before the  $W$  boson polarisation measurement is addressed, the arising systematic uncertainties are introduced in the following paragraphs. To decide which of these systematics enters the profile likelihood fit and is adjusted via profile parameters, further tests are essential, presented in Section 6.3.2. Most of the systematic effects have also been considered for the  $Wt$  cross-section measurement and have been treated similarly (see Chapter 5.1.4). The corresponding systematic effects are discussed briefly just to give a coherent and complete overview.

Some systematic effects which cannot be profiled are covered more extensively in Chapter 6.3.5.

**Muon Energy Scale and Resolution** To estimate the impact of the muon energy scale, the  $p_T$  of the muons in MC is scaled up and down by  $\pm 1\sigma$ . The rescaled samples are then compared to the nominal ones.

Smearing the muon distributions in data, which affects the event selection and reconstruction, allows for estimating the influence of the muon energy resolution, similar to the description in Chapter 5.1.4. All the corresponding uncertainties are at a level of 1%.

Electron-related uncertainties are too small to induce a measurable effect and thus not evaluated.

**Jet Energy Scale and Resolution** The size of the jet energy scale (JES) uncertainty is dependent on the transverse momentum and the pseudorapidity of the reconstructed jet. To estimate the uncertainty, the tool `MultijetJESUncertaintyProvider` is used, the calculation mainly follows the explanation in Chapter 5.1.4. The uncertainty, with its dependence on  $p_T$  and  $\eta$  of the jet, varies between 2.5% and 8% in the central and between 3% and 14% in the forward detector region. The pile-up uncertainty (5% in the central, 7% in the forward region) is contained in this evaluation. Further contributions take the top quark multijet environment into account, including the flavour composition as well as the close-by jet uncertainties which are due to jets produced with another jet nearby in the multijet environment. The corresponding uncertainty due to  $b$  jets, the  $b$ -JES, which amounts to 2.5%, is also included in the calculation; the uncertainties are added in quadrature.

The systematic effect caused by the jet energy resolution (JER) is propagated to Monte Carlo by smearing the transverse momentum of the underlying jet in data, consistent with the procedure in Section 5.1.4. Dijet events are used, an uncertainty of 10% is assigned.

**Jet Reconstruction Efficiency** The jet reconstruction efficiency (JEFF) calculation is based on randomly dropping jets from events in MC using minimum bias and QCD dijet events. The associated uncertainty amounts to 2%, based on the agreement between efficiencies which are measured in both MC simulation and data.

**Scale Factors** In order to enhance the data/MC agreement, specific scale factors can be introduced. Based on  $Z \rightarrow \ell\ell$  and  $W \rightarrow e\nu$  decays, those factors can be

derived, depending on the lepton kinematics involving trigger, object reconstruction as well as identification efficiencies.

**b-Tagging/Mistagging Scale Factors** Also uncertainties caused by the applied  $b$ -tagging scale factors need to be considered, comparable to the treatment of the known trigger, identification and reconstruction efficiencies. A mistagging scale factor is used as well. The related uncertainties are added in quadrature afterwards. The uncertainties lie in a range of 9%-16% ( $b$ -tagging) and of 12%-45%.

**QCD Background** Another uncertainty which is accounted for is due to QCD background, i.e. fake lepton events. The shape uncertainty for the fake lepton evaluation is calculated with the help of a matrix method, as already done for the  $Wt$  cross-section analysis and explained in Subchapter 6.1.4. To be more precise, two different methods with a different QCD shape are used.

**W+jets Background** By employing the underlying ALPGEN samples, the shape uncertainty of the  $W$ +jets background can be computed. It is based on the variation of two ALPGEN parameters, called `ptjmin` and `iqopt`, similar to the description in Chapter 5.1.4.

**Colour Reconnection** Colour reconnection (CR) can be defined as colour rearrangement between partons. To estimate the effect due to colour reconnection, four  $t\bar{t}$  samples based on two different MC tunings with and without colour reconnection are applied.

**Missing Transverse Energy** The uncertainty related to the missing transverse energy is dominated by the energy resolution and scale correction uncertainties of both leptons and jets. Uncertainties which have to be added in this context arise from calorimeter cells not associated with jets or soft jets having a transverse momentum of:  $7 \text{ GeV} < p_T < 20 \text{ GeV}$ .

**Initial and Final State Radiation** Gluon radiation in the initial or final state of an event (ISR/FSR) is simulated with samples which are generated with AcerMC.

**Further Uncertainties on Signal Modelling** Other systematic uncertainties which are related to the signal modelling have to be taken into consideration, in particular, uncertainties caused by the parton distribution function sets, by different Monte Carlo generators or by various shower algorithms (see also Subsection 6.3.5).

**Top Quark Mass** The generation of the MC signal samples is based on a top quark mass of  $m_t = 172.5 \text{ GeV}$ , fixed during the event reconstruction. The uncertainty which arises because of the uncertainty on the top quark mass has to be considered. This is realised by using pseudo-data sets which rest on different top quark masses.

## 6.2 Profile Likelihood Fits to Measure the $W$ Boson Polarisation

This section describes the setup of profile likelihood fits for a measurement of the  $W$  boson polarisation. The fundamental aspects concerning those fits can be found in Chapter 4. Special attention is paid to the evaluation of different interpolation methods in order to select that one that gives the best parametrisation.

### 6.2.1 Technical Aspects

As mentioned in Subsection 6.1.6, the templates of the  $\cos\theta^*$ -distributions, which enter the profile likelihood fit, are calculated for all three possible helicity states  $F_0$ ,  $F_L$  and  $F_R$ . All input templates or histograms for all the different systematic uncertainties are composed of 15 bins characterised by an equal bin width. It is worth mentioning that the analysis is not based on a combined fit comprising different channels, as it was implemented for the  $Wt$  production measurement.

Nominal  $\cos\theta^*$ -templates are not only available for the three helicity states, denoted as  $H_{N_0}$ ,  $H_{N_L}$  and  $H_{N_R}$  and referred to as signal templates, but also for three different kinds of background contributions: One template contains  $W$ +jets background events, one QCD multijet events and another  $\cos\theta^*$ -template comprises all the remaining background events. These histograms are labelled as  $H_{W\text{jets}}$ ,  $H_{\text{QCD}}$  and  $H_{\text{RemBkg}}$ , respectively.  $N_0$ ,  $N_L$  and  $N_R$  reference the number of events with left-handed, right-handed and longitudinally polarised  $W$  bosons, respectively. A fit performed in this way does not only allow for a simultaneous estimation of the helicity fractions but also of the background contributions.

The interpolation or morphing step is carried out for all the three signal and three background distributions. The  $\pm 1\sigma$  or up- and down-templates for all considered nuisance parameters are available for all these six kinds of input templates, which means that six morphed histograms constitute the outcome of this interpolation step. It should be added that no variations for the QCD background are used, so that the corresponding up- and down histograms are equal to the nominal one. This is due to the data-driven estimation of QCD multijet events.

Different interpolation methods, which can be used for the  $W$  boson polarisation measurement, are studied in Section 6.2.2.

For reasons of clarity, the different signal and background templates can be written as a combination of one signal and one background distribution, in the following denoted as  $H_S$  and  $H_B$ . The signal histogram depends on several fit parameters, first of all, on the used nuisance parameters  $\vec{k}$ , normalisation parameters and selection efficiencies for all the three signal templates. The fit is implemented in such a way that the scale or normalisation parameters of these signal samples are equal to the number of events contained in the corresponding sample including either left-handed, right-handed or longitudinally polarised  $W$  bosons - but before the different selection cuts are applied. This is due to the fact that the selection efficiency is different for the

$t\bar{t}$  signal samples which contain these left-handed, right-handed and longitudinally polarised  $W$  bosons. The selection efficiency for the right-handed samples is higher because charged leptons emitted from right-handed  $W$  bosons have a harder  $p_T$ -spectrum than those coming from left-handed  $W$  bosons. The  $p_T$ -spectrum of right-handed  $W$  bosons is harder, as they have the same flight direction as the top quark from whose decay they originate, as illustrated in Fig. 2.6. Left-handed  $W$  bosons are emitted in the opposite flight direction with respect to the top quark leading to a smaller probability that the decay products of the underlying  $W$  boson decay fulfil the selection requirements because of their softer  $p_T$ -spectrum.

Therefore,  $H_S$  does not only depend of the scale factors  $N_0$ ,  $N_L$  and  $N_R$  but also on the selection efficiencies  $\varepsilon_{N_0}$ ,  $\varepsilon_{N_L}$  and  $\varepsilon_{N_R}$ .  $H_B$ , on the other hand, simply depends on the applied nuisance parameters  $\vec{k}$  and scale parameters for the three different background templates. These normalisation parameters as further fit parameters directly correspond to the number of background events of the associated background source:  $W$ +jets events, QCD events or events belonging to the remaining backgrounds. Consequently, considering all the different dependencies, the different signal and background contributions  $H_S$  and  $H_B$  can be written as:

$$\begin{aligned} H_S(\vec{k}, \vec{N}_S, \vec{\varepsilon}_{N_S}) &= H_{N_0}(\vec{k}) \cdot N_0 \varepsilon_{N_0} + H_{N_L}(\vec{k}) \cdot N_L \varepsilon_{N_L} + H_{N_R}(\vec{k}) \cdot N_R \varepsilon_{N_R} \\ H_B(\vec{k}, \vec{N}_B) &= H_{W\text{jets}}(\vec{k}) \cdot N_{W\text{jets}} + H_{\text{QCD}}(\vec{k}) \cdot N_{\text{QCD}} + H_{\text{RemBkg}}(\vec{k}) \cdot N_{\text{RemBkg}}, \end{aligned}$$

whith the vectors  $\vec{N}_S = (N_0, N_L, N_R)$ ,  $\vec{N}_B = (N_{W\text{jets}}, N_{\text{QCD}}, N_{\text{RemBkg}})$  and  $\vec{\varepsilon}_{N_S} = (\varepsilon_{N_0}, \varepsilon_{N_L}, \varepsilon_{N_R})$ . Starting from these two distributions  $H_S$  and  $H_B$ , the distribution  $H_{\text{sum}}$  as a sum of these two can be written as:

$$H_{\text{sum}}(\vec{k}, \vec{N}_S, \vec{N}_B, \vec{\varepsilon}_{N_S}) = H_S(\vec{k}, \vec{N}_S, \vec{\varepsilon}_{N_S}) + H_B(\vec{k}, \vec{N}_B).$$

The six different templates, here written in the condensed form  $H_{\text{sum}}$ , resulting from MC distributions are then fitted to the data distribution  $H_{\text{data}}$ .

The likelihood function in Eq. (4.7) is again used for the minimisation process. The mean values and uncertainties of the background parameters are set to the expected values given in Chapter 6.3. The uncertainties which are related to the three background contributions amount to 50% ( $W$ +jets), 100% (QCD) and 30% (remaining backgrounds) in a conservative approach and enter the second sum of Eq. (4.7) - the penalty term for the background parameters.

Apart from this procedure, a second fitting method can be implemented, similar to the second method used for the measurement of the  $Wt$  production rate. Instead of normalisation factors as fit parameters to scale the background contributions, nuisance parameters can be used to adjust the size of the different backgrounds. This alternative fitting procedure can be used to cross-check the results obtained from the first fitting method, as the quality of both is assumed to be equivalent. In order not to exceed the scope of this thesis, this cross-check is not included in this chapter but can be found in App. C.

### 6.2.2 Evaluating the Available Interpolation Methods

Several possible methods with which the morphing step of the profile likelihood fit can be performed are described in Subsection 4.4. All these interpolation procedures have been studied in the course of this thesis.

In order to figure out how suitable a certain fitting method is, templates containing the  $\pm 2\sigma$ - and  $\pm 3\sigma$ -variations can be produced for the nuisance parameters. The bin entries of one certain bin of the nominal and the  $\pm 1\sigma$ -,  $\pm 2\sigma$ - and  $\pm 3\sigma$ -variations of one of the six signal or background contributions for a specific morphing parameter  $k_j$  are then plotted as a function of this parameter  $k_j$  ranging from -3 to +3. Such a plot can be created for all bins of all six input signal and background contributions and all systematic uncertainties each represented by a nuisance parameter. This allows to visualise how far the different up- and -down variations affect the bin entries and the shape of the input histograms in general, e.g. if these variations are symmetric around the nominal value or not.

To validate the quality of the different interpolation methods, the different curves of the interpolation functions belonging to the first three morphing methods pursuant to Eq. (4.1) to Eq. (4.6) are plotted in the same coordinate system. At the end of Section 4.4, a further technique based on a quadratic fit was introduced. The fitted parabola belonging to this fourth interpolation method is displayed in the same plot as well. Such an illustration that does not only contain the histogram entries but also the different interpolation curves allow to investigate whether the individual approaches describe the behaviour of the bin entries properly.

For one bin of the signal distribution  $H_{N_0}$  containing the events with a longitudinally polarised  $W$  boson, based on the nuisance parameter  $k(\text{JES})$  due to the uncertainty on the jet energy scale, this plot is exemplarily shown in Fig. 6.3. In the bottom half, the ratio of the bin entries, denoted as “nom” to the different interpolation curves at that point is given. The ratio as well as a  $\chi^2$ -test serve to estimate the quality of the four approaches (see below).

Considering all data points, the ratio belonging to the linear interpolation method is often comparatively close to the desired value of one. But the straight line corresponding to this method displays that deviations even occur for  $k_j$ -values close to zero since the linear approach is defined in such a way that values of  $k_j = \pm 1$  do not lead to  $H_{\pm 1\sigma, ij}$ , as already pointed out in Chapter 4.4.

The curves belonging to the piecewise linear or the quadratic interpolation describe the bin entries of the underlying templates comparatively well in the interval ranging from -1 to +1. But for  $|k_j| > 1$ , the discrepancies between the histogram values and the interpolation curves increase significantly as the related ratios at the bottom of Fig. 6.3 reveal. These deviations actually affect the fit result although the nuisance parameters normally range from -1 to +1, as pseudo-experiments underline that have been performed to validate the fitting method. Especially if the up- and down-variations are of the order of statistical fluctuations (see Chapter 6.3.2), using these two interpolation procedures can cause a remarkable bias visible in the distributions of the fit parameter values resulting from the pseudo-experiments.

Hence, a fourth method has been tested, the one which is based on a quadratic

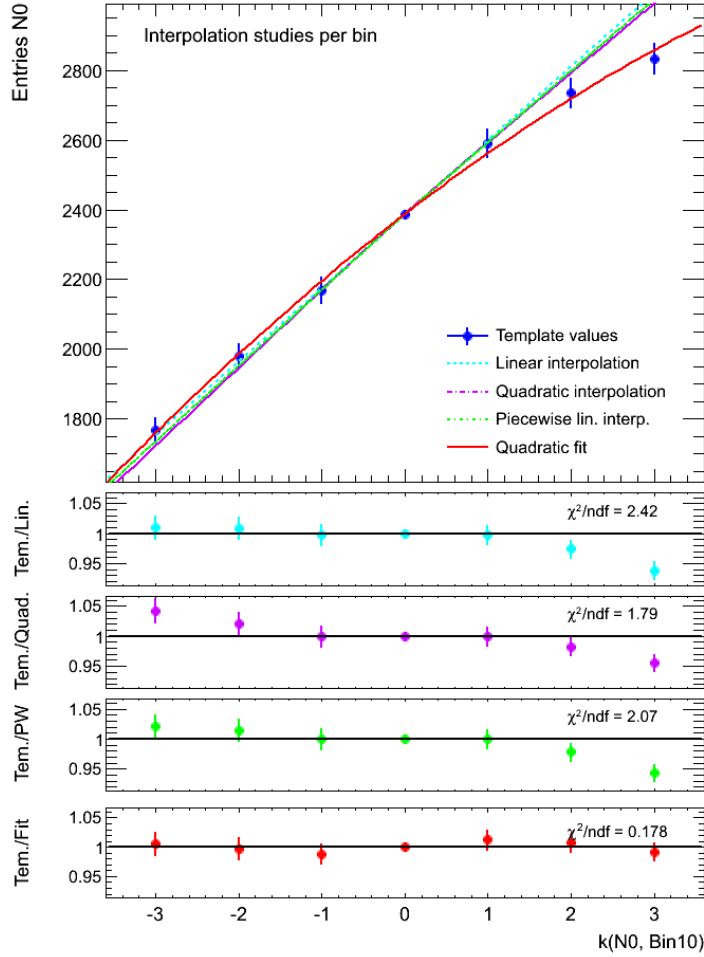


Figure 6.3: Interpolation curves of the different used interpolation methods for one exemplary bin. Chosen is bin 10 of the signal distribution  $H_{N_0}$  based on the nuisance parameter  $k(\text{JES})$ . The different bin entries of the underlying templates are marked in blue. The interpolation curves are coloured and hatched according to the legend. At the bottom, the ratio of the bin entry to the corresponding value of the interpolation curve is shown - separately for all approaches. The quality of the methods is quantified by a  $\chi^2$ -test; results are shown in the ratio plot.

fit. The ratio plot of this quadratic fit interpolation reveals deviations from the template values compared to the piecewise linear and quadratic interpolation method if  $|k_j| < 1$ , but the deviations are comparatively small and remain small when larger  $k_j$ -values are taken into account. Using this approach thus minimises the risk of a bias in case higher values are fitted, proven in Chapter 6.3.3, when the validation of the fit is outlined.

Different plots for all bins of all input signal and background contributions and nuisance parameters have been studied. Since all of them feature a similar behaviour as the one shown here exemplarily, the chosen bin can be regarded as representative. Consequently, the approach based on a quadratic fit is used for the analyses presented in the upcoming sections.

This choice can also be justified quantitatively by performing a  $\chi^2$ -test. Such a test indicates the quality of the underlying fit. The larger the  $\chi^2$ -value the larger is the deviation between the expectation, in this case the curve belonging to the interpolation method, and the given data, in this case the bin entries of the input histograms. The  $\chi^2$ -value divided by the number of degrees of freedom (ndf) for all different interpolation methods can be found in the associated ratio plots at the bottom of Fig. 6.3. This normalised  $\chi^2$ -value of the quadratic fit is usually very small, stressing the good agreement between the data points and the fitted curves and underlining why this method has been chosen. The other interpolation methods possess larger  $\chi^2$ /ndf-numbers. In the presented plot, the quadratic interpolation gives the second smallest number. There are, however, bins, in which due to the linear extrapolation beyond the  $\pm 1\sigma$ -range large discrepancies between the interpolation curve and the bin entries occur, consequently leading to much larger  $\chi^2$ /ndf-values, outvaluing those of other interpolation methods.

### 6.2.3 Nuisance Parameters and Other Fit Parameters

To summarise, apart from the nuisance parameters, at least six parameters enter the fit. These fit parameters comprise three signal parameters as normalisation factors and three background parameters. In the previous subsections, these parameters were denoted as  $N_0$ ,  $N_L$  and  $N_R$  for the signal and as  $N_{W\text{jets}}$ ,  $N_{\text{QCD}}$ , and  $N_{\text{RemBkg}}$  for the three backgrounds. The start values of the normalisation parameters are chosen according to the MC expectation.

Since various nuisance parameters and varying numbers of these parameters have been tested, possible profiling parameters are introduced in Chapter 6.3. The start values of these nuisance parameters are set to zero.

Pursuant to Eq. (4.7), Gaussian constraints are imposed on all used nuisance parameters and on the three background normalisation parameters with the uncertainties mentioned in Section 6.2.1.

## 6.3 *W* Boson Polarisation: Results

Testing and validating the applied fitting method is in the centre of attention in this chapter, presenting the fit results of the *W* boson polarisation measurement.

The fits presented here are based on TMinuit with an individually set up code which enables further studies and performance checks and which thus ensures an easier implementation of validation techniques and different interpolation methods. An implementation which rests on the use of normalisation parameters to fit the background functions as the default fitting method is presented in depth. The description of other methods including a HistFactory fit is briefly addressed in App. C to present options allowing to cross-check the obtained results.

To begin with, some information concerning the calculation of helicity fractions, the computation of the uncertainties on the fit parameters and the used systematic uncertainties is given, followed by a detailed explanation of the validation of the fitting method. Afterwards, the method is applied to data and the obtained results are discussed extensively.

### 6.3.1 Evaluation of the Helicity Fractions and Their Uncertainties

The helicity fractions  $F_0$ ,  $F_L$  and  $F_R$  are calculated with the help of the fitted signal parameters  $N_0$ ,  $N_L$  and  $N_R$ . Taking the selection efficiencies into account, the signal numbers given in the templates can be written as:

$$N_{i,\text{Templ.}} = \varepsilon_{N_i} \cdot N_i \quad \text{with} \quad i = 0, L, R.$$

As stated above, the  $N_i$  as normalisation factors are directly estimated in the fit. The total number of events in due consideration of the background contributions yields:

$$N_{\text{tot}} = N_0 + N_L + N_R + N_{\text{Wjets}} + N_{\text{QCD}} + N_{\text{RemBkg}}.$$

This number is considered in the later analysis as it allows to check the performance of the fit. The fitted values of the signal templates can be directly used to evaluate the helicity fractions:

$$F_i = \frac{N_i}{N_0 + N_L + N_R} \quad \text{with} \quad i = 0, L, R. \quad (6.2)$$

The related uncertainties of the fit can be estimated as follows: The uncertainties on the fit parameters can be directly obtained from the TMinuit fit. To be more exact, a Hesse algorithm based on the Hessian matrix is used, as introduced in Section 5.3.1. Apart from this calculation of uncertainties, a self-implemented *profiling method* can be used to evaluate the uncertainties of the fit and to check the quality of this TMinuit uncertainties, which is explained more extensively in Section 6.3.3.2.

The uncertainties on the helicity fractions are obtained taking the covariance matrix into consideration which can be gained from TMinuit on the basis of the Hesse calculation or from ensemble tests, presented in Section 6.3.3.2. The covariance

matrix is of the following form:

$$V = \begin{pmatrix} \sigma_{N_0}^2 & \sigma_{N_0}\sigma_{N_L}\varrho(N_0, N_L) & \sigma_{N_0}\sigma_{N_R}\varrho(N_0, N_R) \\ \sigma_{N_L}\sigma_{N_0}\varrho(N_L, N_0) & \sigma_{N_L}^2 & \sigma_{N_L}\sigma_{N_R}\varrho(N_L, N_R) \\ \sigma_{N_R}\sigma_{N_0}\varrho(N_R, N_0) & \sigma_{N_R}\sigma_{N_L}\varrho(N_R, N_L) & \sigma_{N_R}^2 \end{pmatrix}$$

with the correlation  $\varrho(x, y)$  between the variables  $x$  and  $y$ .  $\sigma$  denotes the uncertainties, according to the common notation. The uncertainties on the helicity fractions can then be computed by means of error propagation with their dependence on  $V$  which finally results in:

$$\sigma_{F_i}^2 = \sum_{k=0,L,R} \sum_{l=0,L,R} \frac{\partial F_i}{\partial N_k} \frac{\partial F_i}{\partial N_l} \cdot \sigma_{N_k}\sigma_{N_l}\varrho(N_k, N_l) \quad \text{with} \quad i = 0, L, R. \quad (6.3)$$

The correlations between the different fit parameters have a considerable impact on the uncertainty of the fit, as presented in Chapter 6.3.4.

### 6.3.2 Overview of Profiled Systematic Uncertainties

Several of the systematic uncertainty listed in Section 6.1.7 cannot be fitted via nuisance parameters. This paragraph serves to delineate which nuisance parameters are used in the profile likelihood fit in this analysis.

A characteristic of such fits is that only continuous sources of systematic uncertainties can be added to the minimisation process. Those originating from discrete sources require a separate evaluation, which is further described in Section 6.3.5.

At first, the scale factor uncertainties are allowed to be fitted as nuisance parameters. One scale factor emerges from the jet vertex fraction, abbreviated as ‘‘JVFSF’’, three additional scale factors arise from muon-related uncertainties which account for the identification, the reconstruction and the trigger efficiency of muons, denoted as ‘‘MUON\_ID’’, ‘‘MUON\_RECO’’ and ‘‘MUON\_TRIG’’. Three other nuisance parameters are added on the basis of  $b$ -tagging scale factors. Separate scale factors are applied to distinguish between  $b$  quarks (BTAG),  $c$  quarks (CTAG) and lighter quarks (MISTAG).

Concerning the muon energy scale and resolution, three further nuisance parameters can be applied. One accounts for the muon energy scale (MUSC), two others are used to estimate the impact of the muon energy resolution separately in the Inner Detector (MUID) and in the muon spectrometer (MUMS). For the studies presented here, only the muon energy scale is profiled. The other two uncertainties are very small - of the order of statistical fluctuations. Hence, the benefit of using these two uncertainties as nuisance parameters is marginal. Due to the small effect of these systematics a lot of bins feature the behaviour that the associated bin entries of the  $+1\sigma$ - and the  $-1\sigma$ -histogram are both smaller or, respectively, both larger than the nominal value. Although the effect is comparatively tiny, such a behaviour causes a bias in the distributions resulting from pseudo-experiments to study the stability of the fit, as several tests revealed. Consequently, these uncertainties are not profiled.

Three different systematic uncertainties are based on the missing transverse energy: Two uncertainties emerge from soft jets (SOFTJET) and from calorimeter cells which are not associated to reconstructed jets (CELLOUT). Another systematic uncertainty considers pile-up effects and also influences the missing transverse energy calculation (PILE-UP). However, these three uncertainties are very small, resulting in  $\pm 1\sigma$ -variations which are almost negligible and thus again of the order of possible statistical effects. Accordingly, these three uncertainties are not profiled either.

The following three systematic uncertainties are related to jets and constitute systematics which are fitted via nuisance parameters. These account for uncertainties which are due to the jet energy scale (JES), the jet energy resolution (JER) and the jet reconstruction efficiency (JEFF). The jet energy scale uncertainty demands a more detailed description:

The JES is a compound systematic uncertainty that, regarding the 2011 data analysis, is composed of 16 individual components. Six of these components come from the in-situ calibration, one from the jet calibration, two from the jet intercalibration and one from the high- $p_T$  extrapolation. Two further JES components arise from pile-up effects, two take the flavour composition and the flavour response into account while another one considers close-by jets. The last component constitutes a  $b$ -JES uncertainty. All of these components have been studied in the framework of this thesis. It has been shown that only eight components influence the shape and the number of events of the corresponding  $\pm 1\sigma$ -histograms in comparison to the nominal template whereas the impact of the others is barely existing. These eight components are the two flavour-related uncertainties, two of the in-situ calibration components, one pile-up and one intercalibration uncertainty and finally those which originate from close-by jets and from the  $b$ -JES uncertainty. But not all of these uncertainties can be used as nuisance parameters in the profile likelihood fit. Only the flavour composition uncertainty and the first five in-situ components are officially approved to be profiled, excluding the last one, the so-called “rest term”. Terms like the intercalibration, the  $b$ -JES and the flavour response uncertainty cannot be profiled since these are not continuous but two-point systematics. The other uncertainties are not authorised to be fitted via nuisance parameters because the correlations of these components are not yet fully understood. This means, regarding the eight chosen terms, that only the two in-situ and the flavour composition uncertainty can be applied to the fit via profiling parameters.

As these remaining three components do not heavily affect the shape of the  $1\sigma$ -up and down-templates, splitting the JES into its different terms is not remarkably worthwhile, especially in the framework of this thesis considering that the centre of attention is placed on the understanding of the fitting method in general. Consequently, only one profiling parameter  $k(\text{JES})$  is used for the jet energy scale.

It should be added that for three of the uncertainties introduced so far only one histogram containing either the up- or the down-variations is available. These so-called one-sided systematics are: MUSC, JEFF and JER. However, since these three uncertainties enter the fit, the distributions of both up- and down-variations need to be available to perform the fit properly. The missing histogram is thus produced by

symmetrising the effect of those one-sided systematics. For most studies, especially those carried out in the course of this thesis, such an approach is justifiable, as long as only  $\pm 1\sigma$ -variations are considered. Concerning larger variations, the artificial symmetrisation may cause a bias.

The following systematic uncertainties are not fitted as nuisance parameters, mainly due to the fact that these systematics are discrete ones which cannot be profiled. Those account for the colour reconnection, the MC generator choice, parton showering, the PDFs, the QCD background, the  $W$ +jets background, the top quark mass uncertainty and initial and final state radiation. The templates to estimate the uncertainty due to the top quark mass and the PDFs, though, are not evaluated yet and are therefore not considered in the following analysis. Furthermore, other systematic effects caused by the template statistics or by  $Z$ +jets events are not taken into account yet as they are assumed to have a negligible impact on the measurement. The uncertainty which is occasioned by the  $W$ +jets background only affects the  $W$ +jets templates so that the entire uncertainty is expected to be negligible. As a consequence, the  $W$ +jets background uncertainty is not applied for the studies presented in this thesis.

Electron-related uncertainties are not considered as well, neither as nuisance parameters nor in the context of a different treatment of systematic uncertainties since they are too small to cause a measurable effect.

The different available systematic uncertainties are summarised in Table 6.2. The used fitting method for all sources and, if necessary, the different profiling parameters are listed as well. The list shows that, in total, eleven nuisance parameters remain which can be used for the profile likelihood fit.

For all systematic uncertainties which enter the fit via nuisance parameters, at least  $\pm 1\sigma$ -variations are available. As mentioned in Chapter 4.4, most interpolation methods are based on these  $\pm 1\sigma$ -variations. The precision of a more sophisticated method, previously referred to as quadratic fit method, can be further improved by adding  $\pm 2\sigma$ - and even  $\pm 3\sigma$ -templates. This interpolation method gives most appropriate results, as described in Section 6.2.2, and is thus used for most of the studies presented in the following.

At first, plots have been studied showing the bin entries as a function of the nuisance parameter  $k_j$  comparable to Fig. 6.3 but containing only the  $\pm 1\sigma$ -variations. The interpolation curves mostly reveal a rather linear behaviour, exemplarily shown for  $k(\text{BTAG})$  in Fig. A.3 in the appendix. Solely the interpolation curves based on the JES-templates exhibit remarkable deviations from a linear slope. As long as only a slight difference between the curve emerging from a quadratic fit and the other curves can be observed, the  $\pm 1\sigma$ -variations are regarded as being sufficient for the profile likelihood fit. Hence, the nuisance parameter due to the jet energy scale is the only fit parameter for which  $\pm 2\sigma$  and even  $\pm 3\sigma$ -variations are used here.

The nominal template as well as all the different up- and down-histograms for the JES are shown in Fig. 6.4. In contrast to the templates of other systematic effects, the bin entries vary significantly between the different templates. In case the nominal

Systematic Uncertainty	Nuisance Parameter	Remarks
Signal and Background Modelling		
MC generator choice	-	
Parton showering	-	
PDF uncertainty	-	
ISR/FSR	-	
Colour reconnection	-	
Top quark mass	-	
QCD background	-	
$W$ +jets background	-	affects $W$ +jets templates only
Other backgrounds	-	
Template statistics	-	
Detector Modelling		
Scale factors	$k(\text{JVFSF})$ $k(\text{MUON\_ID})$ $k(\text{MUON\_RECO})$ $k(\text{MUON\_TRIG})$	jet vertex fraction muon identification muon reconstruction muon trigger
Muon energy scale	$k(\text{MUSC})$	one-sided effect
Muon energy resolution	-	2 components account for ID and muon system
Jet energy scale	$k(\text{JES})$	not split into its 16 components
Jet energy resol.	$k(\text{JER})$	one-sided effect
Jet reconstruction eff.	$k(\text{JEFF})$	one-sided effect
$b$ -tagging	$k(\text{BTAG})$ $k(\text{CTAG})$ $k(\text{MISTAG})$	accounts for $b$ quarks accounts for $c$ quarks accounts for lighter quarks
Missing transv. energy	-	3 components

Table 6.2: List of the different sources of systematic uncertainties. If nuisance parameters are used for a certain systematic effect, the names of the corresponding profiling parameters are listed in the second column whereas the last column contains further noteworthy comments or explanations concerning the abbreviations. More information is given in the text. For reasons of clarity, the systematic effects are divided into uncertainties related to signal and background modelling and to detector modelling.

value is small, there can arise fluctuations which may lead to the situation that the entries of the  $+1\sigma$ - and the  $-1\sigma$ -histogram bins are both smaller or both larger than the associated nominal bin value. This may cause a bias of the fit result which can be corrected by a quadratic fit as long as it includes variations exceeding  $1\sigma$ . This underlines the necessity of using those additional templates. These fluctuations are negligible concerning the other profiling parameters confirming that the other systematics do not obligatorily require more than one up- and one down-template for the following studies. Those observations give rise to the assumption that the JES may affect the results of the profile likelihood fit significantly.

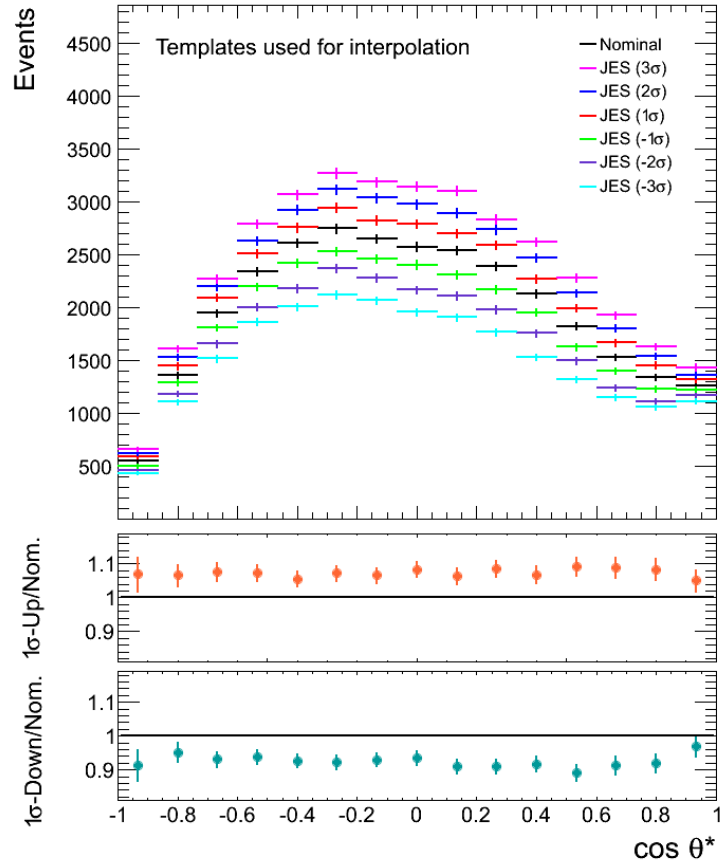


Figure 6.4: The different templates corresponding to  $\pm 1\sigma$ - to  $\pm 3\sigma$ -variations based on the systematic uncertainty arisen from the jet energy scale for the fit parameter  $N_0$ . The nominal distribution can be found in the middle, coloured in black. The differences between the templates are large, especially compared to the distributions for the other available nuisance parameters. At the bottom, the ratio of the  $1\sigma$ -up-/down-variations to the nominal sample per bin is presented. For the displayed JES, the ratio plot shows a substantial deviation from one.

To also visualise the shapes of the templates of the other signal parameters, these are shown for reasons of completeness in Fig. A.4 and Fig. A.5 in the appendix.

At the bottom of Fig. 6.4 also the ratio between the  $1\sigma$ -up- and down-templates and the nominal one is shown. The ratio clearly deviates from one, underlining the impact of the jet energy scale.

It is worth mentioning that not only the number of events might change between the up-/down-variations and the nominal distribution, also the shape of the underlying histograms can vary. To visualise such an effect, the templates  $H(-1\sigma)$ ,  $H(\text{nominal})$  and  $H(+1\sigma)$ , can be normalised and again be plotted in one figure. This is shown in Fig. 6.5 exemplarily for the  $\pm 1\sigma$ -variations of the jet energy scale. Additionally, the effect of other systematic uncertainties was examined similarly revealing that, apart from the JES, also the jet energy resolution is one of the systematic uncertainties which influence the shape most.

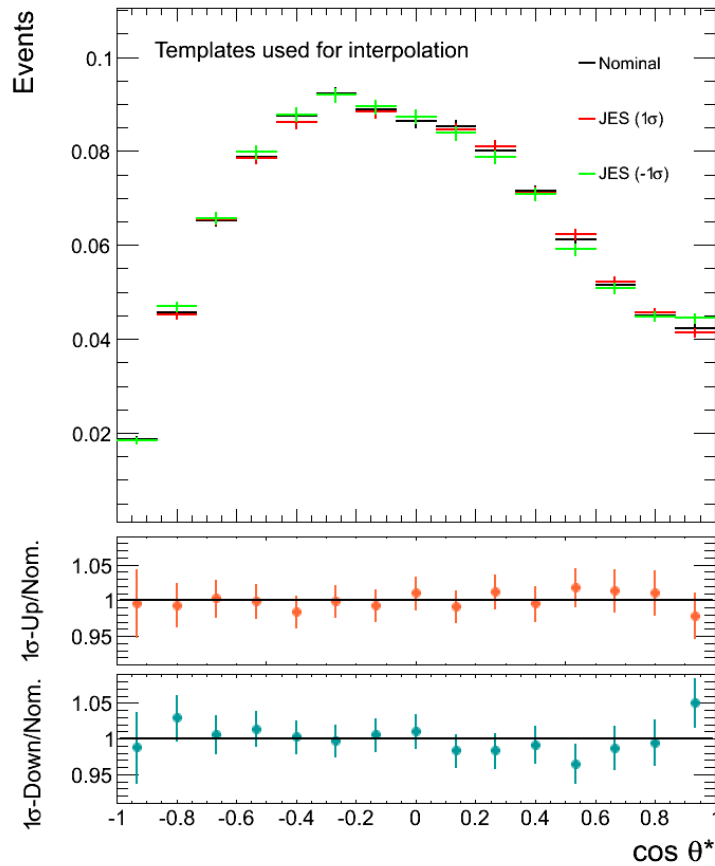


Figure 6.5: The different normalised templates corresponding to  $\pm 1\sigma$ -variations based on the systematic uncertainty arisen from the JES for the fit parameter  $N_0$ . The nominal distribution is coloured in black. The differences between the templates concerning the shape are clearly visible. At the bottom, the ratio of the  $1\sigma$ -up-/down-variations to the nominal sample per bin is presented. The ratio plot shows deviations from one for the displayed normalised JES templates.

### 6.3.3 Pseudo-Experiments

The measurement of the  $W$  boson helicity fractions is tested and validated by using MC simulated events. For this purpose, pseudo-experiments (PEs) are used, allowing for stability and performance studies. In this subsection, the fundamentals of pseudo-experiments and the implementation of corresponding ensemble tests are described, followed by a presentation of the obtained results.

#### 6.3.3.1 How to Perform Pseudo-Experiments

The pseudo-data sets are generated by using a combination of signal and background templates normalised to an integrated luminosity of about  $4.7 \text{ fb}^{-1}$  summarised in one  $\cos \theta^*$ -distribution. The predicted number of events per bin is presumed to be distributed pursuant to a Poissonian distribution. Accordingly, a new pseudo-data set is derived from the  $\cos \theta^*$ -distribution with bin entries regarded as Poisson-distributed and a mean equalling the original expectation of events for the corresponding bin. Random shifts of the start values of the different fit parameters - before performing the fit to such a set of pseudo-data - are implemented as well. Since the nuisance parameters  $k_j$  and the normalisation parameters  $N_i$  are assumed to possess Gaussian-shaped uncertainties, these variations are gained from a Gaussian distribution with a standard deviation following the  $\pm 1\sigma$ -range of the underlying parameters and a mean corresponding to the expected values of all fit parameters. The fit is then performed using a quadratic fit for the interpolation.

Pseudo-experiments are carried out in series of about 1,000. The obtained values for each single fit are added to histograms set up for all different fit parameters. The average fitted value for each single parameter can be evaluated by using the mean value of these histograms including all fit results. Besides, *pull distributions* are plotted for all fit parameters. Pull values are calculated as the difference between the fitted value and the expected one divided by the estimated uncertainty on the fit result. The average fitted pull value is expected to be zero, the corresponding uncertainties to be one, as long as no additional fit constraints are employed. The mean values of the resulting distributions as well as the associated  $1\sigma$ -uncertainties are again directly extracted from the histograms. All of these distributions are also drawn up for the helicity fractions  $F_i$  calculated according to Eq. (6.2).

The pseudo-experiments are based on values for the helicity fractions close to the SM prediction, stated in Chapter 2.2.4, and are simply marked by the index “exp”:  $F_{0,\text{exp}} = 0.7$ ,  $F_{L,\text{exp}} = 0.3$  and  $F_{R,\text{exp}} = 0.0$ .

**Deriving Fit Uncertainties** Before the desired fit to data is performed, the expected uncertainty of the used fitting method can be computed with the help of pseudo-experiments. If no nuisance parameters are added to the fit (solely six normalisation parameters for the signal and background contributions), the mean values of the distributions containing the uncertainties on the helicity fractions that result from the pseudo-experiments with their Gaussian shapes yield the expected statistical uncertainty of the corresponding fraction.

If all nuisance parameters are used in the minimisation process, the means of the uncertainty distributions obtained from a series of pseudo-experiments specifies an

uncertainty which includes both the statistical and the systematic ones. This systematic uncertainty only considers the sources of systematics which enter the fit via profiling parameters. As illustrated in Chapter 6.3.5, the total systematic uncertainty comprises the contributions coming from all those systematics which are not profiled.

It is noteworthy that due to the correlations between the normalisation parameters  $N_i$ , which are used in the calculation of the helicity fractions pursuant to Eq. (6.3), individual systematic uncertainties cannot be determined directly with the help of the expected statistical and the just mentioned combined uncertainty. Such a procedure works, however, for the fit parameters like the normalisation factors.

**Validating the Stability of the Fit** In a next step, the stability of the fitting method is tested using pseudo-data sets with different input values for the helicity fractions, apart from the values close to the SM expectation listed above. For this purpose, pseudo-data sets are created starting with input values of  $F_{0,\text{inp}} = 0.4$ ,  $F_{L,\text{inp}} = 0.45$  and  $F_{R,\text{inp}} = 0.15$ . For the following other configurations, the input value of  $F_0$  is increased by 0.1, the ones of  $F_L$  and  $F_R$  are reduced by 0.05, in each step. Pseudo-data sets are created and 1,000 pseudo-experiments are performed for all of these configurations until values of  $F_{0,\text{inp}} = 1.0$ ,  $F_{L,\text{inp}} = 0.15$  and  $F_{R,\text{inp}} = -0.15$  are reached. The average measured helicity fractions can again be gathered from the mean of the histograms or distributions in which the fit results are filled for all given configurations of input fractions. These measured values are then plotted as a function of the input fractions, shown in Section 6.3.3.2. A linear fit to these points around the Standard Model helicity fractions is anticipated to reveal a slope of one and no offset - measured as an intercept of the ordinate. These linear curves, in the following denoted as *calibration curves*, can also be plotted for the normalisation parameters. As the number of signal events depends on the helicity fractions, the corresponding linear fit should give similar results - intercept of zero and a slope of one - while the number of background events is assumed to be constant. Consequently, the number of background events for each of the three contributions plotted as a function of the helicity fractions should result in a straight line with a slope consistent with zero and an intercept of the ordinate close to the anticipated number of background events. A comparable plot can be drawn for the nuisance parameters with a suitable linear fit which is expected to reveal a straight line with an intercept of zero, equal to the presumed profiling parameter value.

Deviations from the expectation would indicate that the fitting method does not hold a perfect linearity and corrections to ensure independence of the expected helicity fractions are required.

Also pull distributions serve to assess the modelling of the fit. For all these different input configurations of helicity fractions, pull distributions are depicted as well. Remarkable discrepancies from the expected mean values and standard deviations may point out that the uncertainties are possibly under- or overestimated.

### 6.3.3.2 Results of Pseudo-Experiments

**Parameter Distributions and Expected Uncertainties** According to the remarks in Section 6.3.3.1, series of 1,000 pseudo-experiments have been performed and the fitted values have been filled in histograms, one for each used fit parameter as well as for the three helicity fractions to test the performance of the fit. These pseudo-experiments are based on input values for the helicity fraction which are close to the expected values:  $F_{0,\text{exp}} = 0.7$ ,  $F_{L,\text{exp}} = 0.3$  and  $F_{R,\text{exp}} = 0.0$ .

Pseudo-experiments have been carried out based on fits without any nuisance parameters and with all selected eleven profiling parameters to evaluate possible differences between these two fits since a possible bias or asymmetries of the distributions may occur when more fit parameters are used, leading to a decrease in the stability of the fit. Another reason for plotting these parameter distributions is to generally test their Gaussian shape and thus the performance of the applied fitting method. Shifted or biased distributions, for instance, would indicate some underlying problems with the fitting method. Biases may be caused by an interpolation method which does not describe the input data properly.

An important measure for such studies is the spread of the individual helicity fractions. This spread is expressed by the standard deviation, in the plots denoted as “sigma” and complying with the width of the distributions.

In Fig. 6.6, two distributions for the helicity fraction  $F_L$  are exemplarily shown. The left distribution corresponds to fits not using any nuisance parameters, the one on the right displays the results of pseudo-experiments based on all applied eleven profiling parameters.

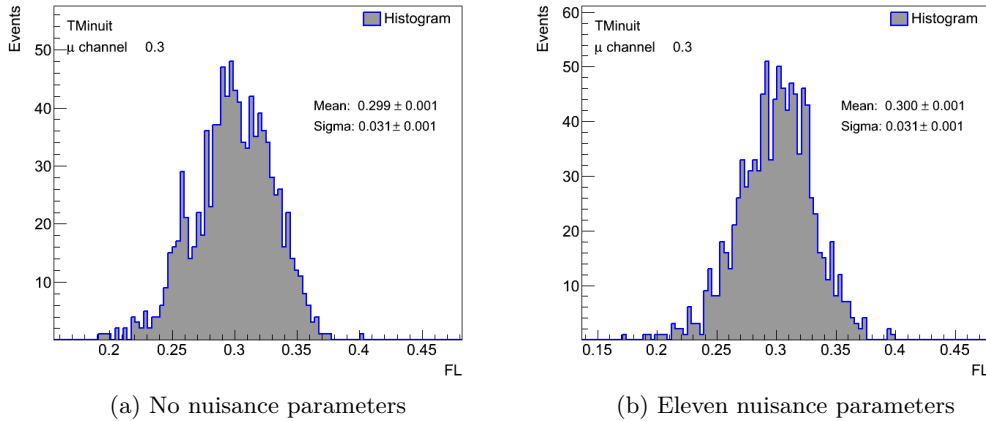


Figure 6.6: Distributions of fitted values for the helicity fraction  $F_L$  obtained from 1,000 pseudo-experiments based on input values  $F_{0,\text{exp}} = 0.7$ ,  $F_{L,\text{exp}} = 0.3$  and  $F_{R,\text{exp}} = 0.0$ . The underlying fits have been performed with (a) no nuisance parameters or with (b) all chosen eleven nuisance parameters added to the fit.

The average mean values are very close to the anticipated input values, the uncertainties cover very small deviations. The standard deviation of the distributions is in both cases very similar. Depending on the analysis, this standard deviation or

width of the distribution is a measure of the expected uncertainty of the underlying parameter. Regarding this measurement of the *W* boson polarisation, as mentioned in Section 6.3.2, Gaussian constraints are imposed on the background parameters and on all added nuisance parameters. This influences the resulting widths of the parameter distributions significantly so that the width cannot be used for an estimation of the expected parameter uncertainties. These Gaussian constraints also explain why the width does not increase if more fit parameters, nuisance parameters in this case, are added although they cause an additional systematic uncertainty. Those distributions have been plotted for all other fit parameters comprising the nuisance parameters - if they are used in the fit. All of these distributions feature the effect visible in the plots for  $F_L$ . This can exemplarily be seen in Fig. 6.7, displaying the plots which correspond to Fig. 6.6 for the normalisation factor  $N_L$ . The fitted mean values are at least approximately in the  $2\sigma$ -range around the expected number, which is given in the upper left corner of the figures, regarding the calculated uncertainty on this average value.

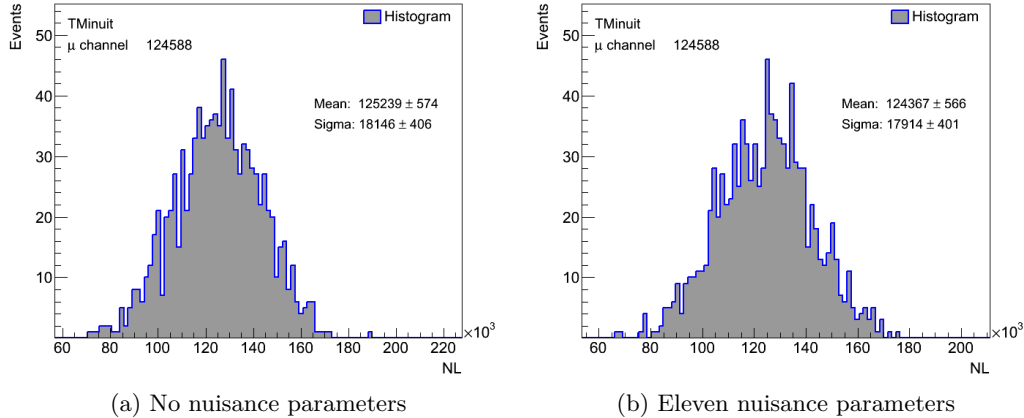


Figure 6.7: Distributions of fitted values for the signal parameter  $N_L$  obtained from the same 1,000 pseudo-experiments on which the distributions in Fig. 6.6 are based. The fits have been performed with (a) no nuisance parameters or with (b) all chosen eleven nuisance parameters added to the fit.

Similar distributions have also been plotted for the total number of fitted events  $N_{\text{tot}}$  involving all signal and background contributions to investigate whether this total number differs from the expectation. Concerning the standard deviation of the distribution, the fitted values agree well with the presumed number within the  $3\sigma$ -range, as illustrated in Fig. 6.8.

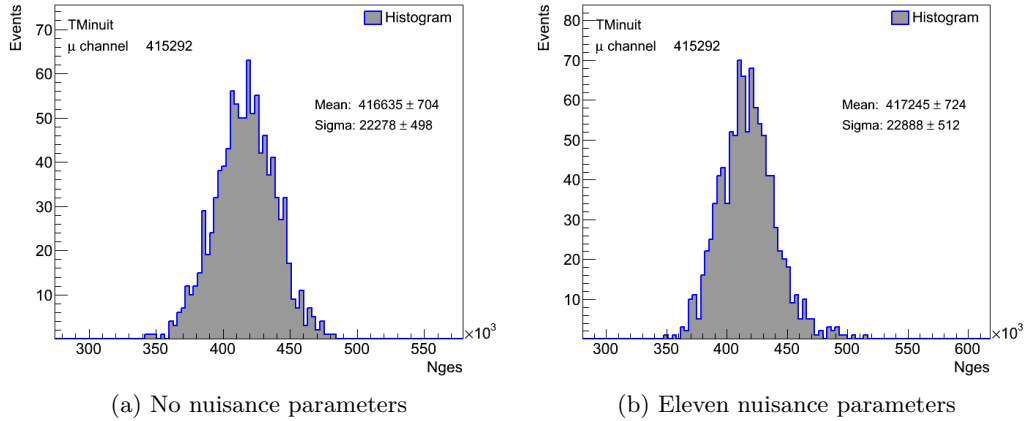


Figure 6.8: Distributions of fitted values for the number of fitted events  $N_{\text{tot}}$  obtained from the same 1,000 pseudo-experiments on which the distributions in Fig. 6.6 are based. The fits have been performed with (a) no nuisance parameters or with (b) all chosen eleven nuisance parameters added to the fit.

**Uncertainties of the Fit** Similar distributions plotted for the parameter values and described in the last paragraphs have also been produced for the associated uncertainties of the fit again for 1,000 pseudo-experiments. Several studies revealed that the shape of the resulting histograms depends strongly on the applied calculation of the uncertainties and the employed interpolation method:

The shape of the distributions does not conform with the one of a Gaussian distribution if interpolation methods like the piecewise linear, the quadratic interpolation or a too simple and not sophisticated algorithm to evaluate the uncertainties of the fit are used. In such cases, the distribution may be biased or asymmetric, or may possess several local maxima. The latter does not occur if a more sophisticated interpolation method is employed like the one based on a quadratic fit. For example, the piecewise linear interpolation can cause deviations from a Gaussian-shaped distribution due to the kink in the interpolation curve at  $k_j = 0$ , in particular, if the up- and down- variations of the underlying systematic uncertainties are very asymmetrically distributed around the nominal template.

To a certain extent, such a bias of the fit uncertainty distribution may also be caused by the underlying algorithm with which the individual uncertainties are determined. First tests are based on fits whose uncertainties are directly gained from a method implemented in TMinuit, the Hesse algorithm, which was already introduced in Chapter 5.3.1. As stated there, this calculation constitutes an adequate choice for most studies. The corresponding uncertainty histograms reveal that the shape is consistent with a Gaussian curve to a large extent. However, to further minimise the risk of biasing the fit result due to an inaccurate evaluation of the uncertainties, another fitting method has been set up.

The new algorithm was individually implemented in the already existing code. This allows for a better control of the computation and for a closer examination of dif-

ferent tests with the used algorithm although this calculation is much more time-consuming and computationally intensive compared to the relatively fast TMinuit Hesse algorithm. The alternative method uses likelihood curves as they have been introduced in Section 5.3.2, referred to as likelihood scans, in order to profile or scan the signal parameter  $N_{W_L}$ . The procedure applied here, in the following denoted as *profiling method*, is equivalent. The parameter of interest is varied around the already fitted minimum in certain steps. In each step, this parameter is fixed and the fit is repeated with the remaining fit parameters. The resulting likelihood values  $-2\ln L$  of all single fits are then plotted as a function of the underlying varied parameter. After the global minimum is shifted to zero, a quadratic fit to the resulting curve of likelihood values can be carried out. Based on the results of the quadratic fit, the half of the distance between the abscissa positions having a function value of one can be computed. The arising value is the estimate of the uncertainty searched for. In Fig. 6.9 two of these likelihood scans with the associated quadratic fit are shown. The parabola perfectly agrees with the given points confirming the choice of this fit function.

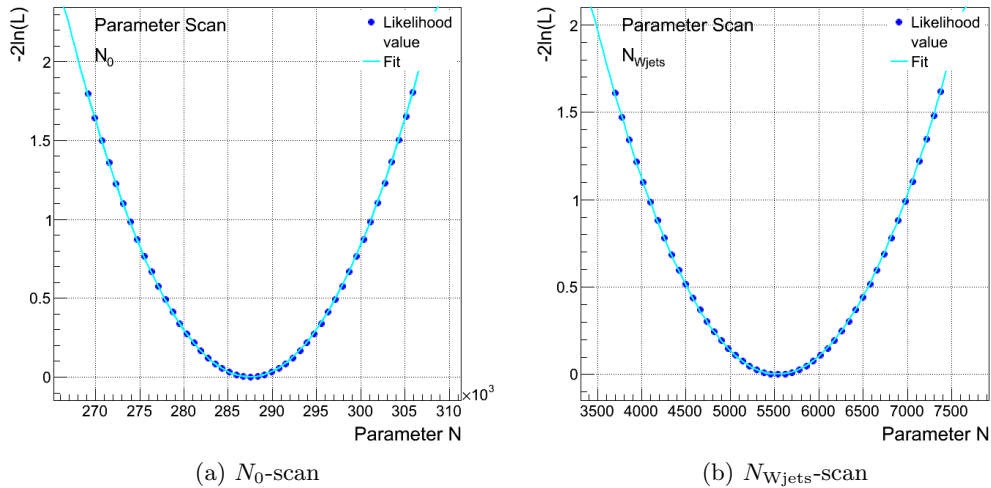


Figure 6.9: Profile likelihood scans for the (a) signal parameter  $N_0$  and the (b) background parameter  $N_{W_{jets}}$  to extract the uncertainty of the underlying fit on these parameters. The global minimum found by the minimisation process is set to zero, the uncertainty can be gained from a polynomial fit, as explained in the text.

Two different uncertainty distributions are depicted in Fig. 6.10. Both belong to the normalisation parameter  $N_L$  and are based on the same 1,000 pseudo-experiments. The plot on the left shows the uncertainties resulting from the TMinuit Hesse algorithm, the right one is based on the profiling method. The two histograms are apparently similar, the given means and the standard deviations denoted as “sigma” are consistent. The uncertainty ranges overlap, underlining that both algorithms are compatible. Several statistical outliers can be seen, but these do not cause a sensible shift or bias and do not affect the mean.

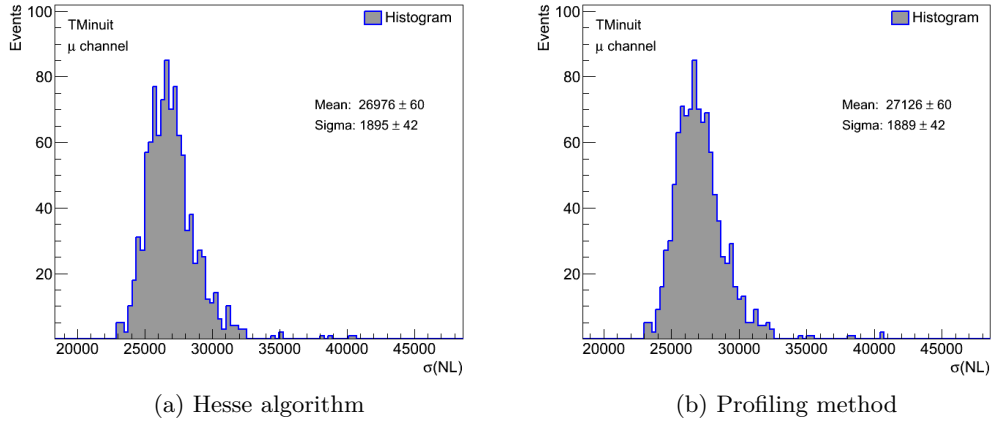


Figure 6.10: Distributions of fit uncertainties for the signal parameter  $N_L$  obtained from 1,000 pseudo-experiments based on input values  $F_{0,\text{exp}} = 0.7$ ,  $F_{L,\text{exp}} = 0.3$  and  $F_{R,\text{exp}} = 0.0$ . The uncertainties are evaluated with the help of (a) the TMinuit Hesse algorithm or (b) a self-implemented calculation referred to as *profiling method*. The distributions resemble each other to a great extent.

In order to calculate the uncertainties on the helicity fractions, the correlations between the three signal parameters  $N_0$ ,  $N_L$  and  $N_R$  are needed according to Eq. (6.3). If the Hesse algorithm is applied, these are usually directly obtained from the TMinuit fit. To be independent of these automatically calculated TMinuit correlations, they are estimated based on pseudo-experiments if the profiling method is used to compute the uncertainties of the fit. For this purpose, the fitted values of the three signal parameters gained from 1,000 pseudo-experiments are plotted in two-dimensional histograms. Three histograms are filled correspondingly and from the resulting distributions, the three necessary correlations can be derived directly:  $\varrho(N_0, N_L)$ ,  $\varrho(N_0, N_R)$  and  $\varrho(N_L, N_R)$ . Eq. (6.3) then serves to evaluate the uncertainties on the helicity fractions.

The resulting uncertainty distributions for the helicity fractions are, concerning the shape, comparable to the ones originating from the Hesse algorithm, as exemplarily shown in Fig. 6.10 for the parameter  $N_L$ . But the mean values of the histograms including the helicity fractions are different. This is due to the default correlation calculation of TMinuit which often leads to not very reliable results causing this difference. Because of these underlying problems of the TMinuit algorithm, the individually set up *profiling method* in combination with the self-implemented code to estimate correlations is applied for all upcoming studies. Exemplary correlation histograms can be found in Fig. A.6.

The uncertainty distributions from a fit without any nuisance parameters reflect the expected statistical uncertainty. If nuisance parameters are added, the value includes both a statistical and a systematic uncertainty which is further discussed on the following pages and in Chapter 6.3.4.

**Pull Distributions** Pull distributions based on a series of 1,000 pseudo-experiments with the known setup with  $F_{0,\text{exp}} = 0.7$ ,  $F_{L,\text{exp}} = 0.3$  and  $F_{R,\text{exp}} = 0.0$  including all eleven nuisance parameters have been plotted for each fit parameter and the three helicity fractions. Two pull distributions, indicating the deviation of the fitted value from the expected one which is divided by the uncertainty of the related parameter gained from the fit, are presented in Fig. 6.11, exemplarily for  $F_0$  (on the left) and  $N_0$  (on the right) both featuring the desired approximate Gaussian shape.

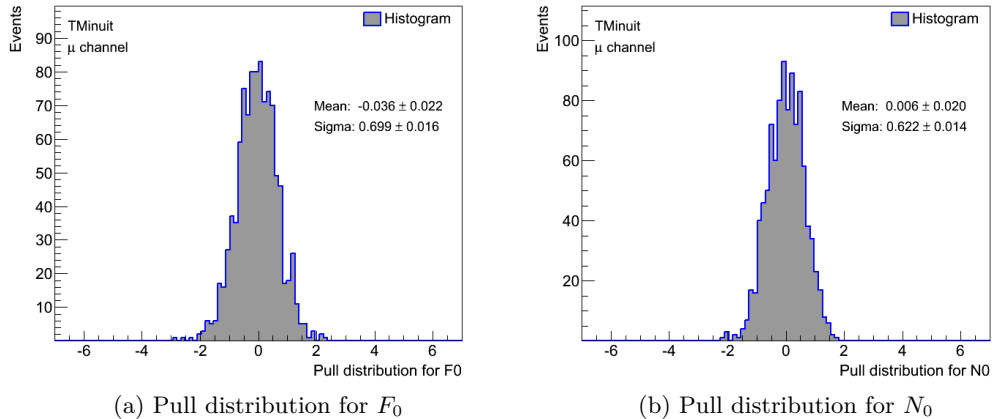


Figure 6.11: Pull distributions of fitted values for (a) the helicity fraction  $F_0$  and (b) the signal parameter  $N_0$  obtained from 1,000 pseudo-experiments based on input values  $F_{0,\text{exp}} = 0.7$ ,  $F_{L,\text{exp}} = 0.3$  and  $F_{R,\text{exp}} = 0.0$ . The selected eleven profiling parameters are used in the underlying fits.

The means are close to the expected values of zero. Regarding also the pull distributions of other parameters, the mean values are ordinarily contained in the  $2\sigma$ -region around zero which is defined by the given uncertainty on the histogram mean. This can also be seen in the exemplarily chosen distributions in Fig. 6.11.

These pull distributions allow to directly assess the quality of the fitting method regarding a possible bias, shift or a width not meeting the expectations caused by the impact of the profiling parameters since those effects are visible in deviations of the pull distributions from a Gaussian shape.

To visualise possible differences between the resulting histograms and the expectations, an ideal Gaussian curve with a peak at zero and a width of one can be plotted together with the pull distribution. This additional test is described in App. A, see Fig. A.7.

The width of the pull distributions (“sigma”) is smaller than the expectation of one due to the Gaussian constraints which are imposed on the the three background parameters and on the nuisance parameters. This affects all fit parameters in such a way that the standard deviations of the distributions decrease significantly. This can be seen when performing pseudo-experiments based on a setup with no profiling

parameters and thus with less constraints. The associated pull distributions feature much larger widths close to one. Hence, the small standard deviations do not hint at a possible underestimation of the uncertainties. This is visualised in more detail in Fig. A.8, the creation of the plots shown there is described in the next paragraph.

Pull distributions can also be analysed for other input configurations of helicity fractions not consistent with the SM expectation. Six other configurations, as introduced in Chapter 6.3.3.1, have been tested. The features of all these distributions are comparable; with a maximum close to zero where the deviation is well covered at least by the  $2\sigma$ -range derived from the uncertainty on the histogram mean. The widths of the pull distributions for  $F_0$ ,  $F_L$  and  $F_R$  are again remarkably smaller than one with values around 0.6 to 0.7. This is due to Gaussian constraints on the background parameters and the nuisance parameters, as stated above.

The mean values of all these configurations for the different fit parameters with either the associated standard deviation or the associated uncertainty are illustrated in Fig. 6.12a and Fig. 6.12b. The mean values around zero and the standard deviations smaller than one are apparent. Further plots can be found in Fig. A.9.

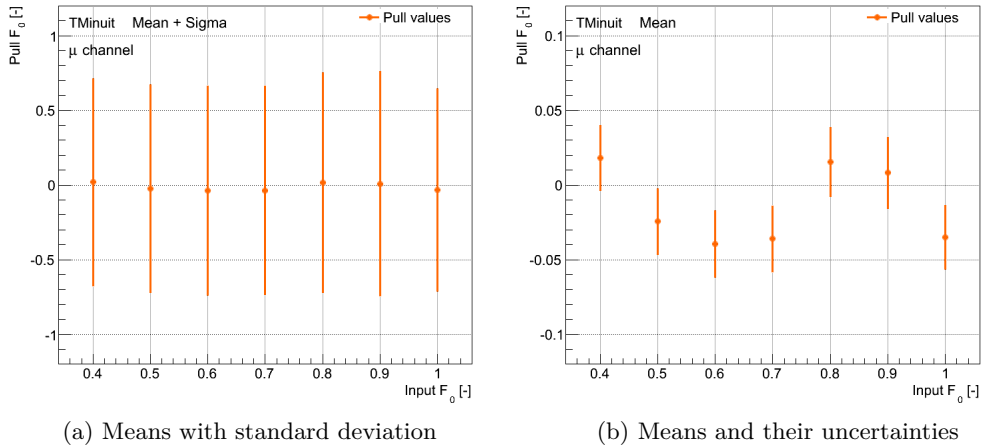


Figure 6.12: Results of pull distributions for  $F_0$  resting on different configurations of input values of the helicity fractions. In total, 1,000 pseudo-experiments have been performed for each configuration, the resulting mean values of the underlying pulls with either (a) the associated standard deviations (“sigma”) or (b) the associated uncertainties on the mean are given. The selected eleven profiling parameter are used in the underlying fits.

**Calibration Curves** The linearity of the fitting method is tested in accordance with the description in the above paragraph about the stability of the fitting method in Subsection 6.3.3.1 with seven different configurations centred around the initial values close to the SM expectation with  $F_{0,\text{exp}} = 0.7$ ,  $F_{L,\text{exp}} = 0.3$  and  $F_{R,\text{exp}} = 0.0$ . In total, 1,000 pseudo-experiments have been performed for each single configuration of input values for  $F_0$ ,  $F_L$  and  $F_R$  based on a fit including all chosen eleven nuisance parameters. Two of the resulting calibration curves for the helicity fractions and the fitted signal parameters as a function of the corresponding tested input values can be seen in Fig. 6.13, depicted are the ones for the helicity fraction  $F_0$  and the related signal parameter  $N_0$ .

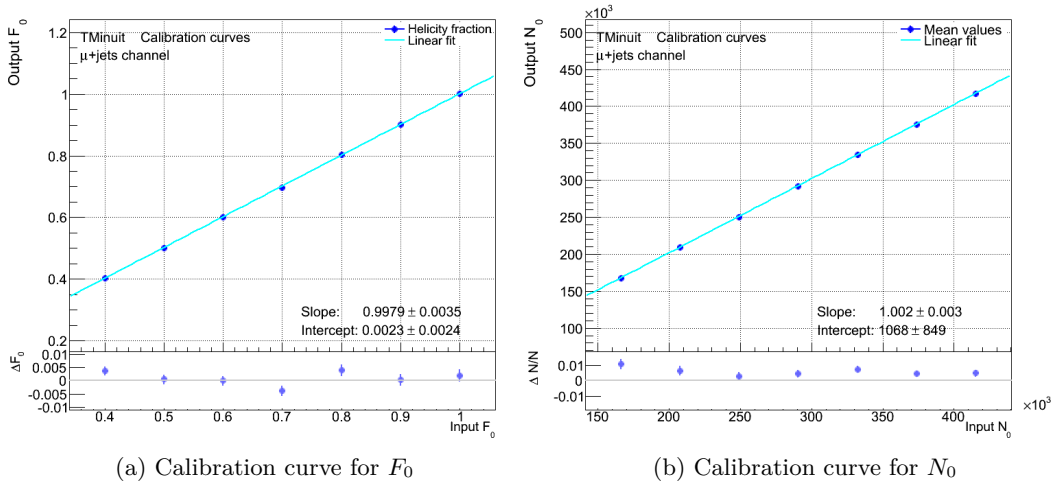


Figure 6.13: Calibration curves for (a)  $F_0$  and (b)  $N_0$  with linear fits. In total, 1,000 pseudo-experiments have been performed for each configuration used to produce these curves. The selected eleven profiling parameters are used in the underlying profile likelihood minimisation. The linear fits to the obtained values as well as the ratio between these values and the input numbers, plotted at the bottom, demonstrate the expected behaviour of the curves.

The results of the linear fit - slope and intercept with associated uncertainties - are summarised in Table 6.3 where the results of the helicity fractions and all fit parameters are given. Apart from the fitted values, the expected ones are listed in separate columns.

As already described, the curves belonging to the helicity fractions and the signal parameters are assumed to have a slope of one and an intercept of zero while the fit results of the background normalisation factors and the nuisance parameters plotted as a function of the tested input helicity values are anticipated to be best described by a straight line with a slope of zero and an intercept equalling the expected parameter value.

The fit values given in the table satisfy the theoretical expectations, the fitted intercepts and slopes lie most often in the  $1\sigma$ - or at least in the  $3\sigma$ -range defined by the corresponding uncertainties of the fit around the assumed values. For some

## 6 Measurement of the $W$ Boson Polarisation in the Muon+Jets Channel

nuisance parameters the deviation is larger, but the corresponding values are very small so that no impact on the general stability of the fit is expected. Concerning the quantities measured in this analysis, the linear fits coincide well with an intercept of zero and a slope of one. Hence, the measurement does not require an additional calibration.

	Slope		Intercept		
Helicity Fraction	Linear Fit	Exp.	Linear Fit		Exp.
$F_0$	$0.998 \pm 0.004$	1	$0.002 \pm 0.003$		0
$F_L$	$1.002 \pm 0.004$	1	$-0.001 \pm 0.002$		0
$F_R$	$1.003 \pm 0.004$	1	$-0.0004 \pm 0.0004$		0
Fit Parameter	Linear Fit	Exp.	Linear Fit		Exp.
$N_0$	$1.002 \pm 0.003$	1	$1068 \pm 849$		0
$N_L$	$1.012 \pm 0.005$	1	$-1128 \pm 703$		0
$N_R$	$1.009 \pm 0.004$	1	$146 \pm 153$		0
$N_{Wjets}$	$99 \pm 54$	0	$4350 \pm 41$		4464
$N_{QCD}$	$35 \pm 30$	0	$1752 \pm 22$		1777
$N_{RemBkg}$	$10 \pm 6$	0	$2507 \pm 4$		2517
$k(\text{BTAG})$	$0.01 \pm 0.01$	0	$-0.03 \pm 0.01$		0
$k(\text{CTAG})$	$0.002 \pm 0.008$	0	$0.009 \pm 0.006$		0
$k(\text{JEFF})$	$-0.02 \pm 0.01$	0	$0.07 \pm 0.07$		0
$k(\text{JER})$	$0.00 \pm 0.03$	0	$-0.02 \pm 0.02$		0
$k(\text{JES})$	$0.02 \pm 0.03$	0	$-0.04 \pm 0.02$		0
$k(\text{JVFSF})$	$0.001 \pm 0.003$	0	$-0.009 \pm 0.002$		0
$k(\text{MISTAG})$	$0.007 \pm 0.007$	0	$0.014 \pm 0.005$		0
$k(\text{MUON\_ID})$	$-0.001 \pm 0.001$	0	$-0.003 \pm 0.001$		0
$k(\text{MUON\_RECO})$	$-0.000 \pm 0.001$	0	$-0.002 \pm 0.001$		0
$k(\text{MUON\_TRIG})$	$0.000 \pm 0.001$	0	$-0.007 \pm 0.001$		0
$k(\text{MUSC})$	$0.01 \pm 0.03$	0	$-0.02 \pm 0.02$		0

Table 6.3: Slopes and intercepts of calibration curves derived from a linear fit based on the seven configurations of helicity fractions around the expectation with  $F_{0,\text{exp}} = 0.7$ ,  $F_{L,\text{exp}} = 0.3$  and  $F_{R,\text{exp}} = 0.0$ . To compare the fitted values to the expected input values, those numbers can be found in the columns to the right of the fit results. The normalisation parameters are rounded to integers, otherwise one significant digit is given.

**Extracting the Expected Influence of Systematic Uncertainties** As long as nuisance parameters are added to the fit, pseudo-experiments allow to estimate an expected uncertainty on the helicity fractions which constitutes a combination of the statistical and the different considered systematic uncertainties. The different nuisance parameters each representing a certain source of systematic uncertainty can be excluded from the fit one after another which allows for studying and determining the impact of individual sources of systematic uncertainties on the fit result and the evaluated combined uncertainty.

This study was done with pseudo-experiments using input helicity fractions conforming with the SM expectation values,  $F_{0,\text{exp}} = 0.7$ ,  $F_{L,\text{exp}} = 0.3$  and  $F_{R,\text{exp}} = 0.0$ . The results of these individual runs with ten nuisance parameters in each case are presented in Table 6.4, all based on 1,000 pseudo-experiments. The uncertainties on the three helicity fractions are displayed for all these runs, they constitute the mean values of the uncertainty distributions resulting from the PEs. The associated uncertainties on the means are given as well. For reasons of comparability, the values obtained from a fit with no and all eleven nuisance parameters can be seen as well. These values which constitute estimated expected uncertainties can later be compared to the measured values gained from a fit to data, as described in the next subsection.

Fitting Method	Unc. on Helicity Fraction:		
	$F_0$	$F_L$	$F_R$
Fit w/o nuis. par.	$0.0683 \pm 0.0002$	$0.0352 \pm 0.0001$	$0.0380 \pm 0.0001$
Full fit	$0.0808 \pm 0.0002$	$0.0471 \pm 0.0001$	$0.0387 \pm 0.0001$
Excluding fit par.:			
$k(\text{BTAG})$	$0.0799 \pm 0.0002$	$0.0460 \pm 0.0001$	$0.0388 \pm 0.0001$
$k(\text{CTAG})$	$0.0818 \pm 0.0002$	$0.0478 \pm 0.0001$	$0.0388 \pm 0.0001$
$k(\text{JEFF})$	$0.0817 \pm 0.0002$	$0.0478 \pm 0.0001$	$0.0387 \pm 0.0001$
$k(\text{JER})$	$0.0787 \pm 0.0002$	$0.0446 \pm 0.0001$	$0.0389 \pm 0.0001$
$k(\text{JES})$	$0.0742 \pm 0.0002$	$0.0408 \pm 0.0001$	$0.0386 \pm 0.0001$
$k(\text{JVFSF})$	$0.0809 \pm 0.0002$	$0.0471 \pm 0.0001$	$0.0388 \pm 0.0001$
$k(\text{MISTAG})$	$0.0816 \pm 0.0002$	$0.0475 \pm 0.0001$	$0.0387 \pm 0.0001$
$k(\text{MUON\_ID})$	$0.0819 \pm 0.0002$	$0.0481 \pm 0.0001$	$0.0387 \pm 0.0001$
$k(\text{MUON\_RECO})$	$0.0820 \pm 0.0002$	$0.0481 \pm 0.0001$	$0.0390 \pm 0.0001$
$k(\text{MUON\_TRIG})$	$0.0811 \pm 0.0002$	$0.0473 \pm 0.0001$	$0.0388 \pm 0.0001$
$k(\text{MUSC})$	$0.0815 \pm 0.0002$	$0.0478 \pm 0.0001$	$0.0385 \pm 0.0001$

Table 6.4: Expected uncertainties on the three helicity fractions from 1,000 pseudo-experiments each. For the different setups of pseudo-experiments, the nuisance parameter given in the first column is excluded from the fit in order to analyse the impact of the underlying systematic effect on the entire uncertainty. For reasons of comparison, the uncertainties from the full fit and the fit without nuisance parameters representing the statistical uncertainties are given in the first two rows.

The numbers show that most nuisance parameters and thus the related systematics hardly influence the combined uncertainty. In particular, removing the JES or the JER significantly reduces the uncertainty of  $F_0$  and  $F_L$  showing that these nuisance parameters cause a noteworthy systematic effect.

The uncertainty of  $F_R$  remains approximately constant, independent of the excluded nuisance parameter. This is caused by correlations between the signal parameters  $N_0$ ,  $N_L$  and  $N_R$ , as discussed extensively in the next section.

### 6.3.4 Fit Results

The different tests performed to validate the implemented fitting method outlined in Section 6.3.3 reveal that the method is stable and does not require an additional correction or calibration; the remarks concerning in particular the pull distributions or the error calculations underline that the modelling is well understood.

Hence, a fit to data can be carried out and is analysed in more detail in the upcoming section.

#### Profile Likelihood Fit to Data

In compliance with the remarks stated above, a profile likelihood fit to data is performed on the basis of 17 fit parameters incorporating normalisation and nuisance parameters. A quadratic fit is used for the interpolation. The results of the fit including the uncertainties calculated with the self-implemented profiling method are displayed in Table 6.5. The helicity fractions are determined by using Eq. (6.2) and Eq. (6.3).

A corresponding fit can also be carried out in which no nuisance parameters are used so that only the six normalisation parameters are fitted. Such a fit serves to estimate the statistical uncertainty on the helicity fractions as well as the corresponding background normalisation uncertainty. The fit results and the helicity fraction gained from the minimisation process together with their statistical uncertainties are also listed in the last column of Table 6.5.

With respect to the fitted helicity fractions, the SM prediction (see Chapter 2.2.4) is in good agreement with the fit results, the small deviations are covered by the fit uncertainties. It is noteworthy that the fitted numbers of background events are larger than the presumed values:  $N_{W\text{jets,exp}} = 4464$ ,  $N_{\text{QCD,exp}} = 1777$  and  $N_{\text{RemBkg,exp}} = 2517$ , especially with respect to  $N_{W\text{jets}}$  and  $N_{\text{QCD}}$ . This is due to the fact that the MC prediction is lower than the observed number of events. This mismatch is compensated during the fit, the effect is absorbed in the background parameters leading to this large background evaluation, which is however covered by the given uncertainties.

To conclude, the gained values for the helicity fractions and the normalisation factors mainly satisfy the expectations, especially in due consideration of the uncertainties of the fit. In the following, these uncertainties are discussed more thoroughly, before the nuisance parameter values are examined.

A comparison of the two fits with and without nuisance parameters reveals that the fitted values are consistent, the deviations are covered by the uncertainties gained from the fit. The uncertainties for all  $N_i$  increase if nuisance parameters are added due to a growing parameter space. This meets the expectations since the profiling fit including these parameters gives a combined uncertainty, containing not only the statistical but also the systematic uncertainty. The dimension of this increase, as a measure of the additional systematic uncertainty, is dependent on the fit parameter. For instance, the uncertainties on  $N_{\text{QCD}}$  and  $N_{\text{RemBkg}}$  rise only slightly whereas the

	Results	
Helicity Fraction	with NPs	w/o NPs
$F_0$	$0.703 \pm 0.085$	$0.705 \pm 0.070$
$F_L$	$0.303 \pm 0.051$	$0.302 \pm 0.036$
$F_R$	$-0.006 \pm 0.040$	$-0.007 \pm 0.039$
Fit Parameter		
$N_0$	$291,910 \pm 34,989$	$287,511 \pm 13,708$
$N_L$	$125,594 \pm 24,687$	$123,310 \pm 21,524$
$N_R$	$-2,494 \pm 16,267$	$-2,759 \pm 15,744$
$N_{W\text{jets}}$	$5,440 \pm 1,780$	$5,538 \pm 1,449$
$N_{\text{QCD}}$	$2,378 \pm 517$	$2,348 \pm 501$
$N_{\text{RemBkg}}$	$2,610 \pm 752$	$2,634 \pm 746$
$k(\text{BTAG})$	$0.01 \pm 1.01$	-
$k(\text{CTAG})$	$0.10 \pm 0.97$	-
$k(\text{JEFF})$	$0.06 \pm 0.99$	-
$k(\text{JER})$	$0.30 \pm 0.47$	-
$k(\text{JES})$	$-0.19 \pm 0.76$	-
$k(\text{JVFSF})$	$0.04 \pm 1.01$	-
$k(\text{MISTAG})$	$0.04 \pm 1.00$	-
$k(\text{MUON\_ID})$	$-0.00 \pm 1.00$	-
$k(\text{MUON\_RECO})$	$-0.00 \pm 1.00$	-
$k(\text{MUON\_TRIG})$	$-0.02 \pm 1.00$	-
$k(\text{MUSC})$	$-0.06 \pm 0.88$	-

Table 6.5: Fit results of the profile likelihood fit including all eleven available nuisance parameters (second column) or no nuisance parameters (third column) and the corresponding results for the three helicity fractions. The evaluation of the uncertainties is based on a self-implemented profiling method, the helicity fractions and their uncertainties result from calculations following Eq. (6.2) and Eq. (6.3). For reasons of clarity, two significant digits are given. The normalisation parameters are rounded to integers. The abbreviation “NP” stands for nuisance parameter. The SM expectation agrees well with the obtained fit results. The values indicate that the nuisance parameters  $k(\text{JES})$  and  $k(\text{JER})$  have the largest impact on the fit result.

growth of the uncertainty  $\sigma(N_0)$  is very remarkable.

The other systematic uncertainties need to be evaluated externally in order to provide a value for the total systematic uncertainty as not all systematic effects can be profiled. The estimation of further systematic uncertainties is addressed in Section 6.3.5.

An investigation of the uncertainties on the helicity fraction with Eq. (6.3) is more complex because correlations entering the propagation of uncertainty influence the resulting numbers. These correlations are obtained from 1,000 pseudo-experiments and listed in Table 6.6 for both the fit with and without profiling parameters.

Correlation between:	with NPs	w/o NPs
$N_0$ and $N_L$	-0.60	-0.77
$N_0$ and $N_R$	-0.74	-0.59
$N_L$ and $N_R$	0.80	0.85

Table 6.6: Correlations between the signal parameters  $N_0$ ,  $N_L$  and  $N_R$  which correspond to a profile likelihood fit including all eleven available nuisance parameters (second column) or no nuisance parameters (third column). In each case, the calculations are based on an individually implemented method using 1,000 pseudo-experiments. For reasons of clarity, two significant digits are given. As the table should impart the size of the correlation, an explicit specification of the uncertainty is waived. The abbreviation “NP” stands for nuisance parameter.

Apart from the deviations between the correlations that arise because of the different numbers of fit parameters, the table shows that the correlations possess different signs. Because of the larger uncertainties on the signal parameters when nuisance parameters are included in the fit, these signs induce a significant increase in the uncertainties of both  $F_0$  and  $F_L$  calculated with Eq. (6.3) although only the uncertainty on  $N_0$  increases drastically while the corresponding terms for  $F_R$  cancel out to a large extent. Thus, the combined uncertainty on  $F_R$  is not significantly larger than the statistical one, as displayed in Table 6.5. The large uncertainty on  $N_0$  is further discussed in Chapter 6.3.5.

Pertaining to the nuisance parameters, it can be seen that several parameters are fitted to a value of zero with an uncertainty of one, which basically corresponds to the initial values of profiling parameters before the fit is performed. This indicates a lack of sensitivity with respect to these parameters. The fit is particularly sensitive to parameters like  $k(\text{JER})$ ,  $k(\text{JES})$  but also to  $k(\text{CTAG})$ ,  $k(\text{JEFF})$  and  $k(\text{MUSC})$  which is indicated by the uncertainties being smaller than one and a fit result included in the range  $-1 < k_j < 1$  with the corresponding nuisance parameter  $k_j$ .

As illustrated in Chapter 6.3.2, the jet energy scale and the jet energy resolution have the largest impact on the  $\cos\theta^*$ -distributions concerning the normalisation and the shape. The fit results fully comply with these observations made when studying the systematics to select those which can be added to a profile likelihood fit. In particular, the fitted values of  $k(\text{JES})$  and  $k(\text{JER})$  are remarkably constrained by

the fit, the uncertainties are considerably smaller than one which underlines the sensitivity of the fit to these parameters.

Most of the nuisance parameters that are fitted to values resembling the input ones account for scale factor uncertainties barely affect the input  $\cos \theta^*$ -distributions pursuant to the findings given in Chapter 6.3.2. The corresponding six parameters can thus be removed from the fit. Some additional studies presented in App. C using, e.g., the HistFactory tool to cross-check the obtained results are only based on the remaining five profile parameters:  $k(\text{JER})$ ,  $k(\text{JES})$ ,  $k(\text{JEFF})$ ,  $k(\text{CTAG})$  and  $k(\text{MUSC})$ . In order to study their impact, despite being small, the nuisance parameters of the other six selected parameters have not been removed for the analyses presented in this chapter.

The results of the minimisation process with the fitted numbers are visualised in Fig. 6.14. The fitted  $\cos \theta^*$ -distribution is in good agreement with the data. The ratio between the data and the fit results is close to one and demonstrates the quality of the performed fit.

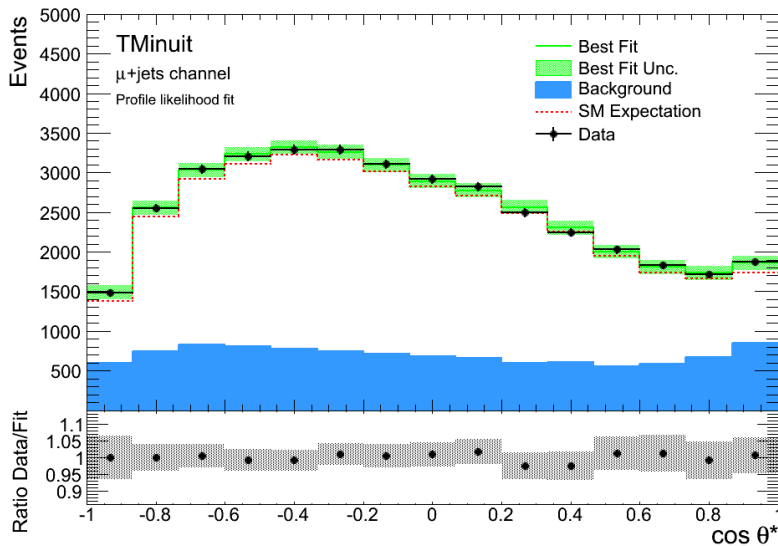


Figure 6.14: Angular distribution for the muon+jet channel including the measured data and the fitted signal and background contribution. The corresponding Standard Model expectation is displayed by the dashed line. The uncertainties obtained from the underlying profile likelihood fit are illustrated by the green band around the fitted numbers. At the bottom, the ratio of the data to the fit result is shown, the uncertainty represented by the grey bands is calculated from the uncertainty on the fitted values by means of error propagation.

### Comparing Expected and Measured Uncertainties

In a next step, the measured uncertainties gained from the fit to data including all eleven selected systematic uncertainties as profiling parameters can be compared to the corresponding expectations. For that purpose, 1,000 pseudo-experiments have been performed with an input sample based on the measured helicity fractions given in Table 6.5. The uncertainties on the fractions obtained from all pseudo-experiments are filled into a histogram, the resulting mean values and the associated standard deviations as well as the uncertainties originating from the fit to data are shown in Table 6.7.

Parameter	Measured Values:	Expected Values:	
	Uncertainty	Uncertainty	Stand. Dev.
$F_0$	0.085	$0.0831 \pm 0.0002$	$0.0061 \pm 0.0001$
$F_L$	0.051	$0.0488 \pm 0.0001$	$0.0037 \pm 0.0001$
$F_R$	0.040	$0.0395 \pm 0.0001$	$0.0029 \pm 0.0001$

Table 6.7: Measured and expected uncertainties on the  $W$  boson helicity fractions. As the expected values are derived from a distribution from pseudo-experiments with an input sample based on the measured fractions, the standard deviation is given as well in the last column. Two significant digits are shown to compare the different numbers.

The expectations agree well with the measured uncertainties. This can also be seen in Fig. 6.15 visualising the three uncertainty distributions from the pseudo-experiments and the uncertainties on the fit parameters obtained from the fit to data represented by the red line of all three helicity fractions. In each case, the measured value is close to the peak of the Gaussian-shaped distribution with regard to the related standard deviation.

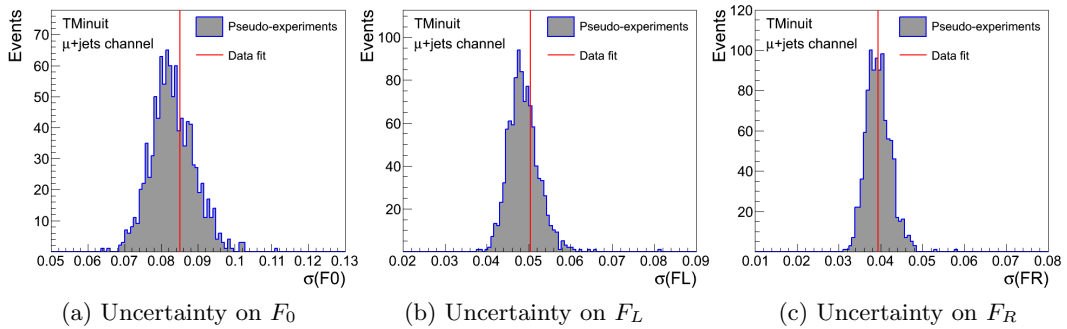


Figure 6.15: Uncertainty distributions of the fit for (a)  $F_0$ , (b)  $F_L$  and (c)  $F_R$  obtained from 1,000 pseudo-experiments based on input values equalling the measured helicity fractions. The expectation and the corresponding measured uncertainties indicated by the red line are in good agreement.

### Extracting the Influence of Systematic Uncertainties

To study the influence of individual sources of systematic uncertainties, the nuisance parameters each representing one of these systematic uncertainties can be removed from the fit one after another. The fit is then reperformed with the remaining ten nuisance parameters together with the usual signal and background normalisation parameters. Table 6.8 contains the results of these reduced fits.

Fitting Method	Unc. on Hel. Frac.:		
	$F_0$	$F_L$	$F_R$
Fit w/o nuisance parameter	0.070	0.036	0.039
Full fit	0.085	0.051	0.040
Excluding fit parameter...			
$k(\text{BTAG})$	0.083	0.049	0.040
$k(\text{CTAG})$	0.084	0.050	0.040
$k(\text{JEFF})$	0.086	0.051	0.040
$k(\text{JER})$	0.081	0.047	0.039
$k(\text{JES})$	0.076	0.042	0.040
$k(\text{JVFSF})$	0.084	0.050	0.040
$k(\text{MISTAG})$	0.084	0.050	0.040
$k(\text{MUON\_ID})$	0.085	0.051	0.040
$k(\text{MUON\_RECO})$	0.084	0.050	0.040
$k(\text{MUON\_TRIG})$	0.084	0.050	0.040
$k(\text{MUSC})$	0.084	0.050	0.039

Table 6.8: Measured uncertainties on the three  $W$  boson helicity fractions. The uncertainties originate from fits in which one nuisance parameter (given in the first column) is excluded from the fit to analyse the impact of the underlying systematic effect on the uncertainty of the fit. For reasons of comparison, the uncertainties from the full fit and the fit without nuisance parameters, representing the statistical uncertainties, are shown as well. In order to better visualise the differences between the results, two significant digits are given.

The given numbers reveal that uncertainties on  $F_R$  hardly change due to the correlations described above. Fits without the JES or the JER lead to a significant decrease in the fit uncertainty of  $F_0$  and  $F_L$ . The other nuisance parameters affect the uncertainties of the fit to a small extent, only slightly decreasing uncertainties can be observed. This is in accordance with the results gained from the full fit including all eleven fit parameters which illustrated that the fit is especially sensitive to  $k(\text{JES})$  and  $k(\text{JER})$ . The other parameters, primarily those which hardly affect the full fit, have only a very little effect on the systematic uncertainty.

According to the fitted values obtained from the full fit to data, the impact of the nuisance parameters  $k(\text{JEFF})$ ,  $k(\text{CTAG})$  and  $k(\text{MUSC})$  exceeds the influence of the other profiling parameters, except for  $k(\text{JES})$  and  $k(\text{JER})$ . This effect is not measurable here after rounding.

Furthermore, these uncertainties can be compared to the results from the equivalent

test based on pseudo-data with the Standard Model input  $F_{0,\text{exp}} = 0.7$ ,  $F_{L,\text{exp}} = 0.3$  and  $F_{R,\text{exp}} = 0.0$ , as illustrated in the last paragraph of Section 6.3.3.2. The expected and measured uncertainties are of the same order of magnitude and similar effects can be observed: The uncertainty on  $F_R$  remains approximately constant, caused by the correlations between the signal parameters. For certain parameters which hardly influence the fit, the individual uncertainties on  $F_0$  and  $F_L$  are also consistent with the ones from the full fit. Both the expected and the measured numbers indicate that the JES and the JER cause a remarkable systematic uncertainty underlining the correspondence between the measured and the expected values.

### 6.3.5 Considering Additional Systematic Uncertainties

After testing and analysing the fit results based on the minimisation process of the likelihood with eleven nuisance parameters, systematic effects which are not yet taken into account need to be estimated to compute the total systematic uncertainty of the  $W$  boson polarisation measurement are investigated more extensively in this subsection. The sources of systematic uncertainty which have not been profiled are listed in Table 6.2.

The systematic uncertainties are evaluated using ensemble tests. In order to estimate the uncertainties, variations of the individual sources are needed. This resembles the idea of profile likelihood fits using  $1\sigma$ -up- and down variations.

The different relevant systematic uncertainties are defined according to the remarks given in Section 6.1.7. But especially the treatment of systematic uncertainties on the signal and background modelling usually requires more information:

Regarding the MC generator uncertainty, ensemble tests with both MC@NLO and POWHEG signal samples both using the HERWIG shower model are carried out. Based on the results of the ensemble tests, distributions for the three helicity fractions are derived and the differences between the mean values of the histograms from the different generators are used as the systematic uncertainty.

The uncertainty caused by shower algorithms is evaluated with POWHEG samples which are interfaced to HERWIG or PYTHIA, respectively. Similar to the calculation of the MC generator uncertainty, distributions originating from the two setups are produced for all three helicity fractions and the difference between the fractions regarding the means is taken as systematic uncertainty.

As mentioned in Section 6.1.7, the estimation of the ISR/FSR uncertainty is based on samples generated with AcerMC. Two variations are available with more and less parton shower activity. Distributions of the helicity fractions are plotted for these samples, half of the difference between the largest and the smallest mean is the estimated ISR/FSR uncertainty.

To evaluate the systematic uncertainty arising from the uncertainty of the top mass, various samples in the mass range  $167.5 \text{ GeV} < m_t < 177.5 \text{ GeV}$  are produced and the uncertainties of the corresponding helicity fractions are measured in these samples.

To estimate the uncertainty arising from colour reconnection (CR), four  $t\bar{t}$  samples simulated with AcerMC and PYTHIA, characterised by different settings and based

on two different MC tunings (namely Perugia2011 and Tune A-Pro) with or without colour reconnection are applied. Fragmentation parameter settings according to [111] are used. The differences between the samples with and without CR are determined for all helicity fractions and the largest is chosen as the corresponding systematic uncertainty.

The shape uncertainty for the QCD background evaluation is estimated by using two matrix methods; differences based on these methods are calculated in due consideration of the nominal template. The largest deviation is used as shape uncertainty, individually calculated for all three helicity fractions.

To summarise, the uncertainties are usually estimated based on input variations different from the input histograms. This applies in general also to the systematics not discussed separately above but illustrated in Section 6.1.7:

Pseudo-experiments are performed, 2,000 for each variation, assuming that the fluctuation in each histogram bin are of Poisson nature. The results of these ensemble tests are translated into distributions of the three helicity fractions and the largest difference between the mean value of the nominal template and the means of the distributions that belong to the variations is taken as the resulting helicity fraction uncertainty of the underlying source of systematic uncertainty.

The ensemble tests are not only performed for the helicity fractions but also for the signal parameters to better study the underlying systematic effect. Exemplarily, the distributions of  $F_0$  and  $N_0$  resulting from the nominal sample and the up- and down-variations obtained from the ensemble tests are visualised in Fig. 6.16 illustrating the difference between the means and thus the idea of ensemble testing.

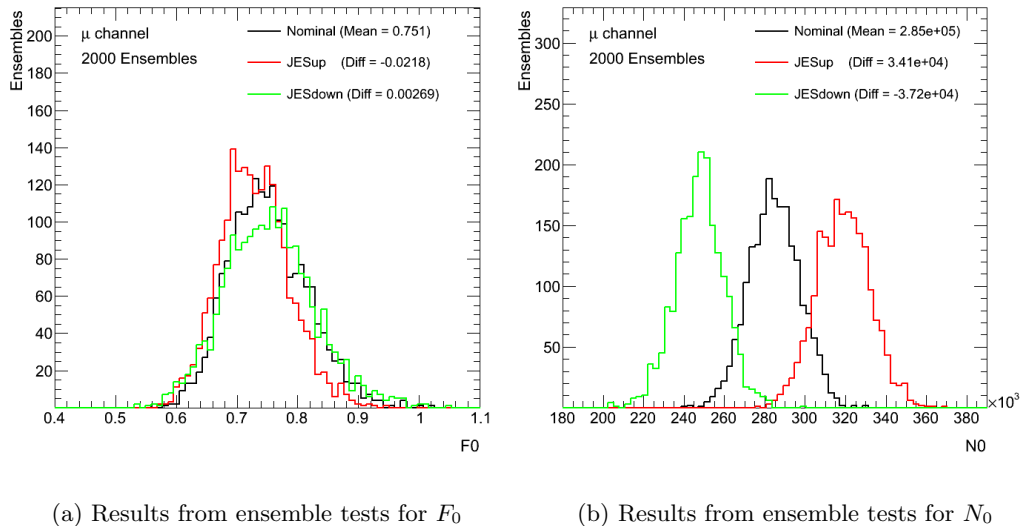


Figure 6.16: Resulting distributions from the ensemble tests for (a)  $F_0$  and (b)  $N_0$  to estimate the systematic uncertainty of the corresponding source, in this case the JES. The distributions are based on 2,000 pseudo-experiments. In the case of asymmetric uncertainties, the largest measured deviation is used.

## 6 Measurement of the $W$ Boson Polarisation in the Muon+Jets Channel

Not only the not yet considered systematic uncertainties but also the profiled ones are evaluated with these ensemble tests. This allows for a direct comparison between this alternative method to determine uncertainties and the profile likelihood fit. The obtained values for all the different sources of systematics are listed in Table 6.9, divided into uncertainties due to signal and background as well as due to detector modelling.

Source	Syst. Uncertainties:		
	$F_0$	$F_L$	$F_R$
Signal and Background Modelling			
MC generator choice	0.023	0.005	0.018
Parton showering	0.019	0.007	0.011
ISR/FSR	0.011	0.005	0.005
Colour reconnection	0.013	0.008	0.009
QCD background	0.006	0.003	0.003
Detector Modelling			
Muon reconstruction	0.012	0.003	0.009
JES	0.020	0.004	0.020
Jet reconstruction	0.026	0.002	0.024
$b$ -tagging	0.011	0.006	0.006
Calorimeter readout	0.008	0.003	0.005
Pile-up	0.012	0.005	0.007
Total systematic uncertainty	0.053	0.017	0.042
Systematic unc. w/o profiled par.	0.038	0.015	0.025

Table 6.9: Results of ensemble tests to estimate the influence of the given sources of systematic uncertainties on the three helicity fractions. The list separates between uncertainties on signal and background modelling as well as on detector modelling. The second last row contains the total systematic uncertainty calculated by adding the individual sources in quadrature. In the last row, a similar sum is given but excludes the contribution of sources which are chosen to enter the profile likelihood fit. Usually, two significant digits are presented. The jet reconstruction comprises the following sources of systematic uncertainties: JER, JEFF and JVFSF; the muon reconstruction contains the muon-related systematics and thus also the following profiled systematic effects: MUON\_ID, MUON\_TRIG, MUON\_RECO and MUSC. Uncertainties due to calorimeter readout, incorporating a “cellout” and the “softjet” term, introduced in Chapter 6.3.2, as well as due to pile-up are related to missing transverse energy.

The given numbers indicate that the uncertainty due to the JES and the JER (including the JEFF and JVFSF contributions here) is comparatively large complying with the results from the profile likelihood fit. However, several other systematic effects which cannot be profiled contribute considerably to the total systematic uncertainty. Especially the uncertainties due to the Monte Carlo generator or the parton shower model are quite substantial.

Adding all these single systematic uncertainties listed in Table 6.9 in quadrature leads to the total systematic uncertainty on the individual helicity fractions, shown in the second last row of Table 6.9. If the profile likelihood fit is not taken into account, the total uncertainty of the helicity fractions can be calculated as the square root of the quadratic sum of the systematic uncertainty gained from ensemble tests and the statistical uncertainty coming from a fit in which no nuisance parameters are used, whose results are given in the last column of Table 6.5. In this particular case, the estimation of the systematic uncertainties is completely based on ensemble tests. For this reason, the corresponding helicity fractions are labelled with the index “ET”. The helicity fractions with their total uncertainties amount to<sup>1</sup>:

$$\begin{aligned} F_{0,ET} &= 0.705 \pm 0.088 \\ F_{L,ET} &= 0.302 \pm 0.040 \\ F_{R,ET} &= -0.007 \pm 0.058 \end{aligned}$$

Using the results of the profile likelihood fit, the total uncertainty on the helicity fractions can be evaluated based on the results from the fit which involves the selected eleven nuisance parameters, shown in the second column of Table 6.5. Since the underlying systematic uncertainties are already included in the uncertainties on  $F_0$ ,  $F_L$  and  $F_R$  obtained from the fit, only the remaining systematic uncertainties need to be added from the ensemble tests. The square root of the quadratic sum of these parameters which are not profiled can be found in the last row of Table 6.9. To estimate the total uncertainty of the helicity measurement using profile likelihood fits, indicated by the index “PR”, this uncertainty and the one from the profile likelihood fit are added in quadrature. Finally, this leads to the following helicity fractions:

$$\begin{aligned} F_{0,PR} &= 0.703 \pm 0.093 \\ F_{L,PR} &= 0.303 \pm 0.053 \\ F_{R,PR} &= -0.006 \pm 0.047 \end{aligned}$$

Comparing the results from these two methods shows that the uncertainty on  $F_R$  decreases by using profile likelihood fits, whereas, however, the total uncertainties on  $F_0$  and  $F_L$  increase. This rise is mainly caused by the large uncertainty on  $N_0$ . In comparison to the fit without nuisance parameters the uncertainty on  $N_0$  more than doubles its size. Due to the correlation between the signal parameters  $N_0$ ,  $N_L$  and  $N_R$  this uncertainty propagates into a large uncertainty on both  $F_0$  and  $F_L$  although the underlying uncertainty on  $N_L$  increases only slightly compared to the fit without nuisance parameters.

At first glance, this result does not seem to meet the expectations since a decrease in the total uncertainty by using profile likelihood fits was anticipated. But a closer examination of the used input histograms serves to explain this increase:

The ensemble tests are based on templates including  $1\sigma$ -variations of the under-

---

<sup>1</sup>Two significant digits of the uncertainties with both methods to compute systematics uncertainties are given to better emphasise differences between them.

lying systematic effect. The profile likelihood, as discussed above, uses  $2\sigma$ - and  $3\sigma$ -variations at least of the systematic uncertainty which affects the results most, the jet energy scale. These variations are added to the fit as they are expected to provide more precise information than the  $1\sigma$ -variations especially for nuisance parameters which remarkably influence the fit like the JES. Further tests revealed that these  $2\sigma$ - and  $3\sigma$ -variations for the JES are responsible for the large uncertainty on  $N_0$ . Excluding them and using only the  $1\sigma$ -up- and down-variations to fit  $k(\text{JES})$  leads to a total uncertainty on the helicity fractions even smaller than the ones obtained from the ensemble tests.

Since the additional  $2\sigma$ - and  $3\sigma$ -variations are proven to enhance the precision of the JES description, this result indicates that using only  $1\sigma$ -variations may potentially bias the calculation of the uncertainty. This inference is based on the assumption that with the  $2\sigma$ - and  $3\sigma$ -variations used in the profile likelihood fit an additional but more realistic effect is taken into account - in comparison to the uncertainty determination with ensemble tests which only apply  $1\sigma$ -variations. Hence, the results of the profile likelihood fit indicate a more reliable estimate of the systematic uncertainties if profile likelihood fits instead of ensemble tests are used to compute systematic uncertainties.

It could be furthermore demonstrated that correlations considerably affect the uncertainties of the calculated helicity fractions. As the large uncertainty on  $N_0$  obtained from a fit including the selected eleven nuisance parameters and thus the large uncertainties - due to the correlations - on both  $F_0$  and  $F_L$  are caused by the additional  $2\sigma$ - and  $3\sigma$ -variations to fit  $k(\text{JES})$ , the effect of such additional variations needs to be studied in more detail in the future.

The comparatively large statistical uncertainty, particularly with respect to the given integrated luminosity, is addressed in Chapter 7. As this uncertainty does not affect the profile likelihood fit and its quality, a detailed discussion here would exceed the scope of this thesis.

Comparing both uncertainty calculations, the helicity fractions themselves are very similar to each other. They are also very close to the expected SM estimation, the small deviation is well covered by the uncertainties originating from the fit.

### 6.3.6 Measurement of the Top Quark Pair Cross-Section

Apart from the determination of *W* boson helicity fractions, the measured data allows for an estimation of the total cross-section of top quark pairs  $t\bar{t}$ . This additional test also serves to cross-check the implemented minimisation procedure. Adding the obtained numbers of the three  $t\bar{t}$  signal contributions for left-handed, right-handed and longitudinally polarised *W* bosons results in a number containing all signal events with regard to the considered decay channels:  $N_{\text{sig}} = N_0 + N_L + N_R$ . For this measurement, these three values constitute the numbers that originate from the fit to data including all chosen eleven nuisance parameters, corresponding to the numbers of signal events before the different selection cuts are applied.

To calculate the  $t\bar{t}$  cross-section  $\sigma_{t\bar{t}}$ , the following relation between  $N_{\text{sig}}$  and  $\sigma_{t\bar{t}}$  is exploited, according to the remarks in Chapter 3.2.

$$\sigma_{t\bar{t}} = \frac{N_{\text{sig}}}{\mathcal{B} \int \mathcal{L} dt}. \quad (6.4)$$

$\mathcal{B}$  denotes again the branching ratio while  $\int \mathcal{L} dt$  signifies the integrated luminosity as the luminosity integrated over a period of time  $dt$ . The number of signal events is measured in this associated time interval.

The branching ratio needs to be considered since the analysis presented here is only sensitive to events with at least one leptonically decaying *W* boson. It amounts to  $\mathcal{B}_\ell = 0.5430 \pm 0.0037$  [13] for top quark pair decays with one or more leptons participating in the decay process. The integrated luminosity of the considered period of time on which the analysis is based is  $\int \mathcal{L} dt = 4655.74 \text{ pb}^{-1}$  with an uncertainty of 1.8% [105]. With the number of fitted signal events obtained from the values given in Table 6.5, which results in  $N_{\text{sig}} = 415010 \pm 53278$ , the top quark pair cross-section can be calculated with Eq. (6.4) to:

$$\sigma_{t\bar{t}} = 164.2 \pm 21.3 \text{ pb}.$$

The associated uncertainty is estimated by means of error propagations using the uncertainties on  $N_{\text{sig}}$  including all systematics, on the branching ratio and on the integrated luminosity although the resulting total uncertainty is largely dominated by the uncertainty on  $N_{\text{sig}}$ . To evaluate the uncertainties from systematic effects not being profiled, ensemble tests have been used, as explained in Section 6.3.5.

A comparison of this measured value to the predicted cross-section, which amounts to  $\sigma_{t\bar{t}} = 166.8^{+16.5}_{-17.8} \text{ pb}$  [29], underlines a high compatibility between the two numbers. This cross-section measurement furthermore illustrates that the number of fitted background events is larger than the corresponding SM expectation. Although the data samples contain more events than the MC generated ones, the fitted cross-section fully satisfies the expectations. Consequently, the discrepancy between data and MC is compensated during the fit by the background parameters rather than by the signal parameters. This could already be seen when examining the fit results given in Table 6.5 showing how the effect of this discrepancy propagates.



## 7 Summary and Conclusion

The topic of this thesis was a presentation of profile likelihood fits in two measurements in the field of top quark physics using data collected with the ATLAS detector at the LHC. The first analysis was a measurement of the signal cross-section of single top quarks in the  $Wt$  production channel with a muon in the final state. The second analysis was the determination of the  $W$  boson polarisation in top quark pair decays concentrating on the muon+jets decay channel.

The focus was laid on the description of the measurement and the gained results with an emphasis on the realisation and technical implementation of profile likelihood fits, using different fitting algorithms or interpolation functions and being based on different tools allowing for cross-checks of the obtained results. The fundamentals of a profile likelihood analysis were shown in the first part examining its performance and possible strengths.

The second measurement comprised more detailed and complex aspects of a profile likelihood analysis including the validation of the fitting methods and more studies regarding different interpolation algorithms or estimates of the uncertainties in order to improve the understanding of the method itself as well as its distinct features.

Furthermore, it was focused on developing a flexible programme which allows for more studies and tests of the fitting and the interpolation methods, easily applicable to other analyses.

Since the task was to develop such an adaptable tool interfaced to existing analysis methods, the TMinuit fit was implemented as the standard fitting method. The TMinuit code needed to be set up individually which enabled more different studies and the just mentioned flexibility. In addition, the HistFactory tool was not fully available at the beginning of this project so that it mainly functioned as a cross-check of the gained fit results.

### Comparing Different Fitting Methods

The upcoming paragraph summarises a comparison of different tested fitting methods, investigated in the context of a measurement of the  $Wt$  production cross-section. The fit results based on both implemented fitting techniques, the TMinuit and the HistFactory fit, are highly consistent which allows to deduce that both techniques work properly and substantiate the potential of a profile likelihood fit. Removing nuisance parameters to which the fit is not sensitive does not affect the fit results. The shapes of the plotted likelihood curves are consistent with the expectations.

PEs performed with the HistFactory code indicate that the original fit operates appropriately. The small  $p_B$ -value further hints at the existence of a  $Wt$  signal.

The Hesse algorithm to calculate uncertainties of the fit parameters is less precise than the Minos algorithm but constitutes a very adequate approximation especially under consideration of the computational effort of the latter algorithm.

### Studying the Stability, the Performance and the Modelling of Profile Likelihood Fits

A very pivotal part of the second analysis which dealt with a measurement of the  $W$  boson polarisation was the validation of the used fitting method; studying its stability, performance and the modelling in general very extensively, briefly summarised in the following. In this context, the main focus was laid on presenting an overview of a more extensive analysis. Some additional tests are presented in App. C to give a brief and rough overview of supplementary fitting methods and settings while the already mentioned tool based on a TMinuit minimisation and set up in the framework of this thesis in order to adequately perform fits was used for most of the essential studies.

Several interpolation methods have been tested, one based on a quadratic fit yielded the best results as such a fit describes the behaviour of the bin entries resulting from the histograms that contain the variations around the nominal values most appropriate, in particular in due consideration of variations beyond the  $1\sigma$ -range. After selecting suitable nuisance parameters, the implemented fitting method has been validated. The parameter distributions resulting from different tests with pseudo-data revealed the desired Gaussian shape with a mean close to the expected initial value based on Standard Model expectations. The reliability of a self-implemented method to calculate uncertainties of the fit parameters and correlations has been tested.

Pull distributions illustrated the presumed behaviour with mean values around zero. Calibration curves that are based on different configurations of input values for the three different helicity fractions visualised that the fitting method is stable and linear; no additional calibration was required and the modelling could be regarded as well understood.

The fit to data yielded the following results: The obtained helicity fractions are in good agreement with the SM expectation. The impact of correlations between the helicity fractions on the fit results could be observed and investigated. A comparison between the expected and measured uncertainties underlined a very good agreement between these numbers.

Moreover, the impact of individual sources of systematic uncertainties has been investigated. The fit is mainly sensitive to five profiling parameters especially those which account for the JES and the JER uncertainties. These findings comply with the outcome of corresponding tests based on pseudo-data.

Adding additional systematic uncertainties estimated with ensemble tests to those obtained from the profiling fit allowed to evaluate total uncertainties for the three helicity fractions.

A comparison between the total uncertainties entirely obtained from ensemble tests to those evaluated with the help a profile likelihood fit revealed that concerning  $F_0$  and  $F_L$  the uncertainty increases if a profile likelihood fit is used but decreases regarding  $F_R$ . This may indicate a more reliable estimation of the uncertainties in case profile likelihood fits instead of ensemble tests are applied to evaluate the individual systematic uncertainties since the profile likelihood fit is based on more

precise information concerning systematic effects;  $2\sigma$ - and  $3\sigma$ -variations of the jet energy scale have been used in the analysis presented in this thesis. This emphasises again the potential of profile likelihood fits to possibly enhance the evaluation of uncertainties and its precision, although more tests are necessary in the future to better investigate the increasing total uncertainties.

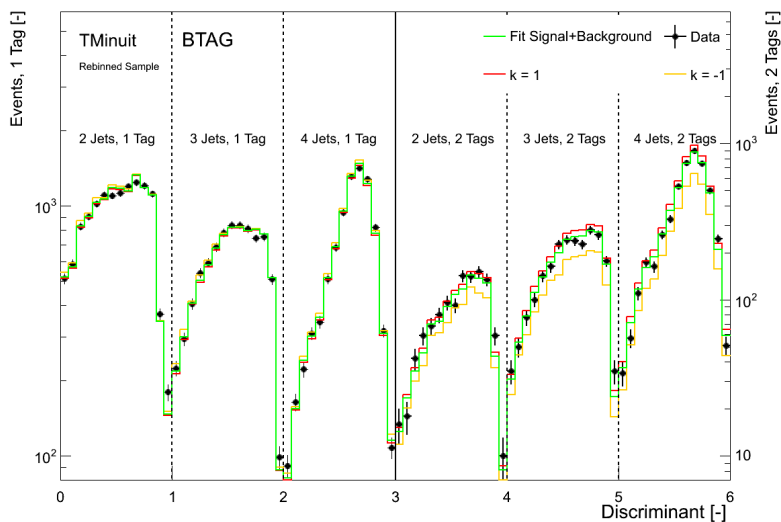
Although all the planned studies could be accomplished successfully - the concepts and the performance of profile likelihood fits as well as their validation have been examined using different interpolation methods and fitting techniques -, further tests need to be performed to better understand the different systematic uncertainties. For the sake of completeness, further systematic effects not yet considered - although assumed to be small - need to be included in the fit. Additional studies with more  $2\sigma$ - and  $3\sigma$ -variations for other systematic effect to estimate other systematic uncertainties apart from the one related to the JES are necessary. This may improve the understanding of the fitting procedure concerning the calculation of uncertainties further - especially in comparison to the uncertainty obtained from ensemble tests. Moreover, additional tests with the 16 components of the JES are necessary. Splitting the JES may advance the understanding of the impact of the systematic uncertainties on the fit uncertainties.

It is besides noteworthy that more tests concentrating on how to decrease the statistical uncertainty have already been performed. This could be achieved by applying a less conservative estimation of uncertainties for the three background parameters. The statistical uncertainties gained from a fit without nuisance parameters based on this new uncertainty evaluation amount to:  $\sigma_{\text{stat}}(F_0) = 0.046$ ,  $\sigma_{\text{stat}}(F_L) = 0.025$  and  $\sigma_{\text{stat}}(F_R) = 0.028$  and are thus significantly smaller than before.

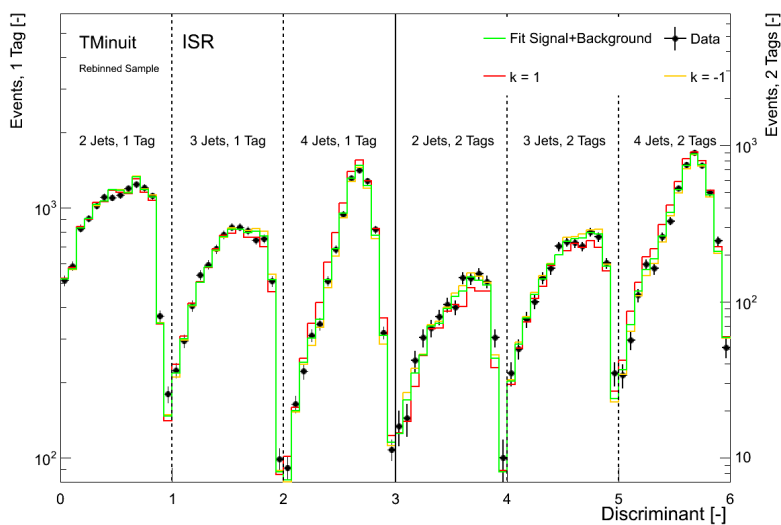
To conclude, profile likelihood fits could be proven to provide an excellent opportunity to perform various kinds of measurements in the field of top quark physics like the described cross-section measurements or measurements of  $W$  boson helicity fractions and can thus help to determine properties of the heaviest quark in more detail. All the different fits can be carried out with the help of the developed tool, established in the framework of this thesis and designed in a very flexible way enabling further promising studies and, in particular, the application to other demanding measurements in the near future.

## *7 Summary and Conclusion*

# A Additional Plots



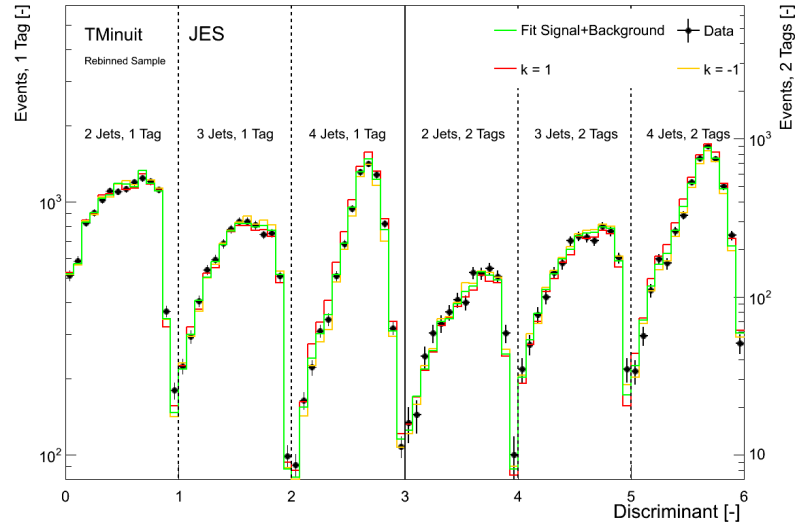
(a)  $k(\text{BTAG})$



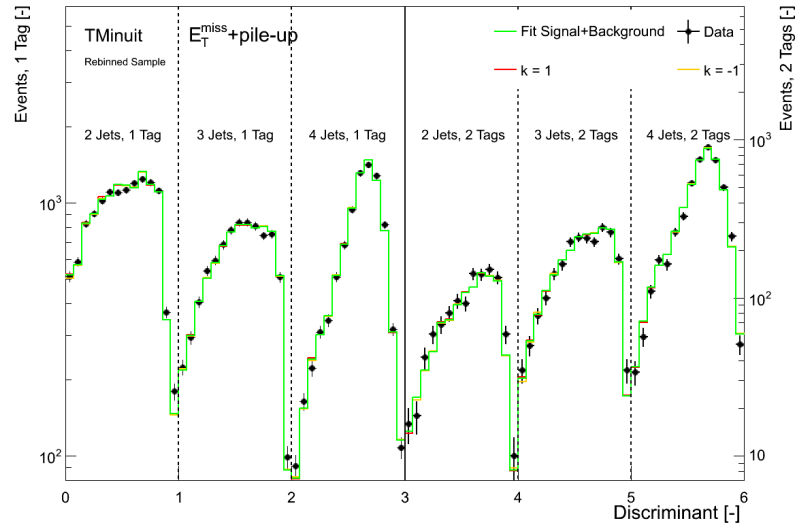
(b)  $k(\text{ISR})$

Figure A.1:  $Wt$  production: Fitted distrib. based on the TMinuit results. Also distrib. are plotted which are based on these best fit results excluding the value of one related nuisance par. which is fixed to  $\pm 1$  pursuant to the  $\pm 1\sigma$ -range. Given are the distrib. for  $k(\text{BTAG})$  and  $k(\text{ISR})$  which possess small unc. and thus small likelihood curves resulting in a noteworthy impact on the shape of the distributions.

## A Additional Plots



(a)  $k(\text{JES})$



(b)  $k(E_T^{\text{miss}} + \text{pile-up})$

Figure A.2:  $Wt$  production: Fitted distributions based on the TMinuit results. Also distributions are plotted which are based on these best fit results excluding the value of one related nuisance parameter which is fixed to  $\pm 1$  pursuant to the  $\pm 1\sigma$ -range. Given are the distributions for  $k(\text{JES})$  and  $k(E_T^{\text{miss}} + \text{pile-up})$ . The latter is characterised by a broader likelihood curve resulting in a negligible impact of the corresponding systematic effect on the shape of the distributions.

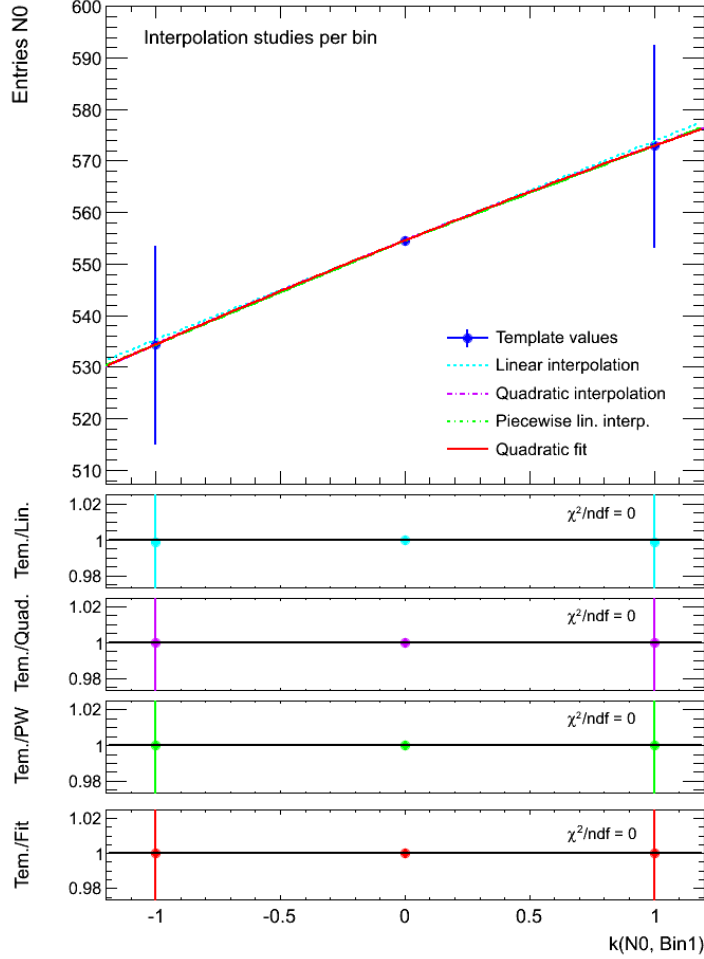


Figure A.3:  $W$  boson polarisation: Interpolation curves of the different used interpolation methods for one exemplary bin. Chosen is bin 1 of the signal distribution  $H_{N_0}$  based on the nuisance parameter  $k(\text{BTAG})$ . The different bin entries of the underlying templates are marked in blue. The different interpolation curves are coloured and hatched according to the legend. At the bottom, the ratio of the bin entry to the corresponding value of the interpolation curve is shown - separately for all approaches. The different interpolation curves feature a linear behaviour and thus overlap to a large extent. This behaviour is exemplarily for most nuisance parameters except for  $k(\text{JES})$ .

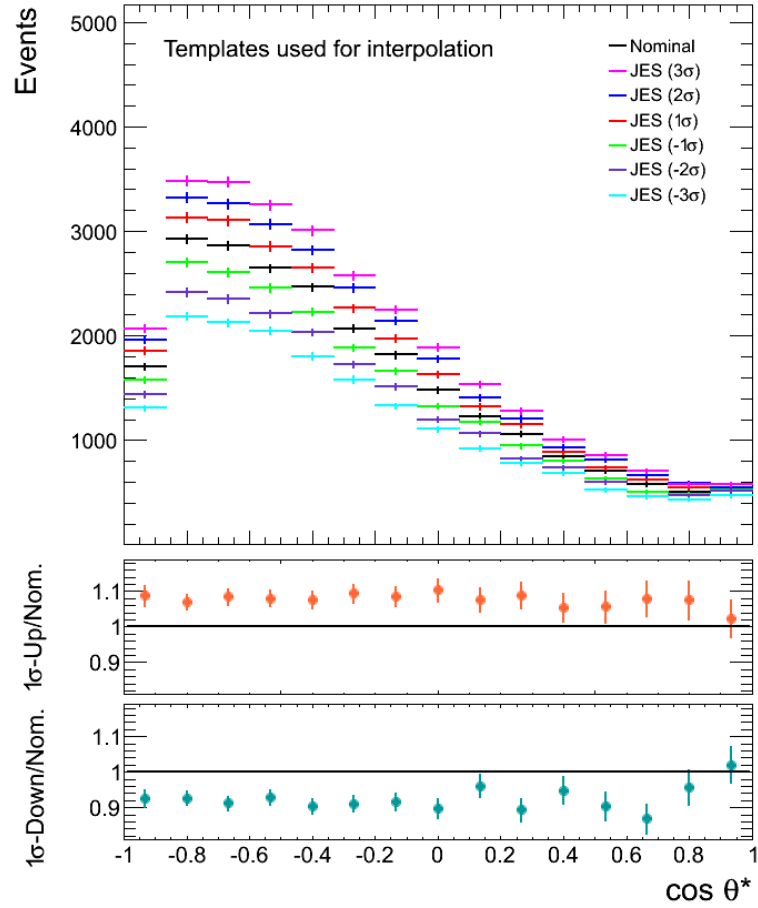


Figure A.4: The different templates correspondent to  $\pm 1\sigma$ - to  $\pm 3\sigma$ -variations based on the systematic uncertainty arisen from the JES for the fit parameter  $N_L$ . The nominal distribution can be found in the middle, coloured in black. At the bottom, the ratio of the 1 $\sigma$ -up-/down-variations to the nominal sample per bin is presented.

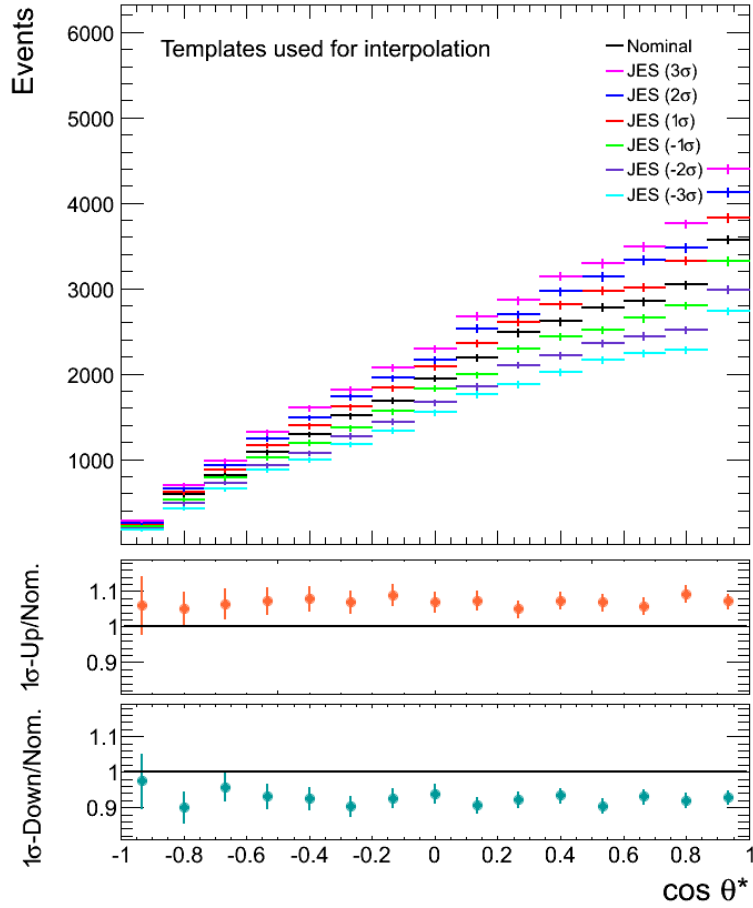


Figure A.5: The different templates correspondent to  $\pm 1\sigma$ - to  $\pm 3\sigma$ -variations based on the systematic uncertainty arisen from the JES for the fit parameter  $N_R$ . The nominal distribution can be found in the middle, coloured in black. At the bottom, the ratio of the 1 $\sigma$ -up-/down-variations to the nominal sample per bin is presented.

## A Additional Plots

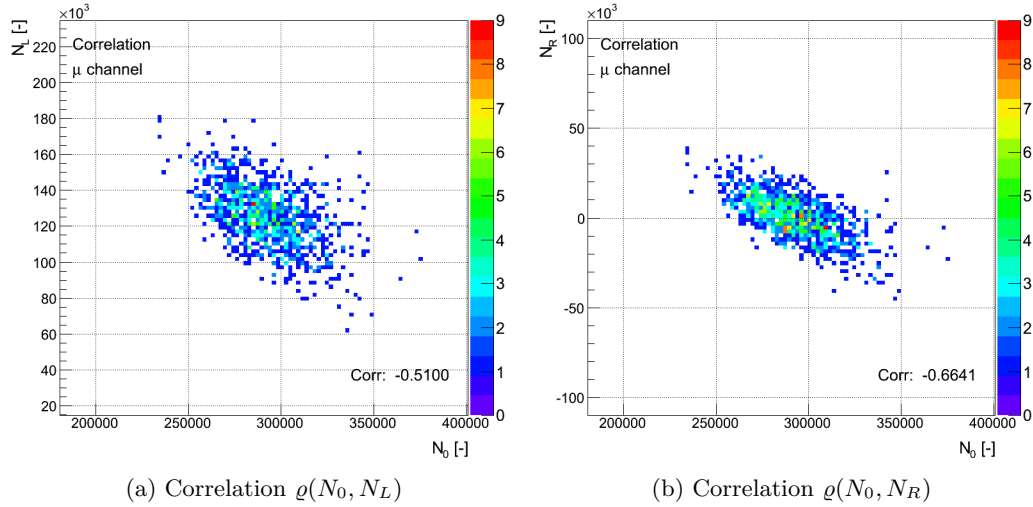


Figure A.6:  $W$  boson polarisation: Two-dimensional histograms based on the fit results of 1,000 pseudo-experiments to exemplarily show the correlations (a)  $\rho(N_0, N_L)$  and (b)  $\rho(N_0, N_R)$  between the signal parameters. These correlations are used to estimate the uncertainties on the  $W$  boson helicity fractions according to Eq. (6.3).

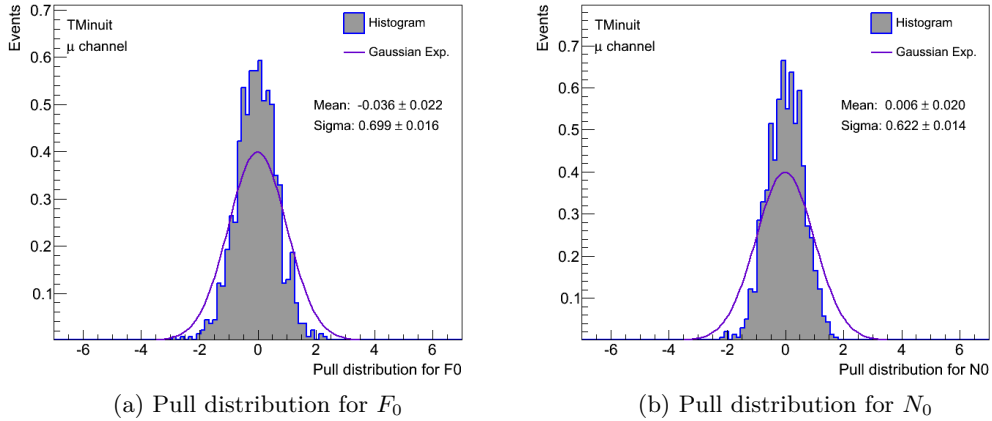
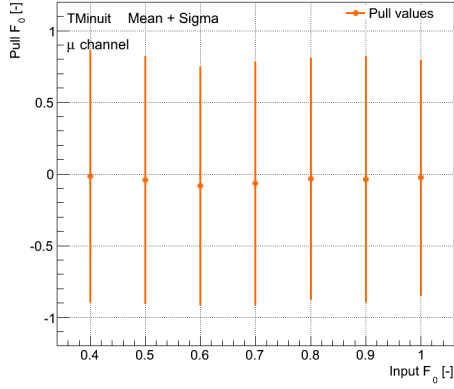
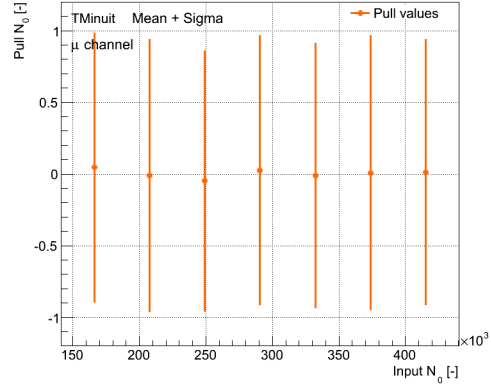


Figure A.7:  $W$  boson polarisation: Pull distributions of fitted values for (a)  $F_0$  and (b)  $N_0$  obtained from 1,000 pseudo-experiments based on input values  $F_{0,\text{exp}} = 0.7$ ,  $F_{L,\text{exp}} = 0.3$  and  $F_{R,\text{exp}} = 0.0$ . The selected eleven profiling parameters are used in the underlying fits. The pull distribution and the Gaussian curves are normalised allowing for an easier comparison, the Gaussian curves thus represent standard normal distributions.

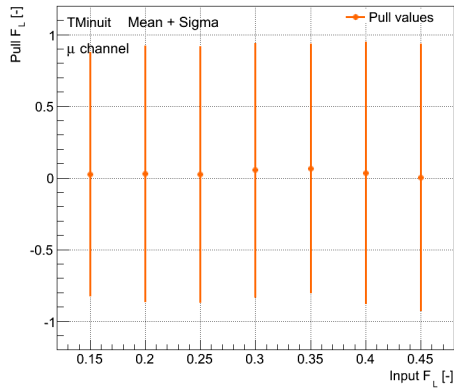
The plots illustrate that both distributions have a comparable shape, but the pull distributions are smaller than the ideal Gaussian curves and have a more distinct peak close to zero. Nevertheless, this is expected because of Gaussian constraints added to the fit. No bias or shift can be observed.



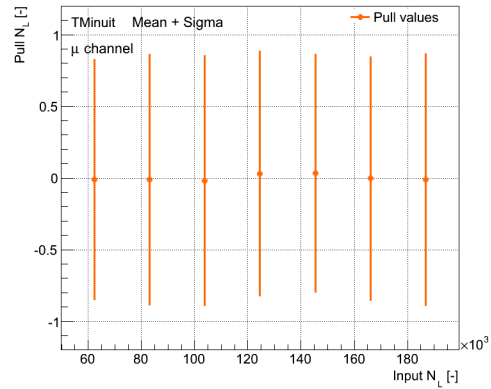
(a)  $F_0$ : Means with standard deviation



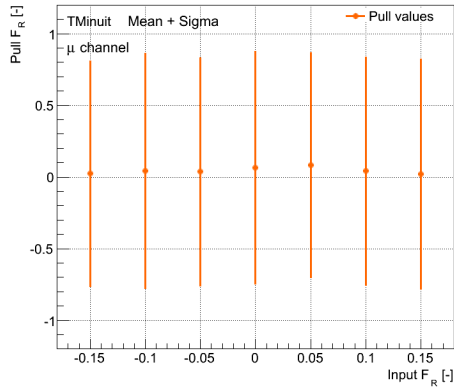
(b)  $N_0$ : Means with standard deviation



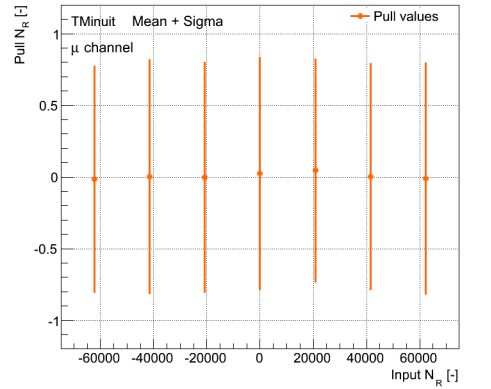
(c)  $F_L$ : Means with standard deviation



(d)  $N_L$ : Means with standard deviation



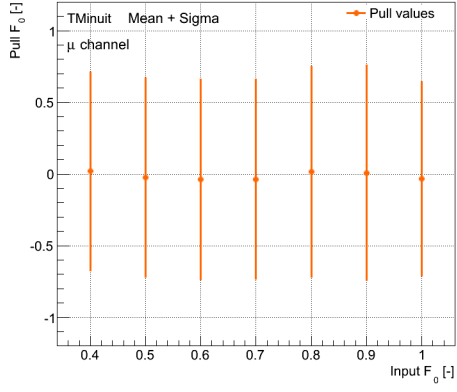
(e)  $F_R$ : Means with standard deviation



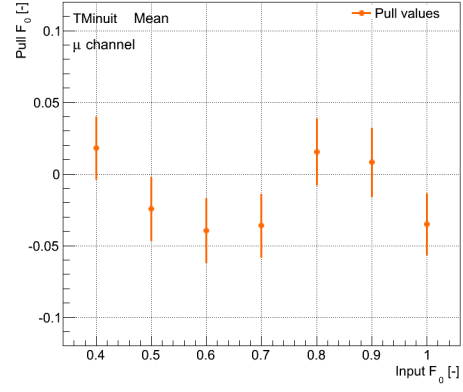
(f)  $N_R$ : Means with standard deviation

Figure A.8:  $W$  boson pol.: Results of pull distrib. for the helicity fractions (left) and the signal parameters (right) based on different configurations of input values of the helicity fractions. In total, 1,000 PEs without nuisance parameters have been performed for each configuration, the resulting mean values with the associated standard deviations (“sigma”) are given, showing that the latter are closer to one since less Gaussian constraints (due to nuisance parameters) are added to the fit.

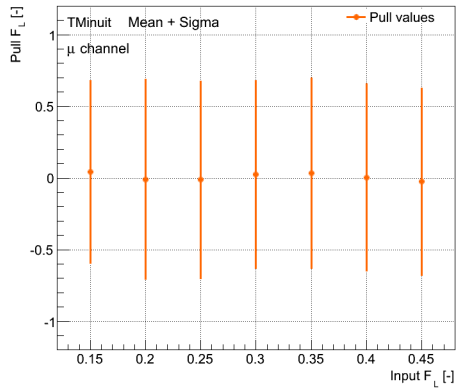
## A Additional Plots



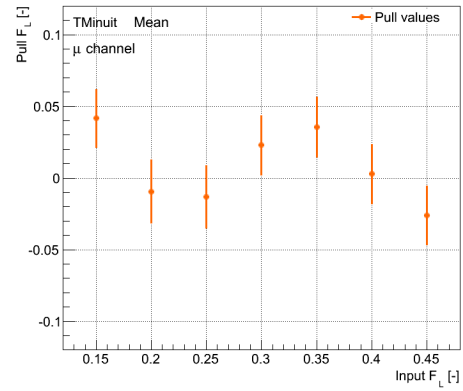
(a)  $F_0$ : Means with standard deviation



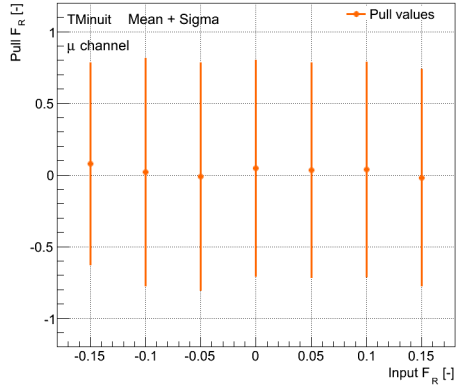
(b)  $F_0$ : Means and their uncertainties



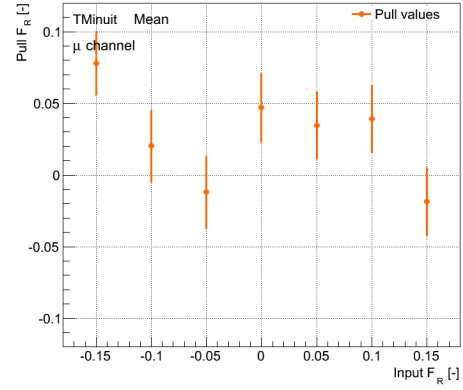
(c)  $F_L$ : Means with standard deviation



(d)  $F_L$ : Means and their uncertainties



(e)  $F_R$ : Means with standard deviation



(f)  $F_R$ : Means and their uncertainties

Figure A.9:  $W$  boson polarisation: Results of pull distributions for (a,b)  $F_0$ , (c,d)  $F_L$  and (e,f)  $F_R$  based on different configurations of input values of the helicity fractions. 1,000 PEs with all eleven profiling parameters have been performed for each configuration, the resulting mean values with either the associated standard deviations (“sigma”, left) or the associated uncertainties on the mean (right) are given.

## B Additional Studies Concerning the Measurement of the $Wt$ Production Cross-Section

The following paragraph describes the fitting method which was referred to as first fitting method in the course of the measurement of the  $Wt$  production rate. This method constitutes a rough approach since it is characterised by applying the background parameters  $N_{B,i}$  as normalisation factors, as shown in Section 5.2.1, which means that the background templates are scaled by these parameters and not solely within the one applied background shape. Nevertheless, this method acts as a further test of the profile likelihood fit and its performance whose results can be compared to the ones gained from more elaborate methods.

According to the foregoing explanation (see also Section 5.2.1), the distribution which is fitted to data can - by neglecting the dependencies - be written as:  $H_{\text{sum}} = H_S + H_B \cdot N_B$ .

Table B.1 summarises the final results for this fitting method using TMinuit for the minimisation process. Two or alternatively three (because of the background parameters close to one) fractional digits are shown. The mean of the  $N_{B,i}$  in the Gaussian constraint added to the likelihood shown in Eq. (4.7) is set to one, the variances amount to  $\sigma_2^2 = 1/214514$ ,  $\sigma_3^2 = 1/48847.3$  and  $\sigma_4^2 = 1/14849.9$  for the used 2-(excl.)-, 3-(excl.)- and 4-(incl.)-jet bins.

Most of the fitted nuisance parameter values lie in the  $\pm 1\sigma$ -range from -1 to +1 defined by the templates including the up- and down-variations. The Gaussian constraint forces the three background parameters to be close to one. As the fitted signal parameter  $N_{Wt}$  outvalues zero, the  $Wt$  production cross-section calculated with the TMinuit fit is larger than the SM expectation, which is, however, still included in the interval of the total uncertainty. The corresponding ratio pursuant to Eq. (5.1) amounts to:

$$\frac{\sigma_{Wt}}{\sigma_{Wt,\text{SM}}} = 1.37 \pm 0.56.$$

The uncertainty on the fit parameters are calculated with TMinuit using the Hesse algorithm. With the uncertainty on  $N_{Wt}$ , the uncertainty on the cross-section ratio can be evaluated by means of error propagation. The corresponding total relative uncertainty is about 41%.

B Additional Studies Concerning the Measurement of the  $Wt$  Production Cross-Section

Parameter	TMinuit Results	Parameter	TMinuit Results
$N_{Wt}$	$0.373 \pm 0.560$	$N_{B,3}$	$1.000 \pm 0.004$
$N_{B,2}$	$1.000 \pm 0.002$	$N_{B,4}$	$0.999 \pm 0.008$
$k(Wb\bar{b}Wc\bar{c})$	$0.00 \pm 1.00$	$k(K_c)$	$-0.21 \pm 0.96$
$k(Wb\bar{b}Wc\bar{c}\text{jet})$	$-0.70 \pm 0.42$	$k(K_{ll})$	$0.03 \pm 0.98$
$k(Wc)$	$-0.00 \pm 1.00$	$k(E_T^{\text{miss}})$	$0.19 \pm 0.77$
$k(Wc\text{jet})$	$-0.91 \pm 0.61$	$k(E_T^{\text{miss}} + \text{pile-up})$	$0.30 \pm 0.69$
$k(\text{MISTAG})$	$-0.89 \pm 0.67$	$k(\text{MS\_SCALE})$	$0.00 \pm 0.08$
$k(\text{BTAG})$	$0.49 \pm 0.14$	$k(\text{MUS\_ID})$	$0.39 \pm 0.64$
$k(\text{di})$	$-0.01 \pm 1.00$	$k(\text{MUS\_MS})$	$-0.00 \pm 0.04$
$k(\text{EER})$	$-0.04 \pm 0.78$	$k(\text{POWHE})$	$1.04 \pm 0.50$
$k(\text{EES})$	$0.13 \pm 0.15$	$k(\text{POWPY})$	$0.24 \pm 0.50$
$k(\text{FSR})$	$0.16 \pm 0.30$	$k(\text{preQCD})$	$0.24 \pm 0.99$
$k(\text{iqopt3})$	$-0.10 \pm 1.00$	$k(\text{ptjmin})$	$-0.17 \pm 1.00$
$k(\text{ISR})$	$-0.40 \pm 0.19$	$k(\text{QCD})$	$0.12 \pm 0.84$
$k(\text{JEFF})$	$-0.45 \pm 0.76$	$k(\text{single top})$	$0.66 \pm 0.94$
$k(\text{JER})$	$0.62 \pm 0.33$	$k(t\bar{t})$	$0.33 \pm 0.44$
$k(\text{JES})$	$-0.19 \pm 0.17$	$k(Z+\text{jets})$	$1.67 \pm 0.83$
$k(K_{bb})$	$0.15 \pm 0.55$		

Table B.1: Fit results of the profile likelihood fit with the background parameters used as normalisation parameters. Fitted values for the signal parameter  $N_{Wt}$ , for the background ones  $N_{B,i}$  as well as for all nuisance parameters are given. Abbreviations follow the remarks in Section 5.1.4.

These results can also be compared to the ones from the method described in Section 5.3.1. The deviations between the two methods are comparatively small, approximately about 2% with regard to  $N_{Wt}$ . The compatibility of fit results reflects that this fitting method successfully acts as a further cross-check of the values obtained so far despite being a rough approach.

Possible future tests in connection with this analysis include a more detailed investigation of the application of cuts. The shapes of different systematic uncertainties can also to be defined and implemented for a more profound analysis.

## C Additional Studies Concerning the Measurement of the $W$ Boson Polarisation

This part of the appendix deals with a brief description of some further additional studies which have been performed in the course of the measurement of the  $W$  boson helicity fractions in order to cross-check some of the most important results presented in Chapter 6.3. It is mainly focused on some ancillary fits to data to better assess the quality and reliability of the results gathered so far. Nevertheless, it should be added that the implementations and fitting methods used in the following have been successfully validated to show that the fit is well modelled and stable. In order not to exceed the scope of this thesis, the corresponding tests are not presented in the following.

In Section 6.3.4, in which a fit to data based on the selected eleven nuisance parameters of the  $W$  boson polarisation measurement is described, it was shown that the fit is mainly sensitive to five of these nuisance parameters and their underlying systematic uncertainties while the others only slightly affect the obtained fit results and, in particular, the measured helicity fractions of the  $W$  bosons.

Hence, a TMinuit fit is performed which uses only these five nuisance parameters, namely  $k(\text{JER})$ ,  $k(\text{JES})$ ,  $k(\text{JEFF})$ ,  $k(\text{CTAG})$  and  $k(\text{MUSC})$ , with the setup introduced in Section 6.3.4, to check whether this affects the fit results. The values obtained from the fit using these five nuisance parameters are listed in Table C.1, apart from those based on a fit without any nuisance parameters. Comparing these numbers for the helicity fractions to the corresponding ones from the minimisation process using all eleven suitable profiling parameters given in Table 6.5 shows that the values are highly consistent, the deviations amount to less than 0.1%. This large comparability concerns also the other fit parameters, the differences between the numbers from both fits are generally less than 1%.

To conclude, excluding systematic uncertainties with fitted values close to the initial ones of the associated profiling parameters from the fit do not remarkably affect the fit results. However, the uncertainty due to these systematics as a sum does not seem to be negligible, the uncertainties on  $F_0$  and  $F_L$  decrease by roughly about 5% after removing the corresponding six nuisance parameters although the fit has not a large sensitivity to the removed nuisance parameter, regarding the fitted values. Consequently, those systematics can be excluded from the fit but the still existing impact on the total uncertainty of all these parameters as a sum needs to be examined in more detail in the future.

	Results	
Helicity Fraction	with NPs	w/o NPs
$F_0$	$0.703 \pm 0.082$	$0.705 \pm 0.070$
$F_L$	$0.303 \pm 0.048$	$0.302 \pm 0.036$
$F_R$	$-0.006 \pm 0.039$	$-0.007 \pm 0.039$
Fit Parameter		
$N_0$	$292, 203 \pm 32, 927$	$287, 511 \pm 13, 708$
$N_L$	$125, 810 \pm 23, 604$	$123, 310 \pm 21, 524$
$N_R$	$-2, 497 \pm 16, 263$	$-2, 759 \pm 15, 744$
$N_{W\text{jets}}$	$5, 443 \pm 1, 776$	$5, 538 \pm 1, 449$
$N_{\text{QCD}}$	$2, 376 \pm 517$	$2, 348 \pm 501$
$N_{\text{RemBkg}}$	$2, 610 \pm 751$	$2, 634 \pm 746$
$k(\text{CTAG})$	$0.10 \pm 0.98$	-
$k(\text{JEFF})$	$0.06 \pm 0.99$	-
$k(\text{JER})$	$0.30 \pm 0.47$	-
$k(\text{JES})$	$-0.19 \pm 0.76$	-
$k(\text{MUSC})$	$-0.06 \pm 0.88$	-

Table C.1: Fit results and obtained helicity fractions of a profile likelihood fit including the five nuisance parameters to which the fit is most sensitive (second column) or no nuisance parameters (third column). The background is fitted via normalisation factors. The evaluation of the uncertainties is based on a self-implemented profiling method, the helicity fractions and their uncertainties result from calculations following Eq. (6.2) and Eq. (6.3). For reasons of clarity, two significant digits are given. The normalisation parameters are rounded to integers. The abbreviation “NP” stands for nuisance parameter.

As already mentioned in Section 6.2.1, a second fitting method can be used which relies on the idea of fitting the background via nuisance parameters without using scale factors. To perform a fit in this way,  $\pm 1\sigma$ -templates including up- and down-variations for the background templates need to be on hand. These  $\pm 1\sigma$ -distributions of one background profiling parameter which are used to scale the corresponding background can be produced on the basis of the given uncertainties which are related to the three background contributions. According to Chapter 6.2.1, they amount to 50% ( $W$ +jets), 100% (QCD) and 30% (remaining backgrounds) in a conservative approach. The up- and down-templates of the signal and the two other background contributions for one certain background source are equivalent to the nominal template so that the shapes of the other five distributions are not affected by the associated background. As a consequence, both fitting methods remain comparable since the background normalisation factors of the first fitting method only scale the related background template.

Using the second fitting method, the expression of  $H_B(\vec{k}, \vec{N}_B)$  is modified to:

$$H_B(\vec{k}, \vec{N}_B) = H_{W\text{jets}}(\vec{k}, N_{W\text{jets}}) + H_{\text{QCD}}(\vec{k}, N_{\text{QCD}}) + H_{\text{RemBkg}}(\vec{k}, N_{\text{RemBkg}}).$$

$H_{\text{sum}}(\vec{k}, \vec{N}_S, \vec{N}_B, \vec{\varepsilon}_{N_S})$  is then calculated as before. The initial values of this fitting

method are chosen as follows: The mean values are set to zero because they are assumed to be Gaussian-distributed around this value and the standard deviation to one, according to the procedure explained in Section 5.2.1.

This method has been validated like the first one on which most of the analyses are based proving that the fit behaves stable and is properly modelled.

The fit has been carried out using - apart from the three background parameters - no further nuisance parameters which account for systematic uncertainties in order to estimate the statistical uncertainty. To test this method with further profiling parameters, a fit has been performed using the five parameters to which the first fitting methods was most sensitive. The values for the three  $W$  boson helicity fractions are listed in Table C.2.

The numbers reveal that both fits using either five or no additional fit parameters yield very comparable helicity fractions, which are also very similar to the values obtained from the first fitting method using background normalisation parameters. Concerning  $F_0$  and  $F_L$ , the difference between both methods is less than 1%, the percentage deviation is larger for  $F_R$  due to its value close to zero.

The uncertainties of the fit of both methods are with respect to the statistical uncertainty consistent, but with more nuisance parameters certain deviations can be observed. The combined uncertainties including the statistical and the systematic ones of the five applied nuisance parameters is larger for the second method. In particular, the uncertainty on  $N_0$  and  $N_L$  exceeds the former value. The effect causing the large uncertainty on  $N_0$ , also noticed while testing the first fitting method, seems to be even augmented when the background is fitted via profiling parameters. Due to correlations, all helicity fractions are affected, the uncertainties increase by roughly 10%. How to study this effect further was discussed in Chapter 7. But since the values themselves are comparable, the cross-check of these two methods can be regarded as successful.

	Results	
Helicity Fraction	with NPs	w/o NPs
$F_0$	$0.703 \pm 0.089$	$0.705 \pm 0.070$
$F_L$	$0.304 \pm 0.054$	$0.302 \pm 0.036$
$F_R$	$-0.007 \pm 0.042$	$0.007 \pm 0.039$

Table C.2: Obtained helicity fractions of a profile likelihood fit using profiling parameters to fit the background contribution. The fit is thus carried out using these background nuisance parameters together with the five nuisance parameters  $k_j$  listed in the table to which the fit is most sensitive (second column) or with no additional further nuisance parameters (third column). The evaluation of the uncertainties is based on a self-implemented profiling method, the helicity fractions and their uncertainties result from calculations following Eq. (6.2) and Eq. (6.3). For reasons of clarity, two significant digits are given. The abbreviation “NP” stands for nuisance parameter.

## *C Additional Studies Concerning the Measurement of the W Boson Polarisation*

Some further studies are also based on the HistFactory tool which was extensively described in the course of the measurement of the  $Wt$  production cross-section. The fit to data yields values comparable to the implementations based on a TMinuit minimisation. The deviations between the helicity fractions obtained from the HistFactory fit using the same five nuisance parameters and the other two methods of the TMinuit fit described above are - with respect to  $F_0$  and  $F_L$  - about 1%.

However, this tool is mainly based on a variety of default settings which can hardly be modified. This limits the opportunity to perform studies with the HistFactory tool to a noticeable extent - also caused by the fact that this tool is rather new and not yet adapted to any desired number of tests and measurements. The proper implementation of a measurement of the helicity fractions with all its requirements within the HistFactory framework constituted thus a challenging task. Especially the default calculation of uncertainties with HistFactory exacerbated the effort to perform a fit comparable to the developed extensive and profound TMinuit code. Therefore, it was focused on the TMinuit fit in the course of the analysis dealing with a  $W$  boson polarisation measurement; the HistFactory fit is because of its default settings more powerful in the field of cross-section measurements as shown in Chapter 5.

# Nomenclature

## Variables and Constants

Var. and Const.	Meaning
$\mathcal{B}$	branching ratio
$B_\mu$	single vector field
$c$	speed of light
$C$	colour
$CP$	charge parity
$CPT$	charge parity time
$D_\mu$	covariant derivative
$E, E_T, E_T^{\text{miss}}$	energy, transverse energy, missing transverse energy
$f$	parton distribution function
$F_i$	helicity fractions
$g, g'$	coupling strengths
$G_F$	Fermi coupling constant
$G_{\mu\nu}^a$	field strength tensors
$\hbar$	reduced Planck constant
$H_i$	templates (used for the fits)
$J_\mu^i, j_\mu^Y$	weak isospin current, weak hypercharge current
$k_j$	nuisance parameter (used for the fits)
$L$	profile likelihood function
$\mathcal{L}$	likelihood function
$\mathcal{L}_i$	Lagrangian
$\int \mathcal{L} dt$	integrated luminosity
$m$	mass
$N_c$	colour factor
$N_i$	normalisation parameter (used for the fits)
$p$ and $p_T$	momentum and transverse momentum
$Q$	electric charge
$Q^2$	momentum transfer
$\Delta R$	distances in the $\eta$ - $\phi$ -plane
$s$	spin
$\sqrt{s}$	centre-of-mass energy
$SU$	special unitary group
$T$	weak isospin
$T_3$	weak isospin (third component)
$U$	unitary group
$V$	CKM matrix

## Nomenclature

Var. and Const.	Meaning
$V_{tb}$	one CKM matrix element
$V(\phi^+\phi)$	Higgs potential
$W_\mu^i$	vector field
$x$	Bjorken- $x$
$y_f$	Yukawa coupling
$y_{\mathcal{L}}$	likelihood discriminant
$Y$	hypercharge
$\alpha_{\text{em}}$	EM coupling
$\alpha_s$	QCD coupling
$\alpha_w$	weak coupling
$\varepsilon_i$	efficiency
$\eta$	pseudorapidity
$\theta$	polar angle
$\theta^*$	angle between the mom. direction of the charged lepton from the $W$ boson decay and the reversed mom. direction of the $b$ quark, both boosted into rest frame of the $W$ bos.
$\theta_W$	Weinberg angle
$\lambda_k$	Gell-Mann matrices ( $k = 1, \dots, 8$ )
$\Gamma$	decay width
$\Omega$	direction
$\mu_F, \mu_R$	factorisation and renormalisation scale
$\phi$	azimuthal angle
$\phi_k$	real scalar fields
$\sigma$	standard deviation
$\sigma_p$	cross-section
$\sigma_i$	Pauli matrices ( $i = 1, 2, 3$ )
$\tau$	lifetime

**Particles**

<b>Particle</b>	<b>Meaning</b>
$b$	bottom quark
$c$	charm quark
$d$	down quark
$e$	electron
$g$	gluon
$p/\bar{p}$	proton/antiproton
$q/\bar{q}$	quark/antiquark
$s$	strange quark
$t$	top quark
$u$	up quark
$W$	$W$ boson
$Z$	$Z$ boson
$\gamma$	photon
$\mu$	muon
$\nu$	neutrino
$\tau$	tau

## Abbreviations

Abbreviation	Meaning
ATLAS	A Toroidal LHC ApparatuS
BW	Breit-Wigner
CA	charge asymmetry
CKM	Cabibbo-Kobayashi-Maskawa (matrix)
CR	colour reconnection
EER	electron energy resolution
EES	electron energy scale
EM	electromagnetic
ET	ensemble test
FSR	final state radiation
HF	HistFactory
ISR	initial state radiation
JEFF	jet reconstruction efficiency
JER	jet energy resolution
JES	jet energy scale
JVF	jet vertex fraction
KLFitter	Kinematic Likelihood Fitter
LHC	Large Hadron Collider
LO	leading order
MC	Monte Carlo
NLO	next-to-leading order
NNLL	next-to-next-to-leading logarithmic
NNLO	next-to-next-to-leading order
NP	nuisance parameter
PDF	parton distribution function
PDG	Particle Data Group
PE	pseudo-experiment
PMNS	Pontecorvo-Maki-Nakagawa-Sakata matrix
PR	profile likelihood
QCD	quantum chromodynamics
QED	quantum electrodynamics
SM	Standard Model of Elementary Particle Physics
TM	TMinuit

# List of Figures

2.1	Top quark pair production: Lowest order Feynman diagrams . . . .	13
2.2	Cross-sections of physics processes at the Tevatron and the LHC . .	14
2.3	Parton distribution functions . . . . .	15
2.4	Single top quark production: Lowest order Feynman diagrams . . . .	16
2.5	$W+1$ jet production . . . . .	20
2.6	$W$ boson helicity states . . . . .	22
3.1	LHC and the corresponding accelerator chain . . . . .	26
3.2	ATLAS detector . . . . .	28
3.3	Inner Detector . . . . .	29
3.4	Calorimeter system . . . . .	31
3.5	Muon system . . . . .	32
3.6	Magnet system . . . . .	33
4.1	Visualisation of a profile likelihood fit . . . . .	37
4.2	Different input templates for a profiling fit . . . . .	38
4.3	Different interpolation methods . . . . .	40
5.1	$Wt$ production: Likelihood discriminant distributions . . . . .	51
5.2	$Wt$ production: Fit results obtained from TMinuit and HistFactory .	58
5.3	$Wt$ production: Profile likelihood scans for the signal parameter $N_{Wt}$	59
5.4	$Wt$ production: Profile likelihood scans for four different nuisance parameters . . . . .	61
5.5	$Wt$ production: PEs for the signal parameter $N_{Wt}$ . . . . .	66
6.1	$W$ polarisation: Data/MC comparison 1 . . . . .	74
6.2	$W$ polarisation: Data/MC comparison 2 . . . . .	75
6.3	$W$ polarisation: Different interpolation methods . . . . .	81
6.4	$W$ polarisation: Different JES input templates for profile likelihood fit	88
6.5	$W$ polarisation: Different normalised JES input templates for profile likelihood fit . . . . .	89
6.6	$W$ polarisation: Distributions for $F_L$ based on PEs . . . . .	92
6.7	$W$ polarisation: Distributions for $N_L$ based on PEs . . . . .	93
6.8	$W$ polarisation: Distributions for $N_{tot}$ based on PEs . . . . .	94
6.9	$W$ polarisation: Profile likelihood scans to extract uncertainties. . .	95
6.10	$W$ polarisation: Uncertainty distributions for $N_L$ based on PEs . . .	96
6.11	$W$ polarisation: Pull distributions for $F_0$ and $N_0$ based on PEs . . .	97
6.12	$W$ polarisation: Pull distributions for $F_0$ with standard deviations or uncertainties on the mean . . . . .	98

*List of Figures*

6.13	$W$ polarisation: Calibration curves for $F_0$ and $N_0$ . . . . .	99
6.14	$W$ polarisation: Angular distribution including data and fit results .	105
6.15	$W$ polarisation: Comparison between measured and expected uncertainties . . . . .	106
6.16	$W$ polarisation: Results from ensemble tests for $F_0$ and $N_0$ . . . . .	109
A.1	$Wt$ production: Best fit and fitted distributions with fixed parameter values I . . . . .	119
A.2	$Wt$ production: Best fit and fitted distributions with fixed parameter values II . . . . .	120
A.3	$W$ polarisation: Different interpolation methods for $k(\text{BTAG})$ . . . .	121
A.4	$W$ polarisation: Different JES input templates for the parameter $N_L$	122
A.5	$W$ polarisation: Different JES input templates for the parameter $N_R$	123
A.6	$W$ polarisation: Correlations between the signal parameters . . . . .	124
A.7	$W$ polarisation: Pull distributions for $F_0$ and $N_0$ based on PEs . . . .	124
A.8	$W$ polarisation: Pull distributions for the helicity fractions with standard deviations based on fits without nuisance parameters . . . . .	125
A.9	$W$ polarisation: Pull distributions for the helicity fractions with standard deviations or uncertainties on the mean . . . . .	126

# List of Tables

2.1	Particles and mediators in the SM . . . . .	7
2.2	Masses of fermions . . . . .	7
2.3	Fundamental forces and their properties . . . . .	11
2.4	Predictions for single top quark production cross-sections . . . . .	17
2.5	Branching ratios $\mathcal{B}$ of the final states from $W$ boson decays . . . . .	18
5.1	$Wt$ production: Different scenarios for the evaluation of $K$ -factors . . . . .	49
5.2	$Wt$ production: Profile likelihood fit using background parameters as nuisance parameters . . . . .	56
5.3	$Wt$ production cross-sections for different kinds of histogram binning . . . . .	63
5.4	$Wt$ production cross-sections for different cut values . . . . .	64
5.5	$Wt$ production cross-sections for different input scenarios . . . . .	65
6.1	$W$ polarisation: Event yields in the muon+jets channel . . . . .	73
6.2	$W$ polarisation: Different sources of systematic uncertainties and used nuisance parameters . . . . .	87
6.3	$W$ polarisation: Slopes and intercepts of calibration curves . . . . .	100
6.4	$W$ polarisation: Expected uncertainties on the helicity fractions . . . . .	101
6.5	$W$ polarisation: Results for fit with and without nuisance parameters . . . . .	103
6.6	$W$ polarisation: Correlations between signal parameters . . . . .	104
6.7	$W$ polarisation: Measured and expected uncertainties on the helicity fractions . . . . .	106
6.8	$W$ polarisation: Measured uncertainties on the helicity fractions . . . . .	107
6.9	$W$ polarisation: Ensemble tests to calculate systematic uncertainties . . . . .	110
B.1	$Wt$ production: Profile likelihood fit with background parameters as scale factors . . . . .	128
C.1	$W$ polarisation: Results for reduced fit with and without nuisance parameters . . . . .	130
C.2	$W$ polarisation: Results for the additional fitting method with and without nuisance parameters. . . . .	131

*List of Tables*

# Bibliography

- [1] The ATLAS Collaboration, Observation of a new particle in the search for the Standard Model Higgs boson with the ATLAS detector at the LHC, *Phys. Lett. B*, 716:1, 2012.
- [2] The CMS Collaboration, Observation of a new boson at a mass of 125 GeV with the CMS experiment at the LHC, *Phys. Lett. B*, 716:30, 2012.
- [3] S.L. Glashow, Partial Symmetries of Weak Interactions, *Nucl. Phys.*, 22:579, 1961.
- [4] A. Salam and J. C. Ward, Electromagnetic and Weak Interactions, *Phys. Lett.*, 13:168, 1964.
- [5] S. Weinberg, A Model of Leptons, *Phys. Rev. Lett.*, 19:1264, 1967.
- [6] H. D. Politzer, Reliable Perturbative Results for Strong Interactions?, *Phys. Rev. Lett.*, 30:1346, 1973.
- [7] D. J. Gross and F. Wilczek, Asymptotically Free Gauge Theories. I, *Phys. Rev. D*, 8:3633, 1973.
- [8] H. D. Politzer, Asymptotic freedom: An approach to strong interactions, *Phys. Rept*, 14:129, 1974.
- [9] P. W. Higgs, Broken Symmetries, Massless Particles and Gauge Fields, *Phys. Lett.*, 12:132-133, 1964.
- [10] P. W. Higgs, Broken Symmetries and the Masses of Gauge Bosons, *Phys. Rev. Lett.*, 13:508-509, 1964.
- [11] D. Griffiths, *Introduction to Elementary Particles*, WILEY-VCH, 2nd Edition, 2008.
- [12] M. Kobayashi and T. Maskawa, CP-Violation in the Renormalizable Theory of Weak Interaction, *Prog. Theor. Phys.*, 49(2):652-657, 1973.
- [13] J. Beringer et al. (Particle Data Group), *J. Phys. D*, 86:010001, 2012.
- [14] C. Berger, *Elementarteilchenphysik: Von den Grundlagen zu den modernen Experimenten*, Springer, 2nd Edition, 2006.
- [15] B. Pontecorvo, Mesonium and anti-mesonium, *Sov. Phys. JETP*, 6:429, 1957.
- [16] Z. Maki, M. Nakagawa and S. Sakata, Remarks on the Unified Model of Elementary Particles, *Prog. Theor. Phys.*, 28:870, 1962.

## Bibliography

- [17] F. Halzen and A. D. Martin, *Quarks and Leptons: An Introductory Course in Modern Particle Physics*, John Wiley & Sons, 1984.
- [18] S. W. Herb et al., Observation of a Dimuon Resonance at 9.5 GeV in 400-GeV proton-Nucleus Collisions, *Phys. Rev. Lett.*, 39:252, 1977.
- [19] The CDF Collaboration, T. Aaltonen et al., Observation of Top Quark Production in  $p\bar{p}$  Collisions, *Phys. Rev. Lett.*, 74:2626–2631, 1995.
- [20] The DØ Collaboration, S. Abachi et al., Observation of the Top Quark, *Phys. Rev. Lett.*, 74:2632–2637, 1995.
- [21] The DØ Collaboration, V. M. Abazov et al., Observation of single top-quark production, *Phys. Rev. Lett.*, 103:092001, 2009.
- [22] The CDF Collaboration, T. Aaltonen et al., First Observation of Electroweak Single Top Quark Production, *Phys. Rev. Lett.*, 103:092002, 2009.
- [23] V. N. Gribov and L. N. Lipatov, Deep inelastic ep scattering in perturbation theory, *Sov. J. Nucl. Phys.*, 15:438, 1972.
- [24] G. Altarelli and G. Parisi, Asymptotic freedom in parton language, *Nucl. Phys. B*, 126:298, 1977.
- [25] Y. L. Dokshitzer, Calculation of the Structure Functions for Deep Inelastic Scattering and  $e^+e^-$  Annihilation by Perturbation Theory in Quantum Chromodynamics, *Sov. Phys. JETP*, 46:641, 1977.
- [26] J. C. Collins, D. E. Soper and G. Sterman, Factorization of Hard Processes in QCD, *Adv. Ser. Direct. High Energy Phys.*, 5:1, 1988.
- [27] A. Quadt, Top quark physics at hadron colliders, *Eur. Phys. J. C*, 48:835–1000, 2006.
- [28] M. Beneke et al., Inclusive top-pair production phenomenology with TOPIXS, *JHEP*, 1207:194, 2012.
- [29] B. Acharya et al., Object selection and calibration, background estimations and MC samples for the Autumn 2012 Top Quark analyses with 2011 data, *ATL-COM-PHYS-2012-1197*, 2012.
- [30] M. Aliev et al., HATHOR - HAdronic Top and Heavy quark crOss-section calculatoR, *Comput. Phys. Commun.*, 182:1034-1046, 2011.
- [31] S. Catani, Aspects of QCD, from the Tevatron to the LHC, *arXiv:hep-ph/0005233v1*, 2000.
- [32] J. Pumplin et al., New Generation of Parton Distributions with Uncertainties from Global QCD Analysis, *JHEP*, 0207:012, 2002.
- [33] The Durham HepData Project,  
see: <http://hepdata.cedar.ac.uk/pdf/pdf3.html>, as of 20th August 2012.

- [34] P. M. Nadolsky et al., Implications of CTEQ global analysis for collider observables, *Phys. Rev. D*, 78:013004, 2008.
- [35] The ATLAS Collaboration, Statistical combination of top quark pair production cross-section measurements using dilepton, single-lepton and all-hadronic final states at  $\sqrt{s} = 7$  TeV with the ATLAS detector, *ATLAS-CONF-2012-024*, 2012.
- [36] The CMS Collaboration, Combination of top quark pair production cross section measurements, *CMS-PAS-TOP-11-024*, 2011.
- [37] The DØ Collaboration, V. M. Abazov et al., Model-independent measurement of t-channel single top quark production in  $p\bar{p}$  collisions at  $\sqrt{s} = 1.96$  TeV, *Phys. Lett. B*, 705:313-319, 2011.
- [38] The CDF Collaboration, T. Aaltonen et al., Observation of Single Top Quark Production and Measurement of  $|V_{tb}|$  with CDF, *Phys. Rev. D*, 82:112005, 2010.
- [39] R. Schwienhorst for the ATLAS collaboration, Single top-quark production with the ATLAS detector in pp collisions at  $\sqrt{s} = 7$  TeV, *arXiv:1110.2192v1 [hep-ex]*, 2011.
- [40] N. Kidonakis, NNLL resummation for s-channel single top quark production, *Phys. Rev. D*, 81:054028, 2010.
- [41] N. Kidonakis, Two-loop soft anomalous dimensions for single top quark associated production with a  $W^-$  or  $H^-$ , *Phys. Rev. D*, 82:054018, 2010.
- [42] N. Kidonakis, Next-to-next-to-leading-order collinear and soft gluon corrections for t-channel single top quark production, *Phys. Rev. D*, 83:091503, 2011.
- [43] The ATLAS Collaboration, Evidence for the associated production of a W boson and a top quark in ATLAS at  $\sqrt{s} = 7$  TeV, *Phys. Lett. B*, 08:011, 2012.
- [44] The ATLAS Collaboration, Measurement of the t-channel single top-quark production cross-section in pp collisions at  $\sqrt{s} = 7$  TeV with the ATLAS detector, *arXiv:1205.3130v1 [hep-ex]*, 2012.
- [45] The CMS Collaboration, Measurement of the single top t-channel cross section in pp collisions at  $\sqrt{s} = 7$  TeV, *CMS-PAS-TOP-11-021*, 2012.
- [46] W. Bernreuther, Top quark physics at the LHC, *arXiv:0805.1333v1 [hep-ph]*, 2008.
- [47] The ATLAS Collaboration, Measurement of the top quark charge in pp collisions at  $\sqrt{7}$  TeV in the ATLAS experiment, *ATLAS-CONF-2011-141*, 2011.
- [48] The ATLAS Collaboration, Observation of Spin Correlation in  $t\bar{t}$  Events from pp Collisions at  $\sqrt{s} = 7$  TeV Using the ATLAS Detector, *Phys. Rev. Lett.*, 108:212001, 2012.

## Bibliography

- [49] M. Jezabek and J. H. Kühn, QCD corrections to semileptonic decays of heavy quarks, *Nucl. Phys. B*, 314:1, 1989.
- [50] A. Czarnecki and K. Melnikov, Two-loop QCD corrections to top quark width, *Nucl. Phys. B*, 554:520, 1999.
- [51] K. G. Chetyrkin et al., Second Order QCD Corrections to  $\Gamma(t \rightarrow Wb)$ , *Phys. Rev. D*, 60:114015, 1999.
- [52] The DØ Collaboration, V. M. Abazov et al., Improved determination of the width of the top quark, *Phys. Rev. D*, 85:091104, 2012.
- [53] A. Czarnecki, J. G. Korner and J. H. Piclum, Helicity fractions of  $W$  bosons from top quark decays at NNLO in QCD, *Phys. Rev. D*, 81:111503, 2010.
- [54] The ATLAS Collaboration, Measurement of the  $W$  boson polarisation in top quark decays with the ATLAS detector, *JHEP*, 1206:88, 2012.
- [55] The CMS Collaboration,  $W$  helicity in top pair events, *CMS-PAS-11-020*, 2012.
- [56] O. Brüning, P. Collier, P. Lebrun, S. Myers, R. Ostojic, J. Poole and P. Proudlock, *LHC Design Report: Volume I, The LHC Main Ring*, CERN, 2004.
- [57] O. Brüning, P. Collier, P. Lebrun, S. Myers, R. Ostojic, J. Poole and P. Proudlock, *LHC Design Report: Volume II, The LHC Infrastructure and General Services*, CERN, 2004.
- [58] M. Benedikt, P. Collier, V. Mertens, J. Poole and K. Schindl, *LHC Design Report: Volume III, The LHC Injector Chain*, CERN, 2004.
- [59] *LEP Design Report: Volume II, The LEP Main Ring*, CERN, 1984.
- [60] The ATLAS Collaboration, The ATLAS Experiment at the CERN Large Hadron Collider, *JINST*, 3:S08003, 2008.
- [61] The ATLAS Collaboration, *ATLAS Detector and Physics Performance, Technical Design Report: Volume I*, CERN, 1999.
- [62] The ATLAS Collaboration, *ATLAS Detector and Physics Performance, Technical Design Report: Volume II*, CERN, 1999.
- [63] The ATLAS Collaboration, Luminosity Public Results, see: <https://twiki.cern.ch/twiki/bin/view/AtlasPublic/LuminosityPublicResults>, as of 4th August 2012.
- [64] The CMS Collaboration, The CMS experiment at the CERN LHC, *JINST* 3:S08004, 2008.
- [65] The LHCb Collaboration, The LHCb Detector at the LHC, *JINST* 3:S08005, 2008.

- [66] The ALICE Collaboration, The ALICE experiment at the CERN LHC, *JINST* 3:S08002, 2008.
- [67] CERN, Public webpage: The accelerator complex , see: <http://public.web.cern.ch/public/en/research/AccelComplex-en.html>, as of 4th August 2012.
- [68] N. Reid and D. A. S. Fraser, *Likelihood Inference in the Presence of Nuisance Parameters*, in *Statistical Problems in Particle Physics, Astrophysics and Cosmology* (Proceedings of PHYSTAT 2003), p. 265., edited by L. Leons, R. P. Mount and R. Reitmayer, 2003.
- [69] D. A. Sprott, *Statistical Inference in Science*, Springer, 2000.
- [70] A. Raue, C. Kreutz, T. Maiwald, U. Klingmüller, J. Timmer, Addressing parameter identifiability by model-based experimentation, *IET Syst. Biol.*, 5:120-130, 2011.
- [71] J. S. Conway, Incorporating Nuisance Parameters in Likelihoods for Multi-source Spectra, *arXiv:1103.0354v1 [physics.data-an]*, 2011.
- [72] The ROOT Team, *ROOT: User's Guide v5.26*, CERN, 2009, last updated 2011.
- [73] K. Cranmer, *Hist Factory Likelihood*, 2011 (draft version).
- [74] W. Verkerke and D. Kirkby, *RooFit Users Manual v2.07*, 2006.
- [75] The ATLAS Collaboration, Measurement of the top quark pair production cross-section with ATLAS in the single lepton channel, *Phys. Lett. B*, 711:244, 2012.
- [76] The GEANT4 Collaboration, S. Agostinelli et al., GEANT4: A simulation toolkit, *Nucl. Instrum. Meth. A*, 506:250-303, 2003.
- [77] The ATLAS Collaboration, ATLAS Simulation Infrastructure, *Eur. Phys. J. C*, 70:823-874, 2010.
- [78] S. Frixione and B. R. Webber, Matching NLO QCD computations and parton shower simulations, *JHEP*, 0206:029, 2002.
- [79] S. Frixione, P. Nason and B. R. Webber, Matching NLO QCD and parton showers in heavy flavour production, *JHEP*, 0308:007, 2003.
- [80] S. Frixione, E. Laenen, P. Motylinski and B. R. Webber, Single-top production in MC@NLO, *JHEP*, 0603:092, 2006.
- [81] M. L. Mangano, M. Moretti, F. Piccinini, R. Pittau and A. D. Polosa, ALPGEN, a generator for hard multiparton processes in hadronic collisions, *JHEP*, 0307:001, 2003.

## Bibliography

- [82] J. Pumplin, D. Stump, J. Huston, H. Lai, P. Nadolsky and W. Tung, New Generation of Parton Distributions with Uncertainties from Global QCD Analysis, *JHEP*, 0207:012, 2002.
- [83] C. Anastasiou, L. J. Dixon, K. Melnikov and F. Petriello, High precision QCD at hadron colliders: Electroweak gauge boson rapidity distributions at NNLO, *Phys. Rev. D*, 69:094008, 2004.
- [84] G. Corcella et al., HERWIG 6.5: an event generator for Hadron Emission Reactions With Interfering Gluons (including supersymmetric processes), *JHEP*, 0101:010, 2001.
- [85] J. M. Campbell and R. K. Ellis, MCFM for the Tevatron and the LHC, *Nucl. Phys. Proc. Suppl.*, 205-206:10-15, 2010.
- [86] J. M. Butterworth, J. R. Forshaw and M. H. Seymour, Multiparton Interactions in Photoproduction at HERA, *Z. Phys. C*, 72:637-646, 1996.
- [87] T. Sjostrand, S. Mrenna and P. Z. Skands, A Brief Introduction to PYTHIA 8.1, *Comput.Phys.Commun.*, 178:852-867, 2008.
- [88] T. Sjostrand, S. Mrenna, and P. Z. Skands, PYTHIA 6.4: Physics and Manual, *JHEP*, 0605:026, 2006.
- [89] B. P. Kersevan and E. Richter-Was, The Monte Carlo Event Generator AcerMC 2.0 with Interfaces to PYTHIA 6.2 and HERWIG 6.5, *arXiv:hep-ph/0405247v2*, 2012.
- [90] The ATLAS Top Group, Top Common Objects, see: <https://twiki.cern.ch/twiki/bin/viewauth/AtlasProtected/TopCommonObjects2011rel116>, as of 27th August 2012.
- [91] The ATLAS Collaboration, Performance of Primary Vertex Reconstruction in Proton-Proton Collisions at  $\sqrt{s} = 7$  TeV in the ATLAS Experiment, *ATLAS-CONF-2010-069*, 2010.
- [92] G. P. Salam and G. Soyez, A Practical Seedless Infrared-Safe Cone jet algorithm, *JHEP*, 0705:086, 2007.
- [93] M. Cacciari, G. P. Salam and G. Soyez, The anti- $k_t$  jet clustering algorithm, *JHEP*, 0804:063, 2008.
- [94] The ATLAS Collaboration, Data-Quality Requirements and Event Cleaning for Jets and Missing Transverse Energy Reconstruction with the ATLAS Detector in Proton-Proton Collisions at a Center-of-Mass Energy of 7 TeV, *ATLAS-CONF-2010-038*, 2010.
- [95] The ATLAS Collaboration, Commissioning of the ATLAS high-performance  $b$ -tagging algorithms in the 7 TeV collision data, *ATLAS-CONF-2011-102*, 2011.

- [96] The ATLAS Collaboration, Searches for Single Top-Quark Production with the ATLAS Detector in  $pp$  Collisions at  $\sqrt{s} = 7$  TeV, *ATLAS-CONF-2011-027*, 2011.
- [97] The ATLAS Top Group, Top ETmiss Liaison EPS, see: [https://twiki.cern.ch/twiki/bin/viewauth/AtlasProtected/TopET-missLiaison\\_EPS](https://twiki.cern.ch/twiki/bin/viewauth/AtlasProtected/TopET-missLiaison_EPS), as of 27th August 2012.
- [98] The ATLAS Top Group, Top Systematic Uncertainties 2011 PLHC, see: <https://twiki.cern.ch/twiki/bin/viewauth/AtlasProtected/TopSystematicUncertainties2011PLHC>, as of 27th August 2012.
- [99] P. Z. Skands, Tuning Monte Carlo Generators: The Perugia Tunes, *Phys. Rev. D*, 82:074018, 2010.
- [100] The ATLAS Collaboration, Updated Luminosity Determination in  $pp$  Collisions at  $\sqrt{s} = 7$  TeV using the ATLAS Detector, *ATLAS-CONF-2011-011*, 2011.
- [101] B. Abi et al., Mis-identified lepton backgrounds to top quark pair production, *ATL-COM-PHYS-2010-849*, 2010.
- [102] K. Becker et al., Mis-identified lepton backgrounds in top quark pair production studies for EPS 2011 analyses, *ATL-COM-PHYS-2011-768*, 2011.
- [103] A. Höcker, J. Stelzer, F. Tegenfeldt, H. Voss, K. Voss et al., TMVA - Toolkit for Multivariate Data Analysis, *PoS, ACAT:040*, 2007.
- [104] The ATLAS Collaboration, Measurement of the  $Wt$  production in the lepton+jets channel using a likelihood method, *ATL-COM-PHYS-2011-1704*, 2011.
- [105] The ATLAS Top Group, Top Systematic Uncertainties for Winter 2012 (rel17) 5 fb-1 analyses, see: <https://twiki.cern.ch/twiki/bin/viewauth/AtlasProtected/TopSystematicUncertainties2011>, as of 27th August 2012.
- [106] The ATLAS Production Group, MC11c Production Campaign details, see: <https://twiki.cern.ch/twiki/bin/viewauth/AtlasProtected/AtlasProductionGroupMC11c>, as of 27th August 2012.
- [107] A.D. Martin, W.J. Stirling, R.S. Thorne, G. Watt, Parton distributions for the LHC, *Eur. Phys. J. C*, 63:189-285, 2009.
- [108] J. Aguilar-Saavedra, J. Carvalho, N. F. Castro, F. Veloso and F. Onofre, Probing anomalous  $Wtb$  couplings in top pair decays, *Eur. Phys. J. C*, 50:519, 2007.
- [109] J. Aguilar-Saavedra, Single top quark production at LHC with anomalous  $Wtb$  couplings, *Nucl. Phys. B*, 804:160, 2008.

## *Bibliography*

- [110] J. Erdmann, K. Kröninger, O. Nackenhorst und A. Quadt, Kinematic Fitting of  $t\bar{t}$  events using a likelihood approach - The KLFitter package, *ATL-COM-PHYS-2009-551*, 2009.
- [111] Andy Buckley, Hendrik Hoeth, Heiko Lacher, Holger Schulz and Jan Eike van Seggem, Systematic event generator tuning for the LHC, *Eur. Phys. J. C*, 65:331, 2010.

# Acknowledgements

In the first place, I would like to express my gratitude to Prof. Dr. Arnulf Quadt for enabling me to draw up my master's thesis in his department and working a whole year on a very exciting and promising analysis which is expected to yield a lot of precise results in many fields of elementary particle physics. Furthermore, I would like to thank him for providing me with the opportunity to spend the first half of my master's project at NIKHEF, the National Institute for Subatomic Physics, in Amsterdam in the Netherlands, which was definitely a fascinating and worthwhile experience, and, certainly, for being the first referee. I am very thankful to Prof. Dr. Ariane Frey who consented to be the second referee. Both referees always have a sympathetic ear in case important questions arise or in case a reference letter needs to be drawn up. In this context, I would also like to refer to their always instructive and interesting lectures and their entertaining way of teaching. Thank you very much indeed!

I am much obliged to Dr. Marcel Vreeswijk and Andrea Knue for providing me with new input templates in Amsterdam and in Göttingen, for supervising my work at NIKHEF and in Göttingen in a very committed manner, for answering all my questions concerning top quark physics and, besides, all programming-related questions which helped to fix several bugs in my code very fast. And, not forgetting, many thanks for proof-reading!

Moreover, I wish to express my gratitude to Dr. Kevin Kröniger for also supervising my thesis very dedicatedly and, of course, for intensively proof-reading my work. I am very grateful for his patience in discussing the obtained results and all emerged problems in particular when professional knowledge in the field of statistics was needed. I would like to give thanks to Dr. Elisaveta Shabalina for also thoroughly discussing issues associated with the technical setup of profile likelihood fits.

Genuine thanks to all colleagues and friends working at the II. Institute of Physics - their contagious enthusiasm for elementary particle physics encouraged me to write my master's thesis in Göttingen and constitutes a substantial reason for staying in Göttingen to do my Ph.D. Thank you ever so much!

In this context, I would like to thank my physics teachers at school, especially Peter Fellenberg and Kirstin Oberdorf, their informative and committed lessons gave me the idea to study physics.

Special thanks to my parents for always supporting me whenever it is important and necessary, not only during the last five years I spent in Göttingen and not only during the work-intensive last months.

I am also thankful to my friends here in Göttingen especially for our always funny conversations in the canteen, our wonderful "Nordmensa".

**Erklärung** nach §18(8) der Prüfungsordnung für den Bachelor-Studiengang Physik und den Master-Studiengang Physik an der Universität Göttingen:

Hiermit erkläre ich, dass ich diese Abschlussarbeit selbständig verfasst habe, keine anderen als die angegebenen Quellen und Hilfsmittel benutzt habe und alle Stellen, die wörtlich oder sinngemäß aus veröffentlichten Schriften entnommen wurden, als solche kenntlich gemacht habe.

Darüberhinaus erkläre ich, dass diese Abschlussarbeit nicht, auch nicht auszugsweise, im Rahmen einer nichtbestanden Prüfung an dieser oder einer anderen Hochschule eingereicht wurde.

Göttingen, den 27. September 2012

(Philipp Stolte)